Development of novel experimental and computational methods for three-dimensional coherent and super-resolution microscopy

Adrien Charles-François Raymond DESCLOUX

Abstract

Optical microscopy is one widely used tool to study cell functions and the interaction of molecules at a sub-cellular level. Optical microscopy techniques can be broadly divided into two categories: partially coherent and incoherent. Coherent microscopy techniques are usually label-free and provide diffraction limited structural information about the sample refractive index distribution though the measurement of phase delay induced by the sample. Since they can be very conservative in the illumination power directed toward the sample, they exhibit very low photo-toxicity and are suitable for both high speed and time lapse imaging. Fluorescence microscopy is an incoherent microscopy method which uses biochemistry techniques to label cellular structures with fluorescent molecules which emit light when excited by a laser. Fluorescence microscopy provides diffraction limited high specificity imaging but is limited in time due to photo-bleaching and photo-toxicity. Super-resolution microscopy is a sub-category of fluorescence microscopy which manipulates and exploits some properties of the fluorescent molecules to achieve high specificity sub-diffraction imaging. Super-resolution comes however at the price of an increased total acquisition time, which limits the applications of super-resolution microscopy to relatively slow cellular processes. The ideal microscope however does not exist; due to the limited spatio-temporal bandwidth of far-field microscopy, there will always be unavoidable trade-offs. There is therefore a need to find new ways to ensure that the methods are reaching their optimal performances and a need to study how different methods can complement each others.

In this thesis I introduce several new imaging methods for phase microscopy, SIM and SOFI. I also propose a new method for the estimation of image resolution for diffraction limited and super-resolution microscopy. Finally, in the context of the AD-gut consortium, I present the application of deep neural networks for optical DNA mapping.

I start by presenting a new method for three-dimensional quantitative phase retrieval. I derive a model for the image formation of three-dimensional bright field images and, from the theoretical modeling, extrapolate a novel expression allowing to retrieve, in a single and straightforward filtering operation, the phase distribution from a bright field image stack. I then show that the phase image can be deconvolved in order to correct for the effect of the partially coherent transfer function. I also point out how the presented method is linked to the Transport-of-Intensity Equation. Using a unique image-splitting multi-plane prism that allows to acquire 8 distinct focal planes in a single exposure without having to move the sample, I demonstrate three-dimensional quantitative phase imaging at 200Hz . Finally, I show the association of three-dimensional super-resolution SOFI with phase imaging.

Abstract

To improve the imaging speed and lower the illumination intensity, I combine the same prism platform with a high-speed structured illumination. I present the first high-speed multi-plane live cell SIM imaging. Since the structured illumination presented is using a digital micro-mirror device, about 90 % of the laser light is diffracted outside of the optical path. The imaging speed was therefore limited by the low illumination power density. To improve the illumination efficiency but keep its speed and flexibility, I present a new approach for achromatic high power high speed sinusoidal structured illumination generation, based on a two-axis galvanometer mirror, a hollow retro-reflector and a mirror mounted on a piezo inside a Michelson interferometer. With the access to high illumination power density, I also show the first experimental combination of SIM with SOFI using a self-blinking dye.

Motivated by the absence of tools to objectively judge the performance of the microscopy methods I develop, I present a novel algorithm for image resolution estimation. The method estimate the resolution by correlating the image with several filtered version of itself. The method estimate the resolution of a single wide field or super-resolution image without any user defined parameter. I also show how the method can be used to identify the optimal imaging conditions for various super-resolution methods.

Finally, in the context of the AD-gut consortium, I show a practical application of deep neural networks used to assists the segmentation and mapping of the microscopy image of enzymatically labeled DNA molecules.

Keywords: Microscopy, partially coherent, quantitative phase, phase retrieval, incoherent, fluorescence, super-resolution, STED, SIM, multi-color SIM, SOFI-SIM, single molecule localization, SOFI, resolution estimation, image processing, optical DNA mapping, image segmentation, deep neural network

Résumé

La microscopie optique est un important outil de l'étude des fonctions cellulaires et des interactions entre molécules au niveau subcellulaire. Les méthodes de microscopie optique peuvent être globalement divisées en deux catégories : cohérentes et incohérentes. Les techniques de microscopie cohérente sont appliquées généralement sans bio-marqueur et fournissent une information structurelle concernant la distribution de l'indice de réfraction à travers la mesure de retardation de la phase induite par l'échantillon, limitée en résolution spatiale par la diffraction. Puisqu'elle nécessite une irradiation modérée de l'échantillon, la microscopie cohérente montre un niveau de photo-toxicité très faible et est adéquate aussi bien pour de l'imagerie à haute vitesse que pour de l'imagerie plus lente, où chaque image est prise à grand intervalle. La microscopie à fluorescence est une méthode d'imagerie incohérente qui fait appel à la biochimie pour marquer des structures cellulaires avec des molécules fluorescentes qui sont capables d'émettre de la lumière sous excitation par un rayonnement. La microscopie à fluorescence produit un signal hautement spécifique, également limité en résolution spatiale par la diffraction, mais aussi limité dans le temps à cause de l'inévitable dégradation des propriétés fluorescente des marqueur ainsi que de la photo-toxicité de l'excitation. La microscopie à super-résolution est une sous-catégorie de la microscopie à fluorescence qui manipule et exploite certaines propriétés des molécules fluorescentes pour obtenir des images au delà de la limite de diffraction. La super-résolution nécessite cependant un temps d'acquisition significativement plus élevé, ce qui limite les applications de ce type de méthode à l'étude de phénomènes relativement lent. Le microscope parfait ne peut tout simplement pas exister. A cause de la bande-passante spatio-temporelle limitée des microscopes à champ-lointain, il y aura toujours la nécessité de faire des compromis entre résolution spatiale et temporelle, spécificité, sensibilité et photo-toxicité. Il y a par conséquent un besoin permanent de trouver de nouvelles approches pour garantir que les méthodes employées opèrent au maximum de leurs capacités et d'étudier comment différentes méthodes peuvent se compléter au mieux.

Dans cette thèse, je présente plusieurs nouvelles méthodes d'imagerie pour la microscopie de phase, SIM et SOFI. Je propose également une nouvelle approche pour l'estimation de la résolution des images pour la microscopie limitée en diffraction et à super-résolution. Enfin, dans le cadre du consortium AD-gut, je présente l'application des réseaux neuronaux profonds pour la cartographie optique d'ADN.
Je commence par proposer une nouvelle méthode pour le calcul de phase quantitative tridimensionnelle. Je dérive un modèle pour la formation d'images tridimensionnelles en champ clair et, à partir de la modélisation théorique, j'extrapole une nouvelle expression permettant

Résumé

de retrouver, en une seule et simple opération de filtrage, la distribution de phase d'une série d'images en champ clair. Je montre ensuite que l'image de phase peut être déconvoluée afin de corriger l'effet de la fonction de transfert partiellement cohérente. Je démontre également comment la méthode présentée est liée à l'équation de transport d'intensité.

En utilisant un prisme multi-plans unique qui permet l'acquisition de 8 plans focaux distincts en une seule exposition sans avoir à déplacer l'échantillon, je réalise de l'imagerie de phase quantitative tridimensionnelle à 200 images par secondes . Enfin, je montre l'association de l'imagerie de phase avec l'imagerie de fluctuation optiques à super-résolution (SOFI) tridimensionnel.

Afin d'améliorer la vitesse d'imagerie et diminuer la dose d'illumination, je présente la première réalisation expérimentale de la combinaison d'une illumination structurée (SIM) avec le prisme multi-plans pour l'imagerie à haute vitesse de cellules vivantes. Comme l'illumination structurée présentée utilise un dispositif numérique à micro-miroirs, environ 95% de la lumière laser est diffractée en dehors du chemin optique. La vitesse d'imagerie a donc été limitée par la faible densité de puissance d'illumination. Afin d'améliorer l'efficacité de l'illumination mais de conserver sa vitesse et sa flexibilité, je présente une nouvelle approche pour la génération d'une illumination structurée sinusoïdale achromatique à haute puissance et à haute vitesse, basée sur un miroir galvanométrique à deux axes, un rétroréflecteur creux et un miroir monté sur un élément piézoélectrique placé à l'intérieur d'un interféromètre de Michelson. Avec l'accès à une densité de puissance d'illumination élevée, je démontre également la première combinaison expérimentale de SIM avec SOFI.

Motivé par l'absence d'outils permettant de juger objectivement des performances des méthodes de microscopie que je développe, je présente un nouvel algorithme d'estimation de la résolution des images en corrélant l'image avec plusieurs versions filtrées de celle-ci. La méthode est capable d'estimer le support du contenu fréquentiel d'une seule image limitée par la diffraction ou à super-résolution sans aucun paramètre défini par l'utilisateur. Je montre également comment la méthode peut être utilisée pour identifier les conditions d'imagerie optimales pour différentes méthodes de super-résolution.

Enfin, dans le contexte du consortium AD-gut, je montre une application pratique des réseaux neuronaux profonds utilisés pour aider à la segmentation et à la cartographie de l'image microscopique de molécules d'ADN marquées par des enzymes.

Mot-clés : Microscopie, cohérence partielle, phase quantitative, extraction de la phase, incohérence, fluorescence, super-resolution, STED, SIM, localization de molécules, SOFI, estimation de la résolution, traitement d'image, recensement d'ADN optique, segmentation d'image, réseaux neuronaux profonds

Contents

Contents

Introduction

One of the first trace of optical engineering dates back to 424 B.C.E. where Aristophanes mentions the burning glass, a large positive lens used to start a fire. Two treatises written around 984 by Ibn Sahl (940-1000), termed *"On the burning instruments"* and *"The book of burners"* report the first description of the *Law of Refraction.* Besides the use of lenses to set thing on fire, Roman artisans also used magnifying glasses for detailed work[1].

It is only in the Seventeenth Century that Galileo Galilei (1564-1642) and Johannes Kepler (1571-1630) built and developed the first generation of telescopes. At the same time, the first microscope was invented by Zacharias Janssen (1588-1632). Theses practical creations were followed by the rediscovery of the *Law of Refraction* by Willebord Snell (1591-1626) and René Descartes (1596-1650) who published it in its modern form. The view of light as a particle or a ray, strengthened by the contribution of Pierre de Fermat (1601-1665) and its *Principle of Least Time* was however challenged by the discovery of diffraction by Francesco Maria Grimaldi (1618-1663). The wave theory was born, and was a direct contradiction to the established ray picture.

The debate concerning the wave/particle nature of light continued until 1801, year at which Thomas Young (1773-1829) realized the famous double-slit experiment, disproving the ray nature of light and presenting a fundamental concept, the *Principle of Interference.* A few years later, Auguste Jean Fresnel (1788-1827) solved the problem of rectilinear propagation of light by showing that a primary wave in which each point of the wavefront was the source of spherical secondary wavelets would interfere to reform the same propagating primary wave front.

In 1864, James Clerk Maxwell (1831-1879) synthesized the field of electricity and magnetism in a single set of equations and was able to show that light is *"an electromagnetic disturbance in the form of transverse waves"*. He left in inheritage a fundamental equation:

$$\bigtriangledown^2 \vec{\mathbf{E}} = \epsilon_0 \mu_0 \frac{\partial^2 \vec{E}}{\partial^2 t^2} \tag{1}$$

where $\bigtriangledown^2$ denotes the Laplacian of the electric field component $\vec{\mathbf{E}}$ and ϵ_0, μ_0 the electric and magnetic vacuum permittivity, respectively.

In 1873, Ernst Abbe (1840-1905) developed the first theory of image formation for a microscope,

which led to tremendous improvement in the design and manufacturing of low aberration optical system. Assuming an ideal imaging setup, Abbe derived the equation for the resolution of microscope, that is the smallest distance at which two points can still be distinguished as two entities:

$$\delta_r = \frac{\lambda}{\mathrm{NA}_i + \mathrm{NA}_d} \tag{2}$$

where λ is the central wavelength of the light used to illuminate the sample and $\mathrm{NA}_i, \mathrm{NA}_d$ is the sine of the incidence and the detection angle, respectively.

In 1905, Albert Einstein (1879-1955) proposed a new theory in which light was composed of particles of energy. The energy of one quanta of light or photon is equal to its frequency ν multiplied by Plank's constant h. Through the contributions of many great minds such as Heisenberg, Schrödinger, Dirac, Bohr and others, quantum mechanics grew into a well-grounded highly successful theory. The wave-particle debate of the last centuries changed into a duality, where a particle can be in a superposition of states which can interfere.

In 1917, Albert Einstein published a paper postulating stimulated emission as a mode of interaction of a quantum of radiation with a two level system. This theoretical discovery, followed by its experimental observation in 1928 led to the invention of the laser in 1960. The access to high power highly coherent monochromatic source allowed to discover and study new optical phenomenon such as second harmonic generation, holography, frequency mixing, optical phase conjugation, spectroscopy, laser trapping and cooling as well as novel fiber based communication system.

In parallel, the development of high precision manufacturing tool enabled the production of high-precision lenses and high-resolution diffraction limited imaging became a reality. The discovery of fluorescent molecules and proteins, together with multi-layer thin film coating, became an ubiquitous tool in life-science research. In the early 2000, several methods were proposed to image structures beyond the diffraction limit, opening new applications in the life-science research field. At the beginning of my thesis, super-resolution microscopy was a well established field of research and was slowly finding its place into research groups that aims at using super-resolution as a tool to answer their questions. Several approaches for super-resolution were and are developed but, due to the limited spatio-temporal bandwidth of far-field microscopy, all super-resolution techniques have to trade speed for spatial resolution. Therefore, there is a general need to study how different methods can complement each other and how the methods can perform at their optimal level.

The core of this thesis focuses on the theoretical and experimental development of new methods for microscopy, from label-free coherent imaging and super-resolution microscopy, both in 2D and 3D. Building upon existing models, I developed a new method for 3D quantitative phase retrieval from partially coherent bright field image stacks. Using an already developed and implemented multi-plane prism, I shown volumetric quantitative phase imaging at 200 Hz in live cells. I also demonstrated how the method can be associated with super-resolution microscopy and become a unique platform for three dimensional structural and functional imaging. Aiming at improving the imaging speed and lowering the illumination power den-

sity for live cell imaging, I combined the multi-plane prism with a structured illumination and realized high-speed high-resolution three dimensional imaging of live cells. The SIM implementation we used was based on a digital micro-mirror device, which has a very low transmission of about 90% as most of the laser light is diffracted outside of the optical axis. To improve the power efficiency but keep the flexibility and speed, I designed and realized a new structured illumination concept based on a 2-axis galvanometer mirror, a retro-reflector and a mirror mounted on a piezoelectric element inside a Michelson interferometer. The presented illumination is insensitive to the illumination wavelength. I demonstrated the ability of the setup to perform multi-color SIM imaging. Having access to high power-density, I show the first experimental combination of SIM with SOFI using a self-blinking dye. Motivated by the the absence of methods for resolution estimation in microscopy and super-resolution microscopy, I proposed a new method based on partial phase correlation of the image with filtered version of itself. The method is completely parameter free and is able to predict the resolution of any microscopy images. Finally, in the context of the AD-gut[2] consortium, I showed how deep neural networks can be used to assist the segmentation and mapping of the image of enzymatically labelled DNA molecules.

This thesis is structured as follow:

Chapter 1 is devoted to present and review the theoretical concepts used and developed throughout this thesis. The basic principle of a coherent imaging system is developed in the section 1.2. The fundamentals of fluorescence as well as the sources of its fluctuations are described in section 1.3. Section 1.4 presents an overview of super-resolution microscopy techniques. **Chapter 2** presents the combination of a glass prism based three-dimensional microscope with a revisited derivation of partially coherent image formation, allowing volumetric quantitative phase measurement at camera limited frame rate. **Chapter 3** describes how the aforementioned setup can be modified to perform high-resolution SIM. **Chapter 4** presents a new approach to generate high-frequency SIM pattern. The application of the setup to multi-color SIM imaging and to the combination of SOFI with SIM is also discussed and experimental results are presented. **Chapter 5** introduces a new approach for parameter-free image resolution estimation applicable, in principle, to any kind of microscopy images. Finally, **Chapter 6** presents the application of deep neural network to the field of optical DNA mapping.

1 Basic principles and methods

In the following chapter, I will review the basic principles of a microscope and the interaction of light with a sample. Since this thesis focuses on the imaging of biological sample, the discussion will be restricted to the classical interaction of light with a dielectric media. I will then introduce the general theory of fluorescence. Finally, I will present how the fluorescent emitter's properties can be exploited to achieve sub-diffraction imaging.

1.1 Microscope layout and Fourier optics

1.1.1 Bright-field microscope

The etymology of the name microscope takes it source from the Greek *micro-*, small and -*scopein*, to look at. The purpose of a microscope is to magnify the image of a microscopic object in order to make small details resolvable to the human eye or a camera.
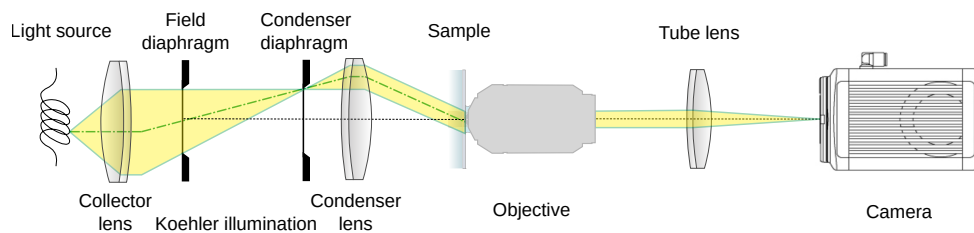
Figure 1.1 – Layout of a bright-field microscope with a Köhler illumination.

Fig. 1.1 illustrates the layout of a bright-field microscope. The light originating from the source (typically a halogen lamp) is collected by the collector lens to form the image of the filament on the condenser diaphragm. A second condenser lens is then used to redirect the light onto the sample. This configuration, known as a Köhler illumination[3], allows to produce a homogeneous illumination independently of the source shape, with a perfect control of the brightness and angle of incidence via the collector field diaphragm and condenser diaphragm.

The light interacts then with the sample, via absorption or scattering and is collected by the objective lens which can be approximated as an ideal lens with a very short focal length (typically $f_{\text{obj}} \approx 2 - 3$ mm). Finally, a tube lens (typically $f_{\text{tl}} \approx 160 - 220$ mm) is used to form the image of the sample onto the camera. The lateral magnification is given by $M = \frac{f_{\text{tl}}}{f_{\text{obj}}} \approx 50 - 100$. Typical modern camera have a physical pixel size of $\approx 6.5 - 10 \ \mu$m leading to a projected pixel size of $\approx 80 - 120$ nm for a high-resolution microscope. Such a pixel size ensures that the image of a point source spreads over 2-3 pixels, which implies that the system is limited only by the diffraction.

1.1.2 Fourier optics

One of the most remarkable properties of a lens is that it performs analog two-dimensional Fourier transform of the electro-magnetic field distribution located at a distance of the lens equal to its focal length[4]. Being able to represent a lens as a Fourier transform allows to describe an imaging system as a linear filtering operation.

Fourier Transform

The Fourier transform is a mathematical transformation developed by Jean-Baptiste Fourier (1768-1830) in 1822 for as he was working on the analytical theory of heat. In his work, Fourier claimed that any function can be expanded in a series of sines of various period and phase offsets.

The Fourier transform of an integrable function $f(x)$ is defined as

$$F(k) = \mathscr{F}\{f(x)\} = \frac{1}{\sqrt{2\pi}} \int_{-\infty}^{\infty} f(x) e^{-2\pi i x k} dx \tag{1.1}$$

From the Euler relation $e^{ikx} = \cos(kx) + i\sin(kx)$, we see that k defines the sine and cosine frequency. For each frequency k, the integral quantify *"how much"* of this particular frequency is present in the function $f(x)$. The result of the integral is generally a complex number and can be expressed as $F(k) = a(k)e^{i\phi(k)}$, where $a(k)$ is the amplitude of the sine and $\phi(k)$ is its phase.

One of the most important property of the Fourier transform, besides its Linearity, is known as the Convolution theorem, which states that the Fourier transform of the convolution of two functions is equal to the product of their individual Fourier transform.

$$\mathscr{F}\{f(x) \otimes g(x)\} = \mathscr{F}\{F(k)\}\mathscr{F}\{G(k)\} \tag{1.2}$$

where $\mathscr{F}\{\cdot\}$ denotes the Fourier transform and $\otimes$ denotes the convolution operator.

A microscope as a linear filter

As can be seen in Fig. 1.1, the detection path is composed of two lenses (the objective lens and the tube lens), each of them performing a Fourier transform. We know from the duality property of the Fourier transform that

$$\mathscr{F}\{\mathscr{F}\{U_{\text{sample}}(x)\}\} = U_{\text{camera}}(-x/M) \tag{1.3}$$

where $U(x)$ denotes the field spatial distribution at the sample or camera plane and M is the lateral magnification of the system. We see that the imaging apparatus should therefore reproduce an exact magnified copy of the field $U_{sample}(x)$[4]. However, due to the diffraction of light, only frequencies up to $1/\lambda$ (where λ is the illumination wavelength) propagate to the far-field. The effect of diffraction on the imaging can be effectively modeled by a circular aperture

$$H(k) = \begin{cases} 1, & \text{if } k < 1/\lambda \\ 0, & \text{otherwise} \end{cases} \tag{1.4}$$

which filter the object frequency spectrum, restricting the resolving power of a microscope to about λ[5].

Other imperfections of the microscope such as limited collection angle, uneven transmission of the spatial frequencies and residual phase aberrations can be modeled by modifying the amplitude and phase of the so-called transfer function $H(k)$. Assuming a magnification $M = 1$, the field at the detector is expressed as

$$U_{\text{camera}}(x) = \mathscr{F}\{\mathscr{F}\{U_{\text{sample}}(x)\}\, H(k)\} \tag{1.5}$$

This equation is a simple yet very powerful description of the image formation of a microscope and will be used throughout the whole thesis.

1.2 Coherent imaging

Coherent microscopy refers to any microscopy method that measures the interference pattern between a typically strong reference field and the field scattered by a sample after its interaction with the reference field. After the interaction, the scattered field will be attenuated, due to the sample absorption, and phase shifted with respect to the reference field. The phase shift or retardation is due to the sample refractive index and can be inferred from the measurement of the interference pattern, providing label-free structural information about the sample.

In order to understand the microscopic origin of refractive index, we rely on the atomic theory, where a dielectric media can be described as a spatial distribution of dipoles. Exposed to an oscillating electric field, the dipoles will start to oscillate and in return produce a polarization field $\mathbf{P} = \epsilon_0 \chi \mathbf{E}$ proportional but usually out of phase with the incident electric field, neglecting

the non-linear contributions. The factor ϵ_0 is called the *vacuum permittivity* and χ is the *susceptibility*. The total electric field inside the material is given by the interference of the incident field with the polarization field.

Using Lorentz model[6], we model each dipole as a damped harmonic oscillator characterized by a resonance frequency ω_0 and damping factor Γ. Under the assumption that the nuclei is too heavy to follow the field at high frequency oscillations, we can express the equation of motion of a single bound electron acted on by the Lorentz force. Solving for the stationary solution, we find a solution for the electron position with respect to its rest position. Summing up the contribution of all electrons, we obtain for the material index of refraction $n = \sqrt{1 + \text{Re}(\chi)}$

$$n^2(\omega) - 1 = \frac{4\pi N e^2}{m(\omega_0^2 - \omega^2) - i\omega\Gamma} \tag{1.6}$$

By solving for the propagation of an incident electromagnetic plane wave in a dielectric media, Ewald (1916) and Oseen (1915) demonstrated the *extinction theorem*. It states that at each point within the medium, the dipole field can be expressed as the sum of two terms. The first one is shown to have a propagation velocity or phase velocity equals to c/n while the second one exactly extinguish the incident field. Therefore an plane wave propagating through a dielectric media will accumulate a phase delay of

$$\Delta\phi = ncL \tag{1.7}$$

where L is the thickness of the dielectric media.

1.2.1 Imaging of a 2D phase object

Let us consider a thin transparent sample illuminated by a plane wave propagating along the optical axis. In first approximation, the plane wave will accumulate a phase delay $\Phi(x) = n(x)cL(x)$, with $n(x)$ the sample refractive index and $L(x)$ the sample thickness. The field transmitted by such an object can be written as

$$F(x) = e^{i\Phi(x)} \tag{1.8}$$

If we assume weak scattering ($\Phi(x) << 1$), the sum of the illumination and the scattered field can be rewritten

$$U_{\text{sample}}(x) \approx 1 + i\Phi(x) \tag{1.9}$$

where the term 1 represents the non-scattered wave and $i\Phi(x)$ the scattered wave.

We then place an ideal objective lens and image the field with a detector. Being only sensitive to the intensity of the field, we have to take the magnitude square of of the field. The image of

the object will be of the form

$$I(x) = |1 + i\Phi(x)|^2 = 1 + \Phi(x)^2 \approx 1 \tag{1.10}$$

where we assumed Φ small compared to unity.

The phase object does not produce any contrast. The essence of phase microscopy is to modify the illumination or detection path of the microscope in order to convey phase shifts into intensity fluctuations, providing label-free structural information of otherwise transparent sample.

We will now describe different methods to image transparent sample, briefly discussing their advantages and disadvantages.

Dark field microscopy

The simplest way to gain phase contrast is to place a stop in order to block the non-scattered light before it reaches the detector. The intensity will then be

$$I(x) = \Phi(x)^2 \tag{1.11}$$

Since we assume Φ small compared to unity, this approach is usually limited to highly scattering objects. Moreover, the recorded signal is not proportional to the phase.

Schlieren phase contrast

An alternative to the dark-field microscopy consists in blocking half of the detection aperture in the Fourier plane of the sample. We have

$$U_{\text{camera}}(x) = \mathscr{F}\{M(k)\mathscr{F}\{U_{\text{sample}}(x)\}\ H(k)\} \tag{1.12}$$

where $M(k) = \begin{cases} 1 & \text{for } k_x \geq 0 \\ 0 & \text{otherwise} \end{cases}$, is the Schlieren mask and k is the reciprocal space of x.

Lets suppose that we image a phase grating illuminated by a plane wave with a phase distribution $\Phi(x) = A\sin(k_g x)$, with $A << 1$ and k_g is the grating frequency. The sample field is then $U_{\text{sample}}(x) \approx 1 + Ai\sin(k_g x)$. The Fourier transform of $U_{\text{sample}}(x)$ is

$$\mathscr{F}\{U_{\text{sample}}(x)\} = \delta(0) + 0.5i A \left(\delta(k - k_g) + \delta(k + k_g)\right) \tag{1.13}$$

The effect of the mask $M(k)$ is to remove half of the Fourier components. Assuming all the Fourier components are transmitted by the transfer function $H(k)$, we have for the intensity at the camera plane

$$I(x) = \left|1 + 0.5Aie^{ik_g x}\right|^2 \approx 1 + \text{Re}\left(e^{ik_g x}\right) = 1 + A\cos(k_g x) \tag{1.14}$$

The intensity modulation is now proportional to the derivative of the phase along the orientation of the mask.

Zernike phase contrast

In 1935, F. Zernike (1888-1966) proposed a powerful and simple method to make the intensity distribution directly proportional to the phase of the object[7]. The principle is to introduce in the objective lens a phase plate that will delay the illumination field with respect to the scattered field by a factor $i = e^{i\pi/2}$. The intensity at the detector plane will then be of the form:

$$I(x) = |i + i\Phi(x)|^2 \approx 1 + 2\Phi(x) \tag{1.15}$$

Differential Interference Contrast Microscopy

Another way to gain phase contrast is to split a linearly polarized plane wave into two orthogonally polarized beam using a Wollaston birefringent prism [8]. As a consequence of the splitting, the two beams will be spatially shifted and will interact with the sample at two slightly different positions, potentially accumulating different phase shift. The two beams are then recombined using a similar Wollaston prism, forming an interference pattern proportional to the derivative of the phase in the direction of the spatial shift (see Fig. 1.2b).

Holography

Instead of looking into the interference of the illumination with the scattered field, another option, proposed by Dennis Gabor in 1948 in the context of X-ray and electron microscopy[9] consists in splitting the illumination into two fields. One field is directed towards the sample while the other propagates freely. Both fields are then recombined and interfere at the detector plane. The phase accumulated by the propagation through the sample can then be digitally recomputed from the interference pattern. Off-axis holography [10, 11] is the modern implementation of Gabor's method for phase measurement where the fields interfere at a small angle and are digitally processed to extract the complex field information.

Defocussed phase microscopy and Transport of Intensity Equation

Another method to gain phase contrast is to defocus the sample. As it will be discussed in more detail in chapter 2, the phase contrast originates from the axial analyticity of the system transfer function. However, defocused phase microscopy is limited to thin sample..

An alternative approach, named the Transport of Intensity Equation (TIE)[12] relates the axial derivative of the intensity of a coherent field to the Laplacian of its phase

$$-\frac{k}{I_0}\frac{\partial I(\mathbf{x})}{\partial z} = \nabla^2\phi \tag{1.16}$$

This expression allows to retrieve the quantitative phase of the field but is only valid for two dimensional sample and for paraxial fields.
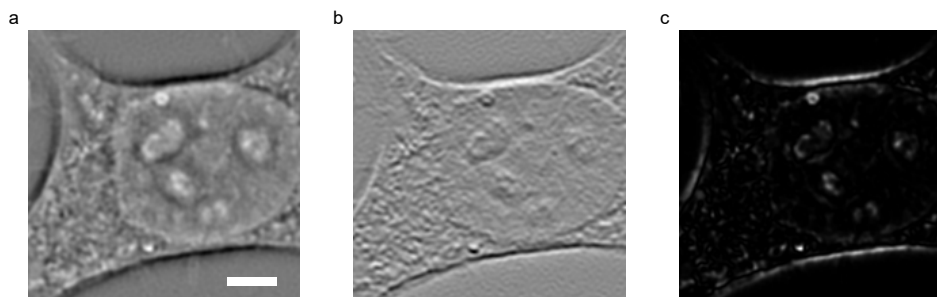
Figure 1.2 – Illustration of phase imaging (a) Input phase computed with the method discussed in chap 2. (b) Differential Interference Contrast. (c) Dark-field. Images of the same cell. Scale bar 5 μm.

1.3 Fluorescence imaging

Phase microscopy is a very powerful non-invasive tool to study cell morphology and reveal sub-cellular structures. However, it can only be used on a sample or a process that naturally exhibit refractive index contrast with respect to the surrounding medium.

In 1942, fluorescent antibody labeling was developed, paving the way to high molecular specificity imaging with unprecedented contrast[13]. Fluorescence is a process in which a molecule emits red-shifted light when irradiated with light at a lower wavelength. The frequency shift between the incident and emitted light is called the Stokes shift and is the key mechanism for high contrast as the illumination and the fluorescence signal can be efficiently decoupled using optical filters. In 1994, the cloning of the green fluorescent protein (GFP)[14] allowed in-vitro studies of protein expression of living cell by genetic encoding. The fluorescent protein gene can be incorporated as a protein marker by fusing its gene to a target gene using lipid transfection or viral transduction. Fluorescent protein can be used to monitor gene expressions or label a sub-cellular structure. Together with indirect antibody labeling, which uses a primary antibody to target a specific cellular structure and a secondary antibody to carry the fluorescent dye, it provided tools that allow to image organelles and protein distribution and to quantify interactions and molecular dynamics.

1.3.1 Photochemistry of fluorophores

Following the rules of quantum mechanics, molecules have an infinite but discrete number of energy states, essentially determined by the electron orbitals. The lower energy states are then filled with electrons according to the Pauli exclusion principle, which states that two or more identical fermions cannot occupy the same quantum state. A molecule with all its lowest energy orbital filled is said to be in the ground state.

The process of absorption corresponds to the transfer of an energy quanta of the field or photon to an electron, which will be promoted to a higher energy orbital. The absorption probability is governed by selection rules which ensure the conservation of energy and momentum. In the semi-classical picture, the molecule can be modeled as a dipole formed by the positively charged nuclei and the center of mass of the delocalized electron. The absorption probability is then proportional to the modulus squared of the dot product of the dipole moment with the incident electric field. The absorption rate is of the order $k_{ex} \approx 10^6 - 10^8 s^{-1}$.
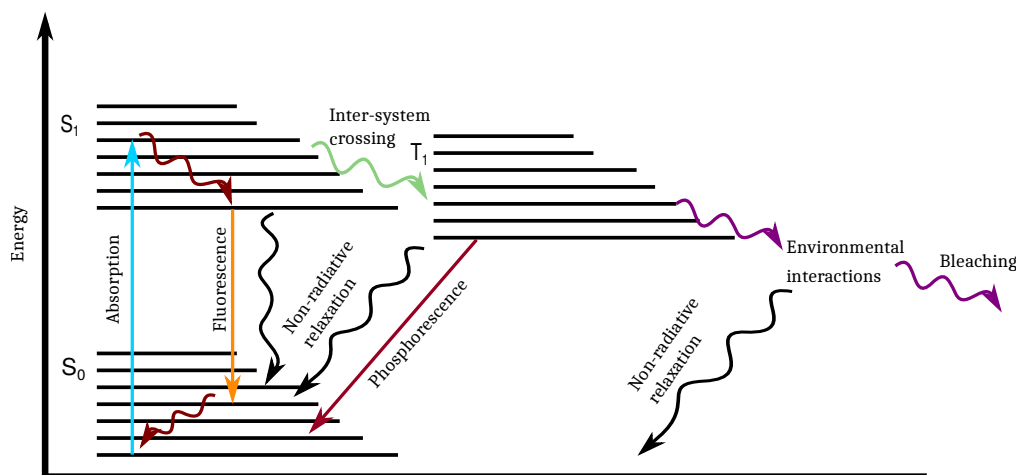
Figure 1.3 – Jablonski diagram.

Due to the interaction with its environment and vacuum fluctuations, a molecule in an excited state is bound to decay to the ground state. Several transitions are available. To each transition we can associate a characteristic time or rate, which describes the transition probability. The transitions are usually represented using a Jablonski diagram[15] (Fig. 1.3). The most common transition corresponds to the radiative decay ($k_f \approx 10^7 - 10^{10} s^{-1}$) fluorescence, where a photon is emitted following a dipole emission pattern. Due to internal non-radiative thermal relaxation($k_{tr} \approx 10^{11} - 10^{12} s^{-1}$), the energy of the emitted photon is red-shifted compared to the energy of absorbed photon. This is called the Stoke-shift[16]. The red-shifted emission allows to decouple the excitation and detect only the fluorescence signal. The electron can also transition to the ground state through non-radiative decay ($k_{nr} \approx 10^9 - 10^{11} s^{-1}$), or transition to a triplet state via inter-system crossing ($k_{isc} \approx 10^6 - 10^{10} s^{-1}$), where the excited electron has the same spin as the ground electron. The triplet state has a long lifetime as the direct transition from the triplet state to the ground state is forbidden by the Pauli exclusion principle. The process in which a photon is emitted by a transition from an excited triplet state to the ground state is called phosphorescence ($k_p \approx 10^{-2} - 10^4 s^{-1}$).

While in the long lived excited triplet state, the molecule is more likely to interact with other species. One possible result of this interaction is irreversible photobleaching, where the molecule loses its ability to emit fluorescence. The molecule can also change into a meta-stable reduced non-fluorescent state or OFF state[17, 18]. In opposition to photobleaching,

the molecule can return to a fluorescent or ON state. The change to the OFF state is called photo-switching and is used in super-resolution microscopy to temporally separate single emitters and localize them with a precision smaller than the diffraction limit. Other switching mechanisms involve cis-trans isomerization, hydration-dehydration reaction or absorption of near-UV photons[15].

1.3.2 Incoherent image formation and resolution

Fig. 1.4a shows the implementation of an epi-illumination fluorescence microscope. A laser source is focused on the back-focal plane of the objective lens to produce a Gaussian-shaped illumination profile. A fraction of the fluorescence light is then collected by the objective and transmitted by the dichroic. The numerical aperture (NA) of an objective is defined as $NA = n\sin\theta$, where n is the refractive index of the medium between the object and the objective and θ the collection angle. The larger the NA, the higher the resolving power. An emission filter is usually required to suppress spurious reflections of the intense laser light. Using a tube lens, the fluorescence light is then focused on the camera to form an image of the sample.

Due to its stochastic nature, the field emitted by two fluorophores does not exhibit spatial or temporal correlations. The fluorescent light is said to be incoherent. Consequently the intensity distribution of the image of a distribution of fluorescent molecules can be expressed as a sum of the intensity of each molecules

$$I(\mathbf{x}) = \sum_i^N A_i U(\mathbf{x} - \mathbf{x_i}) \tag{1.17}$$

where A_i is the brightness of the molecule and $U(\mathbf{x} - \mathbf{x_i})$ is the microscope point-spread function shifted at the molecule location and $\mathbf{x_i}$ is the molecule location.

The resolving power of a microscope is characterized by its point-spread function, which describes how a point source is blurred by the unavoidable diffraction, the limited numerical aperture of the objective lens and the optical aberrations of the optical component used.

Using the convolution theorem, the Fourier transform of the intensity distribution $I(\mathbf{k})$ can be expressed in terms of the Fourier transform of the emitters spatial distribution, also called object function $F(\mathbf{k})$ and the Fourier transform of the point-spread function (see Fig. 1.4) $OTF(\mathbf{k})$, the optical transfer function. We have

$$I(\mathbf{k}) = OTF(\mathbf{k})\,F(\mathbf{k}) \tag{1.18}$$

where $\mathbf{k}$ is the reciprocal space of $\mathbf{x}$.

The OTF can itself be defined as the auto-correlation of the pupil function $P(\mathbf{k})$, a complex function that describes the transmission in amplitude and phase of an optical system. The phase of the pupil function contains all the information about the aberrations present in the

system. A constant phase corresponds to a diffraction limited imaging system and corresponds to the highest resolving power for a given wavelength and numerical aperture. The phase of the pupil function can be decomposed into Zernike coefficients[19], allowing to classify and categorize the many type of aberrations that can occur in the design and alignment of an optical system.
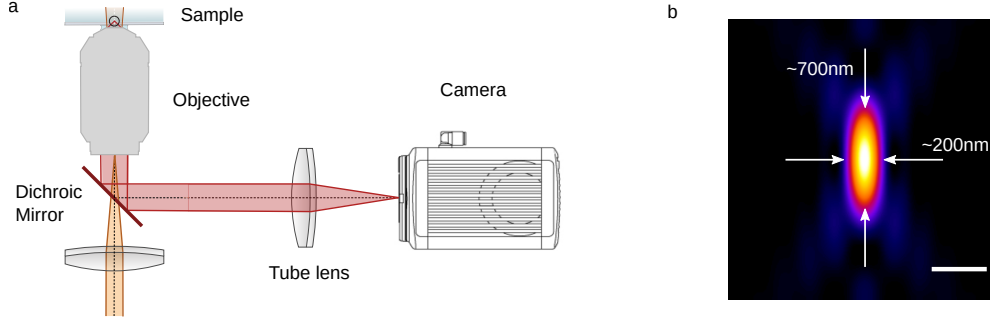
Figure 1.4 – (a) Epi-fluorescence setup (b) Incoherent three-dimensional PSF generated using the "PSF Generator" imageJ plugin [20], $NA = 1.4, \lambda = 560$ nm. Scale bar μm.

In order to understand the 3D image of point source, the pupil function has to be projected on the so called *Ewald sphere*[21]. The *Ewald sphere* lives in the reciprocal space **k** and has a radius equal $n\frac{2\pi}{\lambda}$ where n is the refractive index of the immersion media and λ is the main wavelength of the fluorescent emission. The 3D OTF is then naturally given by taking the auto-correlation of the projected pupil function.

Following Abbe principle, the lateral resolution achievable by an optical system is then given by the highest lateral spatial frequency with non-zero value. Expressed in nanometer, the resolution when imaging an incoherent self-luminous object is given by

$$\delta_\perp = \frac{\lambda}{2NA} \tag{1.19}$$

Similarly, the axial resolution can be defined as the highest axial frequency with non-zero value. We have

$$\delta_z = \frac{\lambda}{2\left(n - \sqrt{n^2 - NA^2}\right)} \tag{1.20}$$

While being a very powerful guidance in the design of optical system, theses concepts remain theoretical. They do not provide any information about the actual performance of a real system, only the theoretically ideal achievable resolution. In particular the crucial notion of noise and signal-to-noise ratio is not considered at all by this definition. The potential issue of residual aberrations, motion blur due to sample drift and the degradation of image quality due to out-of-focus background are also important practical aspect that cannot be modeled in a general formula.

There exists therefore a need for a method, compatible with the theoretical framework described above, that is able to estimate the resolution directly from the image. A solution to this problem is presented in chapter 4.

1.4 Super-resolution imaging

While providing high contrast and specificity at the molecular level, fluorescence microscopy has been for a long time limited to resolutions in the order of 200 nm, which is about two order of magnitude larger than routinely achievable electron microscopy image. In 1928, Edward Synge laid out the idea of a near-field scanning microscope, where a sub-diffraction aperture placed a few nanometers above the surface is used to illuminate or collect evanescent waves that do not propagate in the far-field. After solving the many technical issues, a resolution of $\lambda/60$ was reported by Ash and Nicholls[22]. In the early 2000, several far-field techniques have been proposed to go beyond the diffraction limit. An important conceptual aspect which applies to all methods is that they are all exploiting some a-priori knowledge about the sample, which can then be exploited to improve the spatial resolution. This gain of resolution is usually associated with an increase in the total acquisition time.

Super-resolution methods can be divided into two categories: patterned illumination and stochastic imaging. The first category exploits photo-physical properties of the fluorophores such as stimulated emission or saturation of the fluorescence. Theses approaches involve a non-linear response of the sample. The second category exploits uncorrelated fluctuations of fluorescent emitters to separate them beyond the diffraction limit.
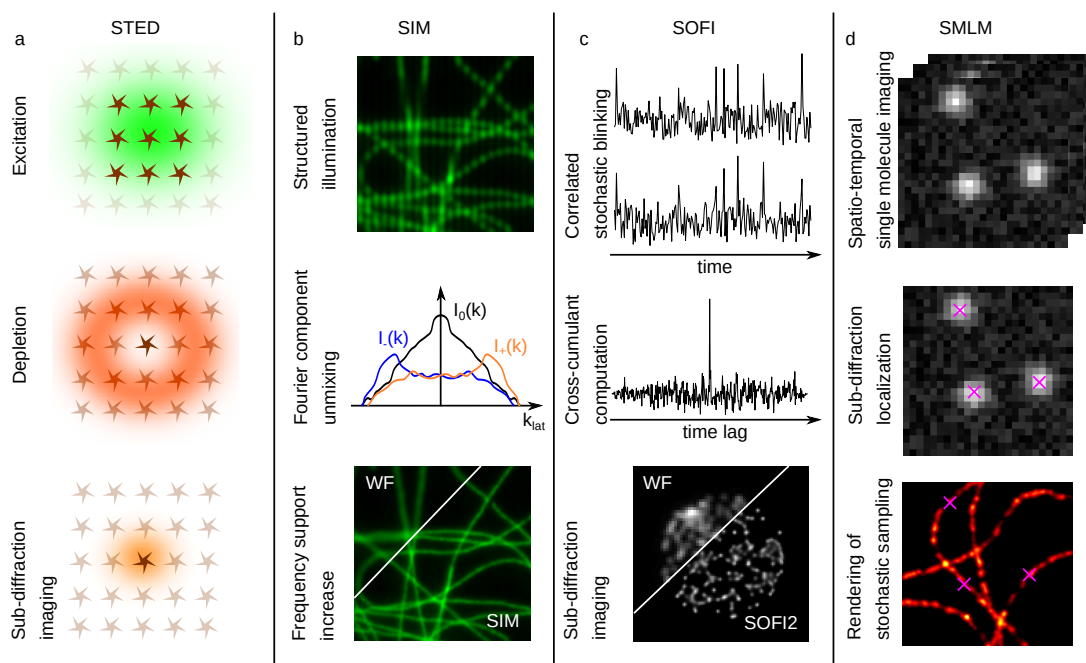

Figure 1.5 – Overview of super-resolution microscopy (a) STED (b) SIM (c) SOFI (d) Localization microscopy.

1.4.1 Stimulated Emission Depletion Microscopy (STED)

Stimulated emission is one mode of interaction of a photon with an excited two level system. In this process, the incoming photon trigger the two-level system decay to the ground state, emitting a new photon, with a phase, frequency, polarization and momentum identical to the incident photon.

The approach to exploit this property can be decomposed in two steps. First the fluorophores are excited by a diffraction limited laser spot. If we wait until the molecules spontaneously decay and count all the photons emitted, the signal will be approximately proportional to the number of molecules present in the laser spot and no gain in resolution will be achieved. The second step consists in depleting a fraction of the fluorophores using a torus or donut-shaped diffraction limited beam whose central minimum coincide with the maximum of the Gaussian excitation. The subsequently recorded signal can therefore only originate from a much narrower volume. The resolution gain is proportional to the depletion cross-section. We have

$$\delta_{STED} = \frac{\lambda}{2\text{NA}\sqrt{1 + \frac{I}{I_{sat}}}} = \frac{\delta_\perp}{\sqrt{1 + \frac{I}{I_{sat}}}} \tag{1.21}$$

where $\delta_\perp$ is the wide-field resolution, I is the depletion laser beam intensity and I_{sat} is the saturation intensity, defined as as the intensity at which the stimulated emission gain drops to half of the gain approximation for small incident depletion intensity.

We note that the resolution achieved by STED microscopy is, in principle, arbitrary small provided high enough depletion intensity and perfect shape of the STED beam[23–25]. In practice however, the relatively high power density of the STED beam, the depletion cross-section of the fluorophore, the residual aberration of the STED pattern and signal to noise limit the achievable resolution. The need also exists for a method to assess the resolution directly from the recorded image. A resolution of about 2.5 nm has been demonstrated on solid-state samples[26], where photo-bleaching and high-power densities is not an issue.

By modifying the shape of the depletion beam, STED super-resolution can also be achieved in 3D. The gain in axial resolution (≈ 100 nm), however, comes at the cost of a lower lateral resolution in practice[27, 28].

1.4.2 Structured Illumination Microscopy (SIM)

The inclusion of SIM[29–31]among other super-resolution methods is sometimes contested as the linear version of SIM is limited to a 2-fold resolution improvement. SIM exploits the fact that the fluorescence signal is proportional to the illumination intensity, which is a non-linear response with respect to the electric field. This non-linearity allows to access information beyond the cut-off frequency[32] of the microscope by a clever patterning of the illumination.

While the first implementation of SIM was using a sinusoidal pattern, it was recognized that a Gaussian illumination is also one form of structured illumination which also achieve

increased resolution[33]. While its first implementation, termed image scanning microscopy, [34], involved scanning of the sample and numerical rescaling, a more recent approach, termed iSIM, proposed an all optical parallel implementation, dramatically increasing the imaging speed at the cost of a more complex setup[35].

The non-linear version of SIM, also called saturated SIM[36] exploit the fact that, beyond a certain intensity threshold, the fluorescence signal saturate. The illumination sinusoidal pattern appears then truncated. This saturation is the source of high order non-linearity that can be used to achieve an arbitrarily small resolution, in principle. While being interesting conceptually, this method is however extremely inefficient in terms of photon budget and bleaching.

We will now focus on the case of a linear sinusoidal pattern. Such a pattern can be realized by two crossing beams interfering in the sample plane. The two beams are usually generated by a phase grating placed in a conjugated sample plane. The use of a pixelated digital micro-mirror device [37] or transmissive liquid crystal[38] was also proposed as a faster way to change the illumination pattern, usually at the cost of higher losses in the illumination path.

The intensity distribution under an idealized patterned illumination is given by

$$I(\mathbf{x}) = \left[O(\mathbf{x})\, 0.5(1 + \cos(\mathbf{x} \cdot \mathbf{k}_i + \phi)) \right] \otimes psf(\mathbf{x}) \tag{1.22}$$

where $O(\mathbf{x})$ is the spatial distribution of fluorescent labels, $\mathbf{k}_i$ is the wave-vector, defining the period and direction of the oscillating pattern, ϕ is the phase offset, determining the position of the maxima relative to the optical axis, $psf(\mathbf{x})$ is the point-spread function of the imaging setup and $\otimes$ is the convolution operator. A trivial but crucial aspect of the method is that the point-spread function physically acts on the image *after* the interaction of the illumination with the sample.

We have in Fourier space

$$I(\mathbf{k}, \phi) = \left[O(\mathbf{k}) \otimes (\delta(0) + 0.5e^{\pm i\phi}\delta(\mathbf{k} \pm \mathbf{k}_i)) \right] OTF(\mathbf{k}) = I_0(\mathbf{k}) + 0.5I_{\pm}(\mathbf{k} \pm \mathbf{k}_i) \tag{1.23}$$

We see that the illumination added two components to the object spectrum, phase shifted by a factor ϕ and frequency shifted by a factor $\mathbf{k}_i$. If we simplify the effect of the $OTF(\mathbf{k})$ to act as an ideal low-pass filter with a cut-off frequency k_c, we see that the frequency shifted component contains high frequency information that is not present in the central component. The three components are however overlapping and no sub-diffraction resolution can be achieved at this point. In order to unmix the three components, the solution is to acquire at least three images with different pattern phases ϕ.

The situation is best described in matrix form

$$\begin{bmatrix} I(\mathbf{k}, \phi = 0) \\ I(\mathbf{k}, \phi = 2\pi/3) \\ I(\mathbf{k}, \phi = 4\pi/3) \end{bmatrix} = \begin{pmatrix} 1 & 0.5 & 0.5 \\ 1 & 0.5e^{i2\pi/3} & 0.5e^{-i2\pi/3} \\ 1 & 0.5e^{i4\pi/3} & 0.5e^{-i4\pi/3} \end{pmatrix} \begin{bmatrix} I_0(\mathbf{k_0}) \\ I_+(\mathbf{k} + \mathbf{k}_i) \\ I_-(\mathbf{k} - \mathbf{k}_i) \end{bmatrix} \tag{1.24}$$

which can be inverted to retrieve the three components I_0, I_+ and I_-. Finally the components have to be shifted by the illumination pattern frequency $\mathbf{k}_i$ and added to form the final SIM image. The frequency support, i.e. the resolution, of the SIM image is then $k_c + |\mathbf{k}_i|$ along the direction of $\mathbf{k}_i$. To achieve quasi isotropic resolution improvement, the whole procedure has to be repeated in at least three directions.

The non-trivial step in the reconstruction of a SIM image is the accurate estimation of the pattern frequency and phases[39–41]. Imperfect SIM reconstructions typically show well known artifacts[42].

In order to increase the resolution along the axial direction, a third on-axis beam has to be added, providing axial modulation of the intensity[43]. While it requires the acquisition of two additional phases shifts and adequate axial sampling, the reconstruction is essentially similar to the 2D case.

1.4.3   Single Molecule Localization Microscopy (SMLM)

Sub-diffraction microscopy can also be achieved by imaging stochastically blinking fluorophores[44] over time. Assuming that a sufficiently small fraction of the emitters are in the ON state such that their point-spread function do not spatially overlap, the center of mass of each molecule can be numerically estimated with a spatial precision far beyond the diffraction limit. The gain in spatial resolution is traded with temporal resolution as the acquisition of many camera frames will be required to sample the underlying structure.

Three main mechanism are routinely used to achieve sparse blinking. Direct Stochastic Optical Reconstruction Microscopy ((d)STORM, [45–47]) uses reversible switching to a metastable dark state, either by employing specific buffer solution or multiple lasers. Photo-Activated Localization Microscopy (PALM, [48, 49]) uses dyes that can be photoactivated, imaged and consequently bleached. Finally Point Accumulation for Imaging in Nanoscale Topography (PAINT, [50, 51]) uses the stochastic and transient binding of diffusing dyes in solution with a complementary molecule bound to the target structure.

Using a standard diffraction limited microscope, it is very challenging to localize the molecule position along the axial direction due to the limited depth-of-field. However, by carefully adding aberrations to the system, the most common being astigmatism[52, 53], it is possible to trade lateral localization precision for axial precision and increased depth of field. This type of aberration breaks the symmetry of the point-spread function and encodes the axial position in its shape. Alternative approaches such as biplane microscopy[54, 55], double-helix psf[56],

self-bending psf[57], self-interfering psf [58] and illumination modulation [59] have also been proposed to span the trade-off between the probing depth, the axial localization precision and the penetration depth.

More recently, a combination of STED and localization microscopy, termed minFlux, was proposed[60, 61], which uses a donut shaped illumination to probe the fluorescent molecules. Assuming there is only one molecule in the ON-state within the diffraction limited area, the photon statistics become a function of the position of the fluorescent molecule with respect to the donut excitation. By translating the illumination pattern and trying to minimize the fluorescence signal, it is possible to iteratively localize the position of the molecule down to the nanometer size while using as few photons as possible.

1.4.4 Image formation and resolution in localization microscopy

The *"image formation"* of a localization microscopy experiment is quite different from other microscopy techniques in the sense that the resulting image is entirely artificial and do not contain noise.

Standard localization algorithms work as follow. First the raw image is filtered in order to enhance the signal coming from single emitters. All local maxima above a given threshold are then identified. The image of all potential single emitter is then extracted and fitted to estimate the position of the fluorophore. The presence of many sources of noise in the intensity signal, limited photon budget, multiple emitters and finite sampling of the point-spread function limit the localization precision and accuracy. Under the assumption of shot-noise limited signal and a Gaussian shaped point-spread function, the localization uncertainty[62] is

$$\sigma_{\perp} = \frac{\sigma_a^2}{N} \left(\frac{16}{9} + \frac{8\pi\sigma_a^2 b^2}{Na^2} \right) \tag{1.25}$$

where $\sigma_a = \sigma^2 + a^2/12$, σ is the standard deviation of the point-spread function, a is the camera projected pixel size, N is the number of photon from the emitter and b is the average photon background per pixel. While nanometer and subnanometer localization microscopy have been demonstrated, a typical localization microscopy experiment achieves a localization uncertainty of about 15-30 nm[63].

All the localizations can then be filtered based on the results of the fitting operation and rendered as a histogram, Gaussian with standard deviation equal to the localization uncertainty or using more advanced rendering methods[64].

The resolution of localization microscopy experiments is discussed in Chapter 4.

1.4.5 Stochastic Optical Fluctuation Imaging (SOFI)

Instead of relying on the fitting of sparsely blinking emitter, sub-diffraction imaging can also be achieved through the statistical analysis of the fluorescence fluctuation. Stochastic Optical Fluctuation Imaging (SOFI, [65–68]) proposes to compute spatio-temporal cross-cumulant of a sequence of blinking emitters. SOFI can be applied to any fluctuating signal provided the three following conditions are fulfilled:

- The fluctuations should originate from two visibly distinct states

- The fluctuations should be stochastic and independent

- The Nyquist sampling criterion has to be fulfilled

Following these three rules, the signal of an emitter is only correlated with itself, in space and time. Making use of the additivity property of cumulants, the signal originating from each emitter can be processed independently and the resolution increased by a factor $\sqrt{n}$ where n is the cumulant order.

1.4.6 Cumulants

Cumulants are an infinite set of quantities that describe a probability distribution. Compared to moments, the key property of cumulants is their additivity, which entails that the cumulant of the sum two independent variables is the sum of their cumulants.

Since a probability distribution can be equivalently represented by an infinite set of moment, both quantities are intimately linked. We start by reminding the definition of the nth moment of a real-valued continuous function around 0

$$\mu_n = \left\langle f_n(x) \right\rangle = \int_{-\infty}^{\infty} x^n f(x) dx \tag{1.26}$$

The moments can also be derived from the characteristic function

$$\Phi_X(t) = \left\langle e^{itX} \right\rangle \tag{1.27}$$

where $\langle \cdot \rangle$ denotes the expectation value. The Taylor expansion of e^{itX} gives

$$\Phi_X(t) = \int_{-\infty}^{\infty} \left[1 + it\langle X \rangle + \frac{i^2 t^2 \langle X^2 \rangle}{2!} + ... \right] f(x) dx \tag{1.28}$$

The nth order moment, coefficient of the nth term, is then obtained by taking the nth order derivative of the characteristic function at $t = 0$

$$\mu_n = i^{-n} \left[\frac{\delta^n \Phi_X(t)}{\delta t^n} \right]_{t=0} \tag{1.29}$$

The cumulants κ_n are then similarly defined as the coefficients of the Taylor expansion of the cumulant characteristic function

$$\Psi_X(t) = ln(\Phi(t)) = \sum_{n=0}^{\infty} i^n \kappa_n \frac{t^n}{n!} \tag{1.30}$$

1.4.7 Image formation of SOFI

As already stated before, the stochastic intensity fluctuation of fluorophores can be exploited to achieve super-resolution. For a given set of stochastically blinking fluorophores, the intensity signal can be written as

$$I(\mathbf{x}, t) = \sum_{i}^{N} A_i U(\mathbf{x} - \mathbf{x_i}) s_i(t) + b(\mathbf{x}) + n(\mathbf{x}, t) \tag{1.31}$$

where A_i is the molecule brightness, $U(\mathbf{x})$ is the microscope point-spread function, $\mathbf{x_i}$ is its position, $s_i(t) \in [0, 1]$ is the signal fluctuation over time, $b(\mathbf{x})$ is the constant background signal and $n(\mathbf{x})$ is the uncorrelated noise.

Using the semi-invariance and additivity properties, we have for the cumulant of the intensity

$$\kappa_n(\mathbf{x}) = \sum_{i}^{N} A_i^n U^n(\mathbf{x} - \mathbf{x_i}) \kappa_n\{s_i(t)\} + \kappa_n\{b(\mathbf{x})\} + \kappa_n\{n([x], t)\} \tag{1.32}$$

The resolution increase of the nth order SOFI image $\kappa_n(\mathbf{x})$ is due to the raising of the system point-spread function to the nth power. We know from the Fourier transform properties that the Fourier transform of a function raised to the nth power is given by the nth auto-correlation of the Fourier transform of the function. The frequency support of the SOFI image is then increased by a factor n. However, the auto-correlation do not preserve the shape of the transfer function. The effective resolution improvement is therefore closer to $\sqrt{n}$ and a deconvolution/Fourier reweighing operation is required to flatten the transfer function and get closer to the ideal resolution improvement factor of n. There is no fundamental limit in computing high order SOFI image to reach nanometric resolution, however it is limited in practice by the signal to noise ratio which decreases with the cumulant order. The other problems concerning the fixed pixel size, the non-vanishing noise term and the non-linear response to brightness can be solved by introducing cross-cumulant and additional post-processing.

Cross-cumulants exploit spatio-temporal correlations to enhance the fluorescence signal while suppressing the uncorrelated pixel noise. Formally, the nth order cross-cumulant from the n positions $\mathbf{x} = \{\mathbf{x_1}, \mathbf{x_2}, ..., \mathbf{x_n}\}$ and the n time lags $\tau = \{\tau_1, \tau_2, ..., \tau_n\}$ is

$$\kappa_n(\mathbf{x}, \tau) = \sum_{i=1}^{N} A_i^n \left[\prod_{k=1}^{n} U(\mathbf{x_k} - \mathbf{x_i}) \right] \kappa(s_i(t - \tau)) \tag{1.33}$$

The product $\prod_{k=1}^{n} U(\mathbf{x_k} - \mathbf{x_i})$ can be interpreted as a distance dependent factor which depends on the system point-spread function. The equation 1.33 provides the cumulant at the position $\mathbf{x}' = \frac{1}{n}\sum_{i}^{n}\mathbf{x_i}$. Since the position $\mathbf{x}'$ might be in between physical pixels, it can be used to increase the image sampling.

SOFI resolution improvement naturally expands in 3D. If the volume is acquired plane by plane, the axial resolution is however not increased as there will be no temporal correlations between two adjacent planes. The solution consists in acquiring two or more planes simultaneously, allowing to compute cumulants in all directions and to increase the inter-plane sampling[69].

2 Three-dimensional partially coherent quantitative phase microscopy

Super-resolution fluorescence microscopy provides unprecedented insight into cellular and subcellular structures. However, going 'beyond the diffraction barrier' comes at a price, trading temporal for spatial super-resolution. We combine a novel label-free white light quantitative phase imaging with fluorescence to provide high-speed imaging and spatial super-resolution. We realized multi-plane imaging using a customized prism for the simultaneous acquisition of 8 planes. This allowed us to not only image live cells in 3D at up to 200 Hz, but also to integrate fluorescence super-resolution optical fluctuation imaging within the same optical instrument.

The following chapter is based on a reorganized version of two published / submitted manuscripts

Descloux, A.[1], Grußmayer, K.S.[1], Bostan, E.[2], Lukes, T.[1], Bouwens, A.[1], Sharipov, A.[1], Geissbuehler, S.[1], Mahul-Mellier, A.L.[3], Lashuel, H.A.[3], Leutenegger, M.[1] and Lasser, T.[1], 2018. Combined multi-plane phase retrieval and super-resolution optical fluctuation imaging for 4D cell microscopy. Nature Photonics, 12(3), pp.165-172.

A.D. and K.S.G. contributed equally to this work. T.L. and A.D. initiated the project and wrote the theory/modelling. A.D. developed the phase retrieval algorithm and simulations. K.S.G., A.D., T.L. and A.S. designed the experiments. K.S.G. prepared and performed the experiments. A.-L. M.-M. prepared the neuron samples. A.D., K.S.G. and T.Lu. analysed the data. M.L., S.G. and T.L. designed the optical system including the image splitting prism. S.G. and A.S. built the microscope setup. E.B., A.B. and H.A.L. provided research advice. A.D., K.S.G. and T.L. wrote the manuscript with contributions from all authors.

Descloux, A.[1], Neuenschwander, M.[4], Hannebelle, M.T.M.[4], Fantner, G.E.[4], Radenovic, A.[1] and Lasser, T.[1], 2019. Tomographic Phase Retrieval: A 3D reformulation of the Transport of Intensity Equation for non-paraxial fields.

A.D. and T.L. initiated the project. M.N and M.H. prepared the phase sample. T.L., G.F and A.R. provided research advices. A.D. wrote the manuscript with contributions from all authors.

---

[1]LBEN and LOB, EPFL, 1015 Lausanne, Switzerland
[2]BIG , EPFL, 1015 Lausanne, Switzerland
[3]LMNN , Brain Mind Institute, EPFL, 1015 Lausanne, Switzerland
[4]LBNI , EPFL, 1015 Lausanne, Switzerland

2.1 Polychromatic light scattering

2.1.1 Monochromatic scattering

Following the seminal work of Born & Wolf[6], we consider a monochromatic scalar electromagnetic field $U(\mathbf{x})$ at frequency ω (assuming a slowly varying refractive index $n(\mathbf{x})$). This electromagnetic field has to satisfy the Helmholtz equation[1]

$$(\nabla^2 + k_0^2 n^2(\mathbf{x})) U(\mathbf{x}) = 0 \tag{2.1}$$

where $\mathbf{x} = (x, y, z)$ is the spatial coordinate, $\nabla^2 = \frac{\partial^2}{\partial x^2} + \frac{\partial^2}{\partial y^2} + \frac{\partial^2}{\partial z^2}$ is the Laplacian operator, $k_0 = \frac{\omega}{c} = \frac{2\pi}{\lambda}$ the wavenumber of the electromagnetic field in vacuum and $n(x)$ being the spatial refractive index distribution of the sample.

Equation 2.1 cannot be solved in general due to the spatially varying refractive index. We therefore take the index of refraction to vary around the mean refractive index $\bar{n}$. Equation 2.1 can now be rewritten as

$$(\nabla^2 + k_0^2 \bar{n}^2) U(\mathbf{x}) = -F(\mathbf{x}) U(\mathbf{x}) \tag{2.2}$$

where $F(\mathbf{x}) = k_0^2 (n^2(\mathbf{x}) - \bar{n}^2)$ is the scattering potential.

The left-hand side of equation 2.2 is the homogeneous wave equation, whereas the right hand side represents a source term containing the scattering potential $F(\mathbf{x})$.

Outside of the scattering volume [70], the total field is written as a superposition of the incident field and the scattered field

$$U(\mathbf{x}) = U_i(\mathbf{x}) + U_s(\mathbf{x}). \tag{2.3}$$

Using the homogeneous Helmholtz equation for the incident field $U_i(\mathbf{x})$, we obtain

$$(\nabla^2 + \bar{n}^2 k_0^2) U_i(\mathbf{x}) = 0. \tag{2.4}$$

By combining equations 2.2 and 2.3 and using 2.4, we write for the scattered field $U_s(\mathbf{x})$, which

---

[1] Throughout all the calculations we use the same notation for the intensity and its Fourier transformed spectrum. The distinction is made by explicitly noting the variable x or g and the bold font is reserved for the spatial coordinates in three dimensions, i.e. $\mathbf{x} = (x, y, z)$ and $\mathbf{g} = (g_\perp, g_z)$, with $g_\perp$ shorthand for (g_x, g_y). The wavenumber, i.e. the magnitude of the wave vector, is denoted as $k_0 = \sqrt{k_\perp^2 + k_z^2} = \frac{2\pi}{\lambda} = \frac{\omega}{c}$.

satisfies the inhomogeneous Helmholtz equation

$$[\nabla^2 + k_0^2 \bar{n}^2] U_s(\mathbf{x}) = -F(\mathbf{x}) U(\mathbf{x}). \tag{2.5}$$

Using a Green's function ansatz[6] we write

$$[\nabla^2 + k_0^2 \bar{n}^2] G(\mathbf{x} - \mathbf{x}') = -\delta(\mathbf{x} - \mathbf{x}') \tag{2.6}$$

where $\delta(\mathbf{x} - \mathbf{x}')$ is the 3D Dirac function.

Approximating the far-field response of a point scatterer as a spherical wave, we have

$$G(\mathbf{x} - \mathbf{x}') = \frac{e^{ik_0|\mathbf{x} - \mathbf{x}'|}}{|\mathbf{x} - \mathbf{x}'|}. \tag{2.7}$$

Because the scattered field is much weaker than the incident field (first-order Born approximation), we neglect the scattered field in comparison to the dominant incident field. We obtain outside of the scattering volume V_s for the scattering field

$$U_s(\mathbf{x}) = \int_{V_s} G(\mathbf{x} - \mathbf{x}') F(\mathbf{x}') U_i(\mathbf{x}') d^3\mathbf{x}' \tag{2.8}$$

This represents a 3D convolution of the source term $F(\mathbf{x}') U_i(\mathbf{x}')$ with the Green's function. The Green's function (equation 2.7) can be expressed by a series expansion (Weyl's expansion of a spherical wave in terms of plane waves) in the lateral coordinate x and y as [70],[5]

$$G(\mathbf{x} - \mathbf{x}') = \frac{i}{2\pi k_z} \iint_{-\infty}^{\infty} e^{i(k_x(x-x') + k_y(y-y') + k_z(z-z'))} dk_x dk_y. \tag{2.9}$$

Inserting equation 2.9 into 2.8 and taking a Fourier transform, we use the convolution theorem and obtain for $U_s(k;z)$ in Fourier space

$$U_s(\mathbf{k};z) = \frac{i}{k_z} e^{ik_z z} \left[F(\mathbf{g}) \otimes_k U_i(\mathbf{g}) \right], \tag{2.10}$$

where $\mathbf{g}$ is the object spatial frequency space and $\mathbf{k}$ is the scattered field spatial frequency space, $\otimes_{\mathbf{k}}$ is the convolution operator evaluated at $\mathbf{k}$, $e^{ik_z z}$ represents the propagation of the wave and $k_z = \bar{n} k_0 \cos(\theta_{det})$ represents the projection of the scattering vector $\mathbf{k}$ onto the optical axis (where we follow the derivation of Singer et al.[70]).

Assuming a monochromatic plane wave (in Fourier space) with an amplitude A, propagating

along the direction $\mathbf{k}_i$ for the incident field $U_i\left(\mathbf{g};\mathbf{k}_i\right)$, expressed as

$$U_i\left(\mathbf{g};\mathbf{k}_i\right) = A\delta\left(\mathbf{g}-\mathbf{k}_i\right), \tag{2.11}$$

and neglecting the propagation term ($z = 0$), we obtain a general expression where the scattered field appears as an interaction of the illumination field and the scattering potential, given as

$$U_s\left(\mathbf{k};\mathbf{k}_i\right) = iA\frac{F\left(\mathbf{k}-\mathbf{k}_i\right)}{k_z}. \tag{2.12}$$

The object spectrum or scattering potential is interrogated by the illumination field, represented by its wave vector $\mathbf{k}_i$. The scattering event results in a plane wave with an amplitude $U_s\left(\mathbf{k};\mathbf{k}_i\right)$, propagating along the direction $\mathbf{k}$.

2.1.2 Coherent Transfer Function

The microscope is modeled as a telecentric, diffraction limited optical imaging system. The microscope is fully characterized by the source spectrum and the illumination and detection Numerical Aperture (NA_{ill}, NA_{det}). Due to the limited bandwidth of our detection system (sCMOS camera), the intensity is described by a temporal average (denoted $\langle\,\rangle$) of the interference between the scattered and un-scattered field and integrated over the source spectrum ω and the angular spectra $(\mathbf{k}_i, \mathbf{k})$.

$$I\left(\mathbf{x}\right) = \left\langle\left|\int_{\omega,\mathbf{k}_i,\mathbf{k}}\left(U_i\left(\mathbf{x};\omega,\mathbf{k}_i\right) + U_s\left(\mathbf{x};\omega,\mathbf{k}_i,\mathbf{k}\right)\right)d\mathbf{k}d\mathbf{k}_id\omega\right|^2\right\rangle. \tag{2.13}$$

with $U_i\left(\mathbf{x};\omega,\mathbf{k}_i\right) = A(\omega)\,e^{i\mathbf{x}\cdot\mathbf{k}_i}$ and $U_s\left(\mathbf{x};\omega,\mathbf{k}_i,\mathbf{k}\right) = iA(\omega)\frac{F(\mathbf{k}-\mathbf{k}_i)}{k_z}e^{i\mathbf{x}\cdot\mathbf{k}}$.

Developing the equation 2.13, we decompose the intensity into a sum of mutual intensities as

$$I\left(\mathbf{x}\right) = \left\langle\int_{\omega',\mathbf{k}_i'}\int_{\omega'',\mathbf{k}_i''}U_i\left(\mathbf{x};\omega',\mathbf{k}_i'\right)U_i^*\left(\mathbf{x};\omega'',\mathbf{k}_i''\right)d\omega'd\mathbf{k}_i'd\omega''d\mathbf{k}_i''\right\rangle +$$

$$\left\langle\int_{\omega',\mathbf{k}_i',\mathbf{k}'}\int_{\omega'',\mathbf{k}_i''}U_s\left(\mathbf{x};\omega',\mathbf{k}_i',\mathbf{k}'\right)U_i^*\left(\mathbf{x};\omega'',\mathbf{k}_i''\right)d\omega'd\mathbf{k}_i'd\mathbf{k}'d\omega''d\mathbf{k}_i''\right\rangle + c.c. \tag{2.14}$$

where *c.c.* denotes the complex conjugate term $U_s^*U_i$. We neglected the weak $U_sU_s^*$ contribution due to the weak scattering approximation.

Using the generalized Wiener-Khintchine theorem [71], the mutual intensity of two fields is only non-zero for $\omega' = \omega''$. Following the work of N. Streibl[72], which applies for a telecentric configuration and a Koehler illumination, the mutual intensity is non-zero only for $\mathbf{k}_i' = \mathbf{k}_i''$.

We then obtain

$$I(\mathbf{x}) = \int_{\omega,\mathbf{k}_i} U_i(\mathbf{x};\omega,\mathbf{k}_i) U_i^*(\mathbf{x};\omega,\mathbf{k}_i) \, d\omega d\mathbf{k}_i +$$

$$\int_{\omega,\mathbf{k}_i,\mathbf{k}} U_s(\mathbf{x};\omega,\mathbf{k}_i,\mathbf{k}) U_i^*(\mathbf{x};\omega,\mathbf{k}_i) \, d\omega d\mathbf{k}_i d\mathbf{k} + c.c. \tag{2.15}$$

The first term represents the unscattered field and the second term the mutual interference between the illumination and scattered fields.

The situation is illustrated in Fig. 2.1 where a monochromatic plane wave incident on a refractive index distribution gives rise to a weak scattered field. Both illumination and scattered field are then collected by the optical system and interfere at the image plane.
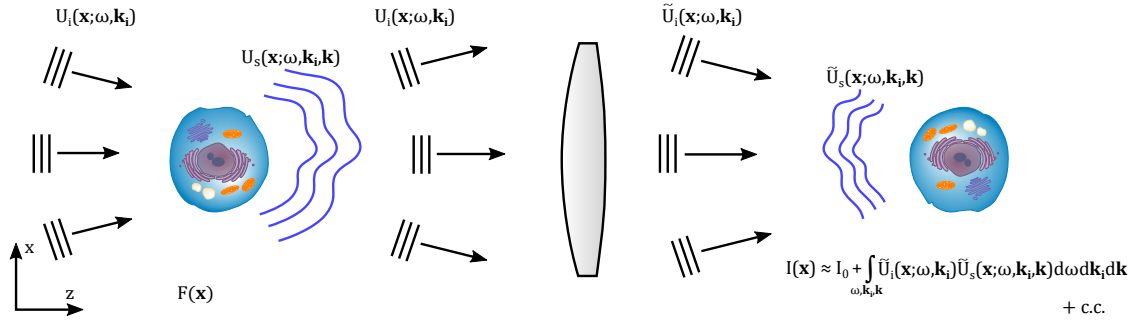

Figure 2.1 – Illustration of image formation process in bright field transmission microscopy.

The product between the scattered and un-scattered field contains all information of the object. Following equation 2.11 and 2.12, we obtain in the object Fourier space

$$U_s(\mathbf{g};\omega,\mathbf{k}) \otimes U_i^*(\mathbf{g};\omega,\mathbf{k}_i) =$$

$$i A(\omega) \frac{F(\mathbf{K};\omega)\delta(\mathbf{g}-\mathbf{k})}{k_z} \otimes_{\mathbf{k}} A^*(\omega)\delta(\mathbf{g}+\mathbf{k}_i) = i S(\omega) \frac{F(\mathbf{K};\omega)}{k_z}\delta(\mathbf{g}-\mathbf{K}), \tag{2.16}$$

where $\mathbf{K} = \mathbf{k} - \mathbf{k}_i$ (Laue equation) and $AA^* = S(\omega)$ the intensity of the light source. This expression is illustrated in Fig. 2.2a by the corresponding Ewald sphere construction taking into account the elastic light scattering. For a given frequency ω, illumination and scattering vector $\mathbf{k}_i$ and $\mathbf{k}$, the scattering potential $F(\mathbf{g};\omega)$ at the spatial frequency $\mathbf{K}$ is interrogated with an amplitude $\frac{S(\omega)}{k_z}$.

Finally the interference term i.e. the cross-spectral density $\Gamma(\mathbf{g})$ is expressed

$$\Gamma(\mathbf{g}) = \int_{\omega,\mathbf{k}_i,\mathbf{k}} i \frac{S(\omega)F(\mathbf{g};\omega)\delta(\mathbf{g}-\mathbf{K})}{k_z} d\mathbf{k}_i d\mathbf{k} d\omega \tag{2.17}$$

where we integrate over the source spectra and the angular spectra (illumination and scattering).

Due to the limited bandwidth of our illumination, we neglect the dispersion of the scattering potential. This results in a linear relationship for the cross-spectral density.

$$\Gamma\left(\mathbf{g}\right) = iF\left(\mathbf{g}\right)H\left(\mathbf{g}\right) \tag{2.18}$$

with the polychromatic coherent transfer function $H\left(\mathbf{g}\right)$,

$$H\left(\mathbf{g}\right) = \int_{\omega,\mathbf{k}_i,\mathbf{k}} \frac{S\left(\omega\right)}{k_z} \delta\left(\mathbf{g} - \mathbf{K}\right) d\mathbf{k}_i d\mathbf{k} d\omega. \tag{2.19}$$

Each combination of illumination and detection modes (frequency (ω) dependent) interrogates a different point of the object's spatial frequency content. The final transfer function is then given by a linear superposition of all contributions.

We obtained this result based on the Helmholtz equation using the first order Born approximation for describing the scattering field as an interaction between the illumination field and a weakly scattering object. The polychromatic illumination has been embedded in a generalized Wiener-Khintchine formalism. The spatial coherence is taken into account by a mutual intensity consideration following the seminal work of N. Streibl[72].

This work on 3D imaging is based on a telecentric configuration containing a Koehler illumination matching all experimental elements of our setup. As a main result of this analysis, the scattering potential $F(\mathbf{g})$ is low pass filtered by the imaging system as described by the Coherent Transfer Function (CTF) $H\left(\mathbf{g}\right)$.

A key assumption we made to derive this linear model (equation 2.18) is the weak scattering approximation, i.e. only single scattering events contribute to the measured signal. This assumption is valid for example when imaging single layer of cells. Imaging thicker samples requires a modified theory taking into account multiple scattering events[6].

The complex ingredients of the theoretical analysis are illustrated in an Ewald sphere representation (Fig. 2.2b). For each wavelength, the Ewald sphere shows the frequency support which corresponds to an axially shifted sphere cap of radius $\bar{n}k_0$ with a lateral extent given by the product of the rescaled wave number k_0 with the detection numerical aperture $\left(g_{\perp max} = \bar{n}k_0 \text{NA}_{det}\right)$ and an axial extent limited to[73] $g_{z,max}\left(g_\perp, \text{NA}_{det}\right) = \bar{n}g_\perp \left(1 - \sqrt{1 - \frac{\text{NA}_{det}^2}{\bar{n}^2}}\right)$. Each of these wavelength-dependent sphere caps are summed up to build the support of the polychromatic system transfer function, where the weights are given according to equation 2.19.

Taking into account the full angular spectrum of the illumination, we integrate over all illumination $\mathbf{k}_i$. The resulting CTF $H\left(\mathbf{g}\right)$ is shown in Fig. 2.2c.
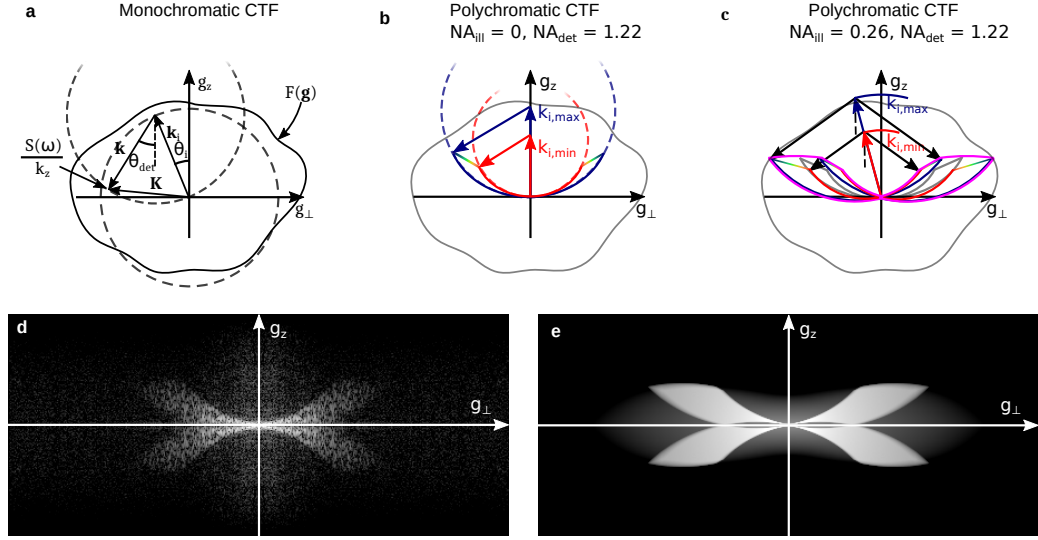
Figure 2.2 – Construction of the polychromatic coherent transfer function. (a) Illustration of elastic light scattering (b) Frequency support of the polychromatic CTF with plane wave illumination, (c) Frequency support of the polychromatic CTF with Koehler illumination, (d) Logarithmic absolute valued 3D-FFT of experimental intensity stack, acquired by translating a sample of fixed hippocampal primary neurons in steps of 200 nm ($\approx 50\ \mu m$ x 50 μm m x 40 μm), showing the system transfer function and its mirrored complex conjugate, (e) Logarithmic absolute valued 3D-FFT of simulated 3D intensity stack based on the proposed model ($\text{NA}_{ill} = 0.26, \text{NA}_{det} = 1.15$).

In complement to the theoretical analysis and the Ewald sphere representation, we calculate (Fig. 2.2d) the experimental 3D-fast Fourier Transform (FFT) of a large intensity stack, containing the transfer function $H(\mathbf{g})$ and its mirrored complex conjugate. Fig. 2.2e shows the simulated 3D-FFT of an equally large intensity stack, based on the experimental source spectrum, the illumination and detection NA.

2.2 Retrieving the complex 3D cross-spectral density

To recover the 3D cross-spectral density and its corresponding phase, only a 3D bright field image stack is required. The different planes can be acquired sequentially by a z-scan or in a multi-plane configuration (see Fig. 2.11), which provides camera rate 3D phase tomographic measurements. For each plane z_p we detect the interference of the incident field with the scattered field. Using equations 2.15 and 2.17, we write

$$I\left(\mathbf{x}_p\right) = I_{DC} + \Gamma\left(\mathbf{x}_p\right) + \Gamma^*\left(\mathbf{x}_p\right), \tag{2.20}$$

where we used the short-hand notation $\mathbf{x}_p = \left(x, y, z_p\right)$.

Taking the 3D Fourier transform of this equation, we obtain

$$I(\mathbf{g}) = I_{DC}\delta(\mathbf{g}) + \Gamma(\mathbf{g}) + \Gamma^*(-\mathbf{g}).$$

(2.21)

The intensity spectrum can be decomposed into a DC-part $I_{DC}\delta(\mathbf{g})$ and an AC part, composed of two symmetric and conjugate cross-spectral densities.

Filtering the intensity $I(\mathbf{g})$

$$\Gamma_+(\mathbf{g}) = I(\mathbf{g})K(g_z)$$

(2.22)

with a cutoff filter $K(g_z)$

$$K(g_z) = \begin{cases} 1 & if\, g_z > 0 \\ 0 & else \end{cases}$$

(2.23)

suppresses the conjugated cross-spectral density $\Gamma^*(-\mathbf{g})$.

This filtering condition entails the analyticity of the cross-spectral density along the axial direction i.e. the real and imaginary part of $\Gamma(\mathbf{x})$ form a Hilbert transform pair (Titchmarsh theorem)[74]. Therefore, the amplitude and the phase are simply two alternative representations of the filtered scattering potential, where the amplitude appears as the imaginary part of transfer function $H(\mathbf{g})$ and the phase as the real part of $H(\mathbf{g})$ (see equation 2.18). In other words, a point scatterer appears in intensity as an axial phase shift with no contrast in focus while the phase appears as a Gaussian with maximum contrast (see Fig. 2.4a).

2.2.1 Quantitative phase derivation

From a general point-of-view, the quantitative phase can be expressed as

$$\varphi(\mathbf{x}) = angle\left(\frac{U_s + U_i}{U_i}\right)$$

(2.24)

where U_i is the reference field that would be measured without any sample and $U_s + U_i$ is the total field, including a sample. Hence, φ represents the phase delay due to the sample.

In order to link this expression to the cross-spectral density, we rearrange equation 2.24

$$\varphi(\mathbf{x}) = angle\left(1 + \alpha\frac{U_s}{U_i}\right) = \tan^{-1}\left(\frac{\alpha\left|\frac{U_s}{U_i}\right|\sin(\Delta\varphi)}{1 + \alpha\left|\frac{U_s}{U_i}\right|\cos(\Delta\varphi)}\right),$$

(2.25)

which corresponds to the quantitative phase[75], with $\Delta\varphi = \varphi_s - \varphi_i$. It is important to note that equation 2.24 applies to the object space. Since U_s and U_i have a different spatial frequency spectra, both fields will be filtered differently while propagating from the sample plane to the detector[76]. In order to account for this effect, we introduce a real positive calibration factor α which is experimentally determined using known and well-characterized technical samples (see 2.4).

Expanding the fraction by $\frac{|U_i|^2}{|U_i|^2}$, equation 2.25 can be further simplified as,

$$\varphi(\mathbf{x}) = \tan^{-1}\left(\frac{\alpha\,|U_i|\,|U_s|\sin\left(\Delta\varphi\right)}{|U_i|^2 + \alpha\,|U_i|\,|U_s|\cos\left(\Delta\varphi\right)}\right). \tag{2.26}$$

Noting that $|U_i|^2$ is the mean intensity I_0, and $|U_i|\,|U_s|\sin\left(\Delta\varphi\right)$ and $|U_i|\,|U_s|\cos\left(\Delta\varphi\right)$ are equivalent to the imaginary and real part of $\Gamma_+(\mathbf{x})$ respectively, we obtain a general equation linking the quantitative phase to the cross-spectral density as,

$$\varphi(\mathbf{x}) = \tan^{-1}\left(\frac{\alpha\Im\left(\Gamma_+(\mathbf{x})\right)}{I_0 + \alpha\Re\left(\Gamma_+(\mathbf{x})\right)}\right). \tag{2.27}$$

2.2.2 Quantitative phase algorithm

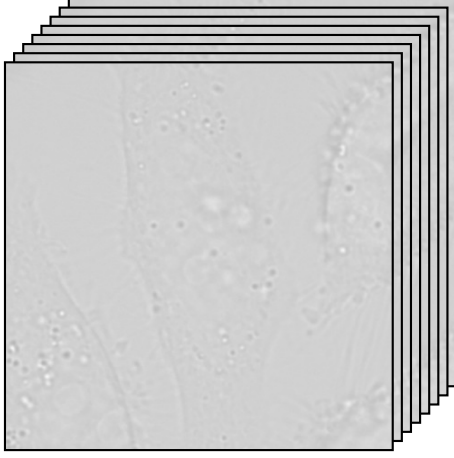The phase retrieval algorithm (see Fig. 2.3) can be summarized as follows

1. Data acquisition.

2. Signal mirroring along the axial direction to avoid boundary effects and 3D Fourier transform of the 3D stack.

3. Application of mask K for removing all $g_z \leq 0$ contributions of the Fourier spectrum and Fourier denoising using a CTF-shaped mask.

4. Inverse Fourier transform for retrieving the cross spectral density in real space. Reconstruct the image field and calculate the 3D quantitative phase.

2.3 Simulation and validation

2.3.1 Calculating the partially coherent system transfer function

For the illumination k-spectrum (limited by NA_{ill}), the corresponding Ewald sphere cap (limited by NA_{det}) is weighted according to the polychromatic spectrum of the source and projected on the reciprocal Fourier space (according to the specified field of view). These k-supports (Ewald sphere caps) are added to form the full polychromatic $\mathbf{k}$-support. The calculated 2D CTF (basically a convolution of the illumination aperture and the detection

STEP 1: Data aquisition and multi-plane coregistration
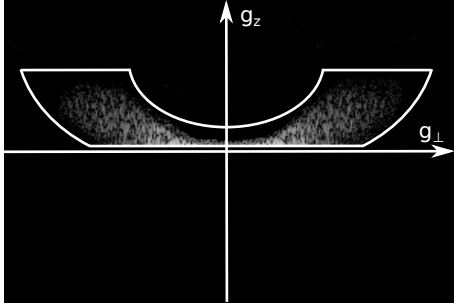
STEP 2: Signal mirroring and 3D FFT

STEP 4: i-FFT and phase calculation
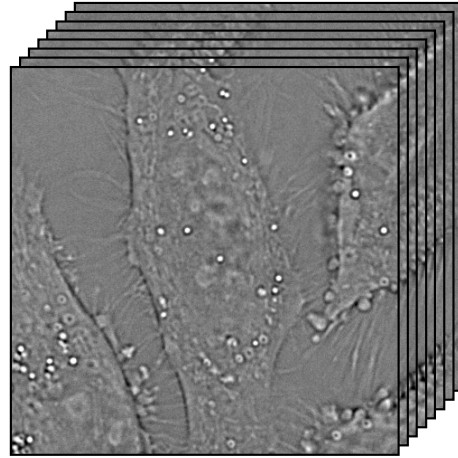
STEP 3: Fourier filtering and denoising

Figure 2.3 – Workflow of the phase retrieval algorithm. In STEP 1 and 4, 8-plane image stacks of fixed HeLa Cell are shown. In STEP 2 and 3, the data is displayed using a logarithmic scale.

aperture) is then mapped onto the 3D frequency support, taking into account the symmetry properties of the CTF (weighing according to equation 2.16), as shown in Fig. 2.2d.

2.3.2 3D image formation simulation

We define a point scatterer in real space by a Dirac function. The corresponding scattering potential is calculated and convolved with the previously established system transfer function $H(\mathbf{g})$ resulting in the complex 3D cross-spectral density $\Gamma(\mathbf{x})$. The 3D image intensity is given by the absolute squared interference of the incident field with the scattered field (equation 2.18). All calculations have been performed using Matlab (R2016a).

2.3.3 Experiment vs simulation

We imaged 200 nm polystyrene beads sparsely distributed in agarose. Due to their size ($\leq \lambda/2$), we used the beads as an approximation of a point scatterer.

Fig 2.4a displays an axial cross-section of the computed and experimental 3D image (averaged over 15 individual measurements), showing an almost perfect match between experimental and simulated images. Their corresponding calculated phase underlines the validity of our model and is further demonstrated in lateral and axial line plots (Fig. 2.4b). Fig. 2.4c shows the color-coded maximal z-projection of the full experimental recovered phase stack. The orthogonal slice 1-2 shows the optical sectioning for our 3D phase imaging.
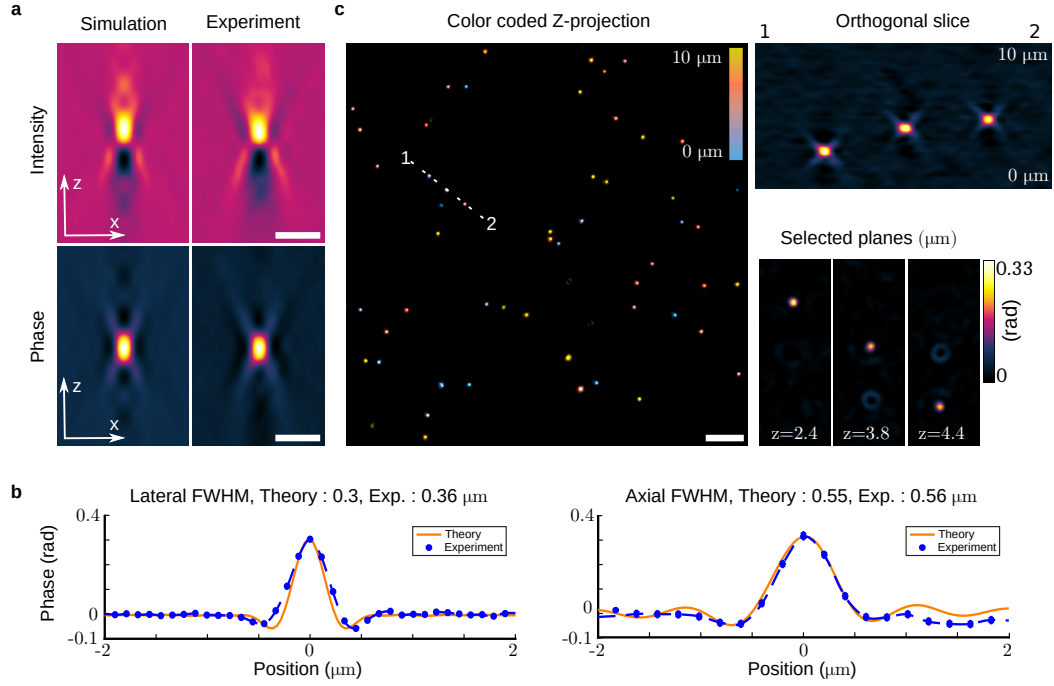

Figure 2.4 – Experiments and simulations with polystyrene beads (a) 3D axial slice of computed and experimental (average over 15 measurements) intensity and phase of 200 nm polystyrene beads. Scale bar 1 μm, (b) Comparison of the theoretical and experimental phase profile showing almost perfect agreement, (c) Color coded maximum z-projection of the phase of sparsely distributed beads. The orthogonal slice 1-2 demonstrates the sectioning capability of the method. Scale bar 5 μm.

2.4 Quantitative phase calibration using technical sample

As discussed in chapter 2.2.1, a calibration step is required to accommodate for the unequal transmission of the reference and the scattered fields.

In order to calibrate our analysis, we imaged a staircase-like nanometric structure made by repetitive chemical etching of a glass substrate (borosilicate, see Section 8.5). A total of 50 planes with an inter-plane distance of 200 nm were used to accurately extract the calibration factor. The in-focus bright field image and its corresponding calibrated phase are shown in Fig. 2.5a respectively Fig. 2.5b. Fig. 2.5c shows the Atomic Force Microscopy (AFM) measurement
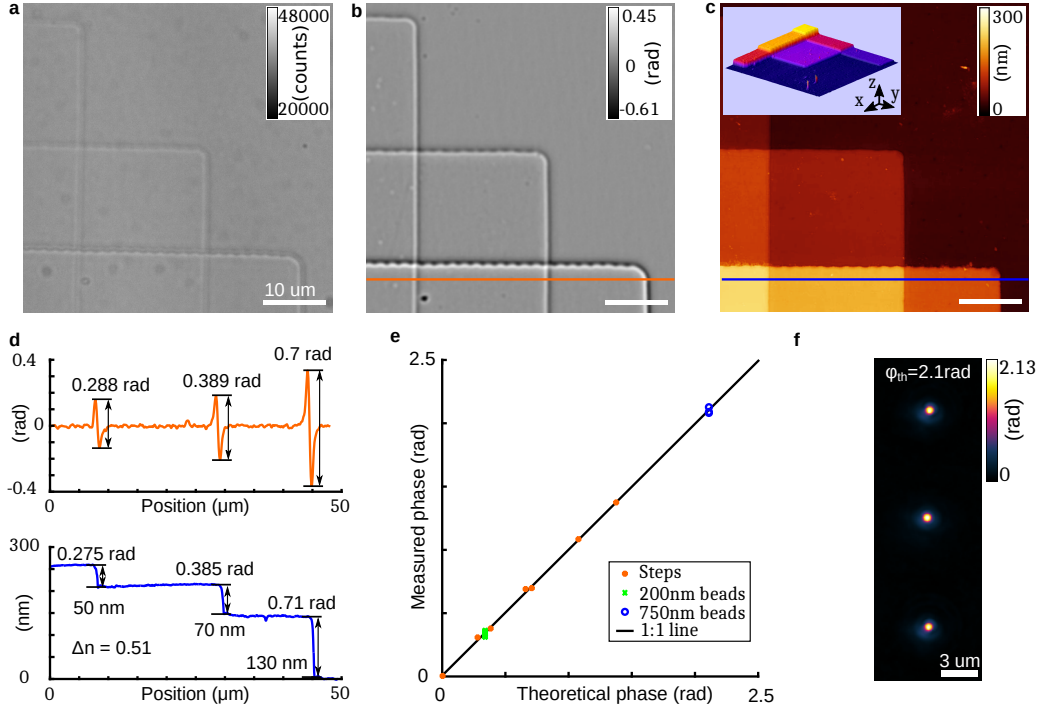
Figure 2.5 – Quantitative phase imaging of technical sample. (a) In-focus bright field image of nanometric step like borosilicate structure, (b) Corresponding quantitative phase after processing of the intensity stack, (c) AFM measurement (insert : 3D surface plot using ImageJ[77]), (d) Line plots of selected lines indicated in (b) and (c), quantitative phase (orange), AFM measurement (blue), (e) Measured phase vs. theoretical phase for step heights (orange dots), 200 nm polystyrene beads (green cross) and 750 polystyrene beads (blue circle). The 1:1 line is also plotted to provide a visual reference, (f) Max. phase projection of 750 nm polystyrene beads.

of the staircase structure used to calibrate the phase measurements. Due to the limited spatial coherence (same illumination aperture used for all imaging) which acts as a high-pass filter, only the edges can be quantitatively resolved in the phase image.

The AFM measurements allow to compute the theoretical phase signal as $\varphi = k_0 \Delta n h$, where $k_0 = \frac{2\pi}{\lambda} = 10.8 \mu m^{-1}$, $\Delta n = n_{glass} - n_{air} = 1.51 - 1$ in air and h is the relative step height. The calibration factor is then estimated by solving equation 2.27 for α and using the expected theoretical phase and the measured imaginary and real parts of the cross-spectral density, and the average intensity. For our setup, we estimated $\alpha = 3.15$. The Fig. 2.5d shows calibrated phase and AFM line plots demonstrating how the phase signal varies proportionally to the step height. The Fig. 2.5e shows (orange dots) all the recovered phase jumps of the 6 steps (Fig. 2.5c).

In order to validate the calibration, we imaged 200 nm and 750 nm polystyrene beads ($n_{beads} = 1.59$) embedded in agarose $(n_{agar} = 1.33)$, for a total of 50 planes with an inter-plane distance of 200 nm (shown in Fig. 2.4). The obtained phases are in total agreement with the theory. The 200 nm beads being smaller than the system point-spread function, the theoretical phase has

to be adjusted by averaging the optical path length over the beads diameter which provides an estimated correction factor of ≈ 0.6, leading to a theoretical phase shift of $0.34[rad]$. We measured an average phase of $0.33 \pm 0.014[rad]$ (average over 15 beads, depicted as a green crosses in Fig. 2.5e). The 750 nm beads being larger than the phase point-spread function, we only have to consider the maximal phase shift. Fig. 2.5f shows the maximal phase projection of 750 nm beads, providing another independent confirmation of the ability of the method to achieve quantitative phase imaging (theoretical phase of $2.106[rad]$ and average measured phase of $2.08[rad]$).

2.5 Symmetry of the coherent transfer function and coherence

As it was shown in section 2.2, the cross-spectral density $\Gamma(\mathbf{g})$ is the phase delayed object function $F(\mathbf{g})$ weighted by the partially coherent transfer function $H(\mathbf{g})$, acting as the transmission amplitude of all spatial frequencies. The three-dimensional shape of $H(\mathbf{g})$ is essentially determined by the illumination and detection numerical aperture NA_{ill} and NA_{det}.
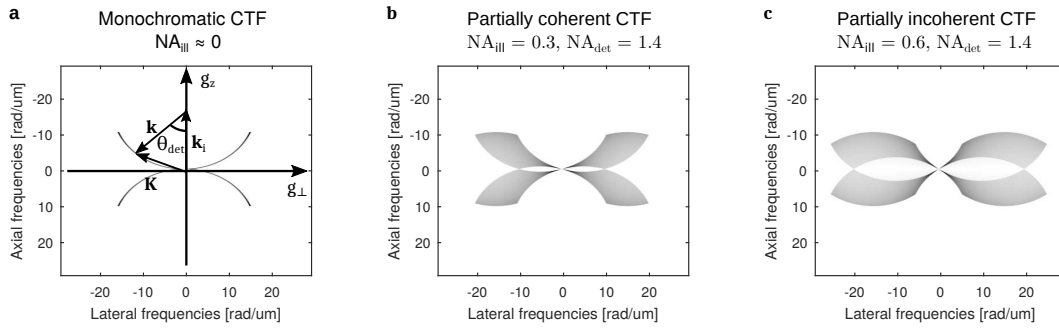

Figure 2.6 – Partially coherent transfer function and Ewald sphere (a) Monochromatic CTF with $\lambda = 580nm$, $NA_{ill} \approx 0$ and $NA_{det} = 1.4$. (b) Partially coherent CTF with $NA_{ill} = 0.3$. (c) Partially incoherent CTF with $NA_{ill} = 0.6$.

In the case of partially coherent illumination ($0 < NA_{ill} < NA_{det}$), the transfer function, and in consequence the cross-spectral density, is almost completely located in the upper half of the frequency space ($g_z > 0$), whereas its complex conjugate extends in the negative frequency space ($g_z < 0$). Both transfer functions overlap in a common region near the low axial frequencies. The Fourier transform of the intensity in this overlapping area is given by

$$I(\mathbf{g}) = I_0 \delta(\mathbf{g}) + \Gamma(\mathbf{g}) + \Gamma^*(-\mathbf{g}) \tag{2.28}$$

where $\Gamma^*(-\mathbf{g}) = \left(iF(-\mathbf{g}) H(-\mathbf{g})\right)^*$. This is illustrated in Fig. 2.6. Fig. 2.6a shows a slice of a highly coherent monochromatic CTF ($\sigma = \frac{NA_{ill}}{NA_{det}} \approx 0$) together with its complex conjugate. In this case, only the zero frequency is suppressed by the overlap. In other word, in a bright-field configuration, it is not possible to recover the average phase shift of the scattered field. Increasing the illumination NA to 0.3 as shown in Fig. 2.6b, we observe a thin frequency band

near the low axial frequencies ($\pm 2 rad/\mu m$ in this case) where the amplitude of the transfer function is affected. For Fig. 2.6c, we have $NA_{ill} = 0.6$ ($\sigma = 0.42$). The overlap has the shape of an incoherent CTF with a NA equal to NA_{ill}. A further increase of NA_{ill} expands the lateral and axial support of the CTF as well as of the overlap. For the incoherent case ($NA_{ill} = NA_{det}$; $\sigma = 1$), the overlap area dominates the CTF, which has as a consequence that no phase information can be recovered.

We now evaluate the transfer function in the overlap region. Assuming $H(\mathbf{g})$ being a real function (i.e. the system has no phase aberration, $H(\mathbf{g}) = H^*(\mathbf{g})$) and $F(\mathbf{g})$ is a Hermitian function (i.e. there is no absorption; $F(\mathbf{x})$ is real; $F(\mathbf{g}) = F^*(-\mathbf{g})$). We decompose $F(\mathbf{g})$ in its real and imaginary contribution $F_r(\mathbf{g}) + iF_i(\mathbf{g})$ and obtain for the intensity (ignoring the DC-contribution $I_0\delta(\mathbf{g})$)

$$\Gamma(\mathbf{g}) + \Gamma^*(-\mathbf{g}) = (iF_r(\mathbf{g})H(\mathbf{g}) - F_i(\mathbf{g})H(\mathbf{g})) - (iF_r(-\mathbf{g})H(-\mathbf{g}) + F_i(-\mathbf{g})H(-\mathbf{g})). \quad (2.29)$$

Using the fact that $F(\mathbf{g})$ is Hermitian $(F(\mathbf{g}) = F^*(-\mathbf{g}))$, we obtain

$$\Gamma(\mathbf{g}) + \Gamma^*(-\mathbf{g}) = [H(\mathbf{g}) - H(-\mathbf{g})][iF_r(\mathbf{g}) - F_i(\mathbf{g})] = iF(\mathbf{g})[H(\mathbf{g}) - H(-\mathbf{g})] \quad (2.30)$$

We therefore see that the cross-spectral density and its complex conjugate in the considered overlap area, can be interpreted as an object function $F(\mathbf{g})$ modulated by a new effective transfer function

$$H_{\text{eff}}(\mathbf{g}) = H(\mathbf{g}) - H(-\mathbf{g}) \quad (2.31)$$

The amplitude of $H_{\text{eff}}(\mathbf{g})$ is linked to the symmetry of $H(\mathbf{g})$. We know from the equation 2.19 and from H. Gross et al[5] that the axial symmetry of $H(\mathbf{g})$ is directly related to the degree of spatial coherence of the field (i.e. $\sigma = NA_{ill}/NA_{det}$). For $\sigma = 0$ (coherent case), there is no overlap. For $\sigma = 1$ (incoherent), $H(\mathbf{g})$ becomes completely symmetric which implies that $H(\mathbf{g}) - H(-\mathbf{g}) = 0$ over the whole frequency support of $H(\mathbf{g})$. This is consistent with the fact that no phase information can be extracted from an incoherent system. In the case of partial coherence, the overlap transfer function $H_{\text{eff}}(\mathbf{g})$ is strongly attenuated in the corresponding spatial frequencies. However the object $F(\mathbf{g})$ is fully preserved and can in principle be recovered via a deconvolution operation.

Due to its axial symmetry, we note that the complex cross-spectral density can be retrieved by measuring the 3D intensity distribution and filtering with the mask

$$M(\mathbf{g}) = \begin{cases} 1 & \text{if } g_z > 0 \\ 0 & \text{elsewhere} \end{cases} \quad (2.32)$$

This mask is nothing else than an axial Hilbert transform (i.e. the analytical axial continuation of the signal). Applying this mask to the Fourier transformed of the 3D intensity allows to

recover the complex cross-spectral density $\Gamma_+(\mathbf{g}) = M(\mathbf{g}) I(\mathbf{g}) = iF(\mathbf{g}) H_{eff}(\mathbf{g})$, with

$$
H_{\text{eff}}(\mathbf{g}) = \begin{cases} H(\mathbf{g}) & \text{for } \mathbf{g} \text{ outside of the overlap} \\ H(\mathbf{g}) - H(-\mathbf{g}) & \text{for } \mathbf{g} \text{ inside of the overlap} \end{cases} \tag{2.33}
$$

There is no general analytical expression for $H_{texteff}(\mathbf{g})$ possible. However, for a given spectral bandwidth, illumination and detection NA, it can be computed and used to deconvolve the cross-spectral density, taking into account the partial coherence and allowing to retrieve $F(\mathbf{g}) = \frac{\Gamma_+(\mathbf{g})}{H_{\text{eff}}(\mathbf{g})}$ over the whole frequency support of $H(\mathbf{g})$.

2.5.1 Link with Transport of Intensity Equation

To demonstrate the close relation to the Transport-of-Intensity Equation and our Helmholtz based approach, we proceed in two steps. First, we show that the intensity filtering operation (i.e. applying $M(\mathbf{g})$ on $I(\mathbf{g})$) is identical to computing the discrete axial intensity derivative. Second, we show that the partially coherent transfer function $H_{\text{eff}}(\mathbf{g})$ projected in 2D is well approximated by the Fourier transform of the Laplacian operator ∇^2 for low spatial frequencies.

We remind the definition of the Transport of Intensity Equation[78]

$$
\frac{k_0}{I_0} \frac{\partial I(x,y,z)}{\partial z} = \nabla^2 \varphi(x,y) \tag{2.34}
$$

where we made the assumption that the in-focus intensity is uniform, i.e. $\nabla I \nabla \varphi = I_0 \nabla^2 \varphi$.

We define an arbitrary intensity out (+,-) and in the focal plane as

$$
I[z] = \begin{bmatrix} I_+ \\ I_0 \\ I_- \end{bmatrix} = \begin{bmatrix} I_0 + \Delta I \\ I_0 \\ I_0 - \Delta I \end{bmatrix}, \text{ with } I_0 = \frac{I_+ + I_-}{2}, \ \Delta I = \frac{I_+ - I_-}{2} \text{ and } \Delta I \ll I_0 \tag{2.35}
$$

$I[z]$ represents the axial intensity in 3 planes of a 2D pure phase object positioned in the intermediate object plane. The average intensity is I_0. The Fourier transform matrix W and the filter matrix M can be expressed as

$$
W = \begin{pmatrix} 1 & e^{\frac{2\pi i}{3}} & e^{\frac{4\pi i}{3}} \\ 1 & 1 & 1 \\ 1 & e^{\frac{-2\pi i}{3}} & e^{\frac{-4\pi i}{3}} \end{pmatrix}; M = \begin{pmatrix} 1 & 0 & 0 \\ 0 & 1 & 0 \\ 0 & 0 & 0 \end{pmatrix} \tag{2.36}
$$

The cross-spectral density $\Gamma[z]$ writes as

$$\Gamma[z] = W^{-1}MWI_z \tag{2.37}$$

where we apply W (forward Fourier transform), the mask M, and W^{-1} (inverse Fourier transform).

The complex field associated to the focal plane $I[0]$ is given as

$$\Gamma[0] = I_0 + i\frac{1}{3}\sin\left(\frac{\pi}{3}\right)\Delta I \tag{2.38}$$

We have shown (2.27) that the quantitative phase (phase difference between the field $U_s + U_i$ and the field U_i) can be expressed as a function of the cross-spectral density as

$$\varphi(\mathbf{x}) = \tan^{-1}\left(\frac{\alpha\Im(\Gamma_+(\mathbf{x}))}{I_0 + \alpha\Re(\Gamma_+(\mathbf{x}))}\right) \tag{2.39}$$

where α is a real positive experimental factor required to model the transmission from the sample plane to the detector plane. Under the weak scattering approximation $I_0 \gg |\Gamma_+(\mathbf{g})|$, the quantitative phase can be rewritten as

$$\varphi(\mathbf{x}) \approx \alpha\frac{\Im(\Gamma_+(\mathbf{x}))}{I_0} = \alpha\frac{F(\mathbf{x})\otimes\Im\left(H_{eff}(\mathbf{x})\right)}{I_0} \tag{2.40}$$

where $\otimes$ denotes a convolution.

Using equation 2.39 , we express the quantitative phase associated to $\Gamma[0]$ (equation 2.38)

$$\varphi[0] = \tan^{-1}\left(\alpha\frac{\sin\left(\frac{\pi}{3}\right)\Delta I}{3I_0}\right) \approx \beta\frac{\Delta I}{I_0} \tag{2.41}$$

where $\beta = \alpha\sin(\pi/3)/3$ is a setup dependent parameter that needs to be estimated via a calibration with a known phase object. The recovered phase is directly proportional (under the weak scattering approximation) to the axial intensity derivative normalized by the average intensity. The quantitative phase $\varphi[0]$ (equation 2.41) is therefore identical to the left-hand side of the TIE (equation 2.34) up to a factor β that arise from the processing and is in all cases compensated by the experimental calibration of α.

The transfer function H_{eff} (equation 2.19 and 2.33) is equivalent to the Laplacian of the TIE (equation 2.36). We also note a difference in notation where the phase of the TIE φ (equation 2.34) represents the deconvolved quantitative phase of our model, that is the object $F(x)$. The
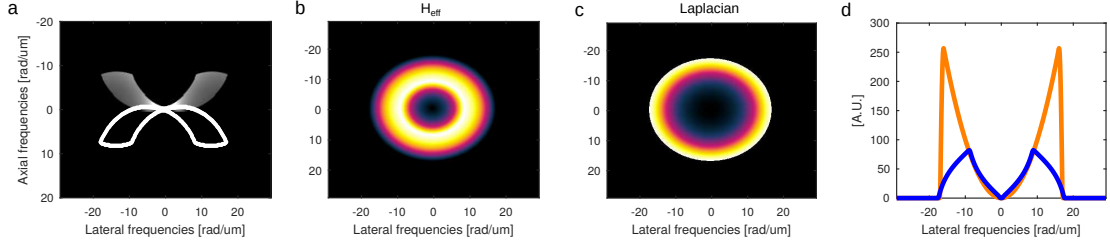
Figure 2.7 – Helmholtz and Paraxial transfer functions. (a) Slice of Helmholtz based transfer function and its complex conjugated (white line), $\lambda_{central} = 580nm, \mathrm{NA}_{ill} = 0.3, \mathrm{NA}_{det} = 1.42$. (b) 2D projection of $H_{eff}(\mathbf{g})$. (c) Paraxial based 2D transfer function H_{TIE} (Laplacian). (d) Line profiles of (b, Helmholtz, blue) and (c,Laplacian, orange) showing how the Paraxial approximation matches the Helmholtz based model for the low frequencies.

situation is summarized in Table 2.1.

Table 2.1 – Comparison to the phase retrieval from 3D intensity data using either TIE or our Helmholtz based model

	TIE	Helmholtz
Cross-spectral density $\Gamma(\mathbf{x})$	$I_0 + i\Delta I \sin(\pi/3)/3$	$F^{-1}(I(\mathbf{g})M(\mathbf{g}))$
Coherent transfer function $H(\mathbf{g})$	∇^2	$\int_{\omega,\mathbf{k}_i,\mathbf{k}} \frac{S(\omega)}{k_z}\delta(\mathbf{g}-\mathbf{K})\,d\mathbf{k}d\mathbf{k}_i d\omega$
Quantitative phase $\varphi(\mathbf{x})$	$\Delta I/I_0$	$\alpha\Im(\Gamma_+(\mathbf{x}))/I_0$
Scattering potential $F(\mathbf{x})$	$\nabla^{-2}\frac{k_0}{I_0}\frac{\Delta I}{\Delta z}$	$F^{-1}\left(H^{-1}(\mathbf{g})\,\alpha\Im(\Gamma_+(\mathbf{x}))/I_0\right)$

However, the Helmholtz based approach is more general as it accepts an arbitrary number of planes, is not restricted to 2D phase objects and does not involve the paraxial approximation.

Since there is no analytical expression for the partially coherent effective transfer function $H_{\mathrm{eff}}(\mathbf{g})$, we rely on in-silico computation. The calculation requires a high-resolution 3D grid representing the Fourier space $\mathbf{g}$. Then for each wavelength, illumination and detection angle $(\omega, \mathbf{k}_i, \mathbf{k})$, the value $\frac{S(\omega)}{k_z}$ is added at the scattering vector $\mathbf{K} = \mathbf{k} - \mathbf{k}_i$. Fig. 2.8a shows an axial slice of a 3D transfer function computed according to the equation 2.19. The white line indicates its complex conjugate. Fig. 2.8b shows the 2D projection of (a) (sum along g_z) which is required to be able to compare the model with the paraxial approximation where a solution only exists for 2D phase objects. Fig. 2.8c shows the TIE transfer function (Laplacian $H_{\mathrm{TIE}}(\mathbf{g}) = g_x^2 + g_y^2$). Fig. 2.8d shows the line profiles of the two model, showing a good agreement for the low frequencies (where the paraxial approximation is valid) and a clear discrepancy at high frequencies. We therefore expect from our model to amplify the low-frequencies and but also to preserve the high-frequencies that will be attenuated by the inverted Laplacian.

2.5.2 Experimental comparison of TIE vs Helmholtz

In order to demonstrate the usefulness of our model, we deconvolve experimental data of an ion-beam etched borosilicate wafer ($n = 1.51$, $\Delta n = 0.51$ in air). This technical sample consists in two 10 μm wide perpendicular lines with consecutive etching depth of 15 and 30 nm, forming a well with a width of 45nm in the center. The sample was characterized with an atomic force microscopy (AFM) measurement (see Figure 2.8a). The same sample was imaged on a bright-field microscope with a Kohler illumination ($NA_{ill} \approx 0.3$, $\lambda_{central} = 580$ nm), a 60x 1.42NA oil objective (Olympus Apo-plan N), an xyz-translation stage (piezoLEGS, Nanos Instruments GmbH) and a Hamamatsu Orca flash V4.2 (projected pixel size of 108nm).
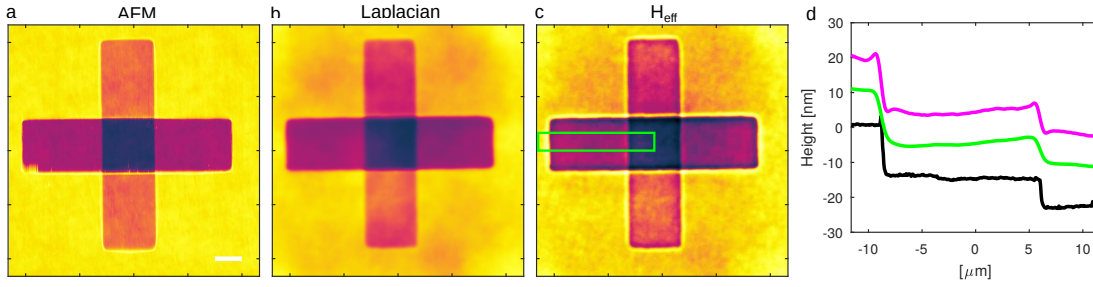

Figure 2.8 – Phase calibration of etched borosilicate with two 10 μm wide perpendicular lines with consecutive etching depth of 15 and 30 nm (a) AFM measurement of. (b) TIE phase image. (c) Deconvolved phase using the proposed model. (d) Averaged line profile (indicated by the green rectangle in (c)) of AFM (black), Laplacian (green) and H_{eff} (magenta). Scale bar, 5 μm.

First a z-stack of 50 bright-field defocused planes axially spaced by 200 nm is acquired. The cross-spectral density and phase are then retrieved following equation 2.34 ($\alpha = 3.15$, where α was estimated using the AFM measurement). The in-focus plane (plane with highest contrast) is then deconvolved (Wiener filtering with a regularization factor of 5 10^{-4}) by using the Laplacian as a transfer function (TIE, Figure 2.8b) and the 2D effective transfer function $H_{eff}(g_x, g_y)$ (Figure 2.8c). Figure 2.8d shows the averaged line profile (indicated by the green rectangle in Figure 2.8c) of the AFM scan (black curve), Laplacian (green curve) and H_{eff} (magenta curve) with a 10 and 20 nm offset to improve visibility. We clearly see how the inverse Laplacian operation strongly attenuates the high-frequencies, resulting in a smooth height transition. On the other hand, the proposed transfer function yields a sharper transition while also retrieving the low frequencies. We also notice that our model produces Gibbs oscillations, which is the typical step response to a low-pass filter. The only way to reduce these oscillations is to apodize the edges of the transfer function, attenuating high-frequencies information.

The Laplacian and the effective transfer function have been calibrated using the AFM data. The calibration allows to extract quantitative optical path difference (OPD) from the intensity measurement. For the technical sample, the refractive index is constant, allowing to assess the sample height. As shown, both method are in a good agreement with the AFM ground truth. The obtained phase precision is ~ 2 nm (standard deviation of phase) and an accuracy of ~ 4 nm (average error between AFM and H_{eff} phase).

In addition to the solid-state technical sample, we also imaged fixed cos-7 cells to compare our model with the standard TIE reconstruction. Figure 2.9a shows the raw quantitative phase retrieved by measuring the 3D intensity, applying the mask $M(\mathbf{g})$, taking its imaginary part and multiplying it by $\frac{\alpha=3.15}{I_0}$.
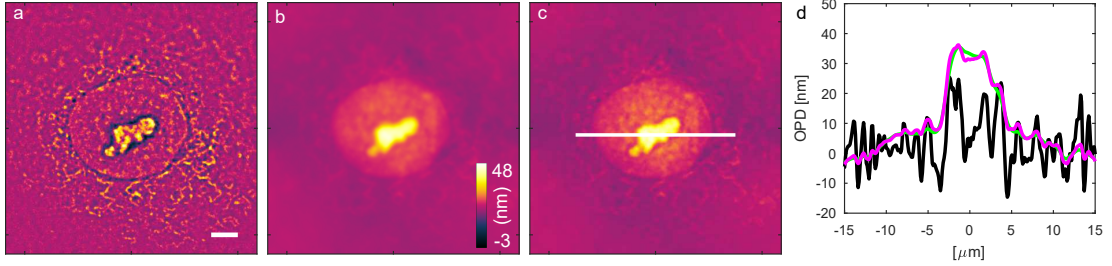

Figure 2.9 – Phase reconstruction. (a) Phase image of fixed cos-7 cell. (b) 2D deconvolution using the inverted Laplacian. (c) 2D deconvolution using the proposed model $H_{\text{eff}}(\mathbf{g})$. (d) Line profiles of (a), (b) and (c) indicated by white line in (c). Scale bar: 5 μm.

Figure 2.9b shows the results of the deconvolution of the Figure 2.9a using the Laplacian, as performed in TIE. Figure 2.9c shows the results of the same deconvolution operation but using the 2D projection of the effective transfer function $H_{\text{eff}}(\mathbf{g})$. Figure 2.9d shows the line profiles of Figure 2.9a, b and c, highlighting the fact that our model intrinsically enhances the low frequencies in the image (envelope of the cell) but also preserves the high-frequencies. The paraxial model (Laplacian), on the other hand, completely removes the high-frequency contribution, and preserves only the phase envelope.

2.5.3 Pupil modulation of coherent transfer function

To demonstrate the viability of the model, we modulated the phase in the illumination pupil by various filters (various NA, ring mask, half-pupil). We imaged a fixed neuron[79], as a 3D weakly scattering source, while simultaneously imaging the back focal plane of the objective.

For each illumination filter, we imaged a bright field stack (field of view: 80 μm, 100 planes spaced by 400 nm) of a fixed neuron sample. We then computed the expected effective transfer function H_{eff} as a function of the experimental conditions. Figure 2.10a shows the axial slice of the computed transfer function for a low illumination NA of 0.05, a detection NA of 1.4 and a central wavelength of 580 nm. Figure 2.10b shows the experimental axial slice of the Fourier transform of the weakly scattering media under similar conditions. The image of the back focal plane of the objective is shown in the inset. We repeated the experiment for two different ring illuminations (Figure 2.10c and d, ring radius of 0.08; Figure 2.10e and f, ring radius of 0.3). We observe an excellent agreement between the calculated and the experimental results. We see that for all conditions, the experimental transfer function vanishes for spatial frequencies larger than $11 \, rad/um$. This can be attributed to the apodization caused by the edges of the illumination and detection path. We also compare the theoretical and experimental effective transfer function of a knife-edged ring illumination in Figure 2.10g and f. The knife-edge was realized by adding an appropriate mask in the image of the back-focal plane of the objective,
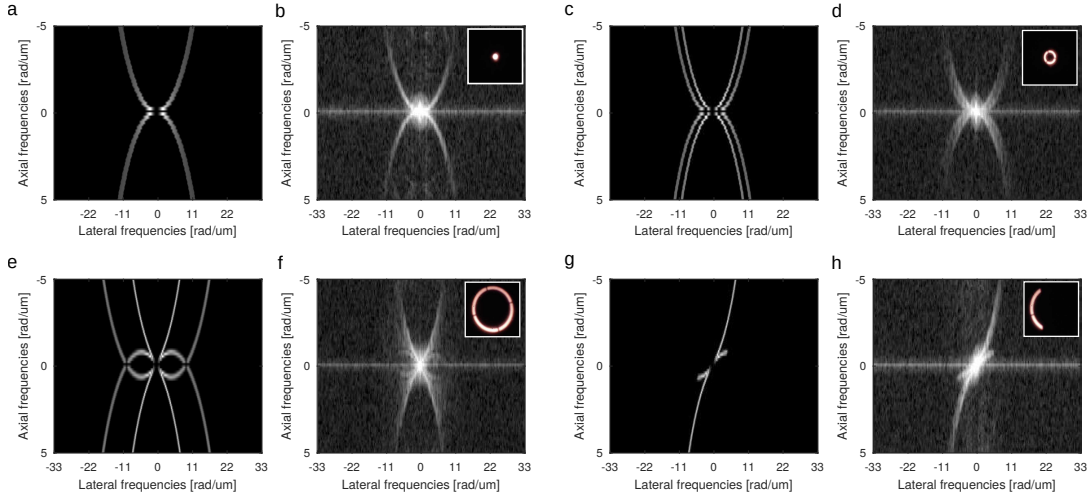
Figure 2.10 – CTF modulation via pupil manipulation. (a) Axial slice of the theoretical H_{eff} for an illumination NA of 0.05 (b) Axial slice of the log of absolute value of 3D Fourier transform of the bright-field image (Inset: Experimental image of the objective back focal plane) (c-d) Ring illumination; Ring radius of 0.08. (e-f) Ring radius of 0.3; (g-h) Ring illumination and knife-edge.

blocking both half of the illumination U_i and half of the scattered field U_s. These results show that our model allows to describe the partially coherent transfer function beyond the paraxial approximation.

2.6 PRISM multi-plane platform

In order to perform fast 3D image acquisition, we conceived a multi-plane platform (MP) based on a novel image splitter. As shown in Fig. 2.11, a customized image splitting prism in the detection arm of the microscope directs the light into 8 distinct images (see Table A.1 and Fig. A.2,A.1). The image splitter, placed in the convergent beam path, provides high inter-plane image stability for recording a sample volume of about 50 μm x 50 μm x 2.5μm. The MP platform allows diffraction limited multiplexed image acquisition of 8 planes with no moving parts (optical design provided in Section A.2, Fig. A.3-A.9). The dominant speed limitation is given by the camera frame-rate (up to 200 Hz in this work).

Due to the common path configuration and fast 3D (8 plane) image acquisition, excellent phase stability is achieved. Our high-NA water immersion objective provides a lateral resolution of 380 nm and an axial resolution of 560 nm for phase imaging (NA$_{det}$ = 1.2, see Section 2.3, Fig. 2.4). We assessed the influence of the 3D intensity sampling on the phase retrieval in detail. As the prism allows fast imaging of 8 planes with an inter-plane distance of 350 nm, we have a trade-off on sampling in Fourier space. The limited axial sampling translates in an additional lateral and axial high-pass filtering of the phase. We have chosen this compromise for the benefit of 3D depth-resolved phase imaging of subcellular structures at 200 Hz.
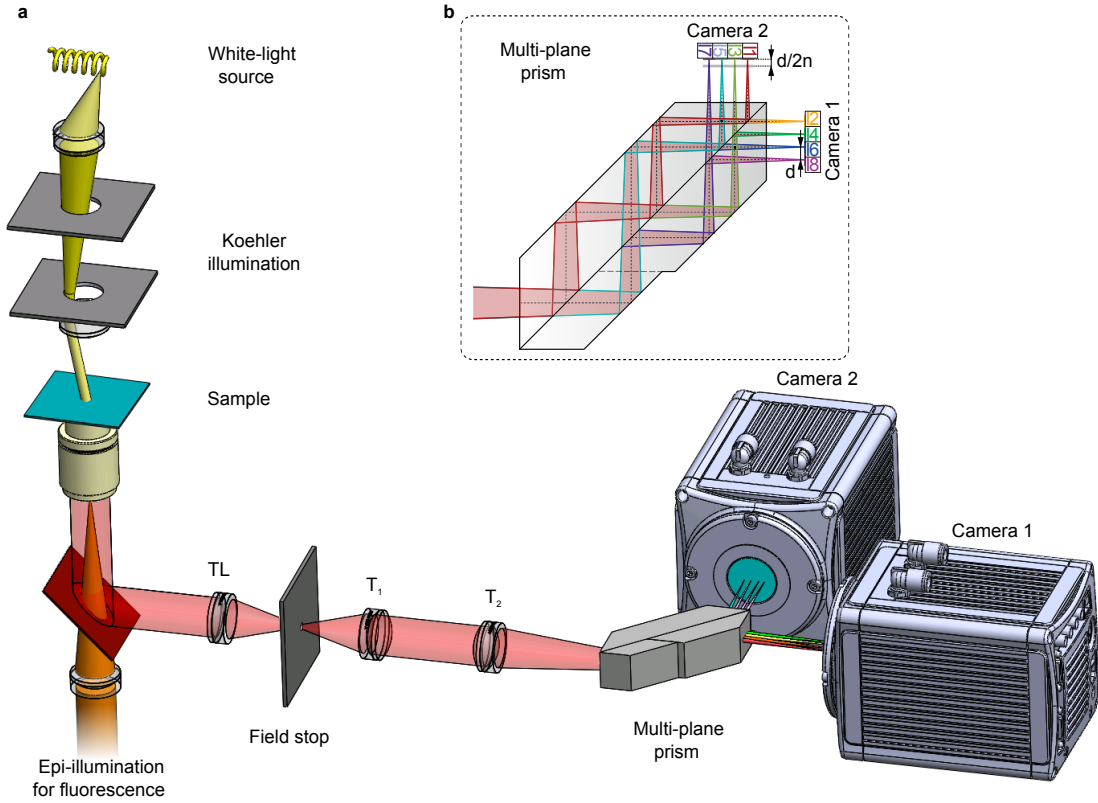
Figure 2.11 – Overview of the PRISM setup. (a) Microscope layout combining epi-fluorescence illumination and white-light Koehler illumination for 3D phase retrieval with the multi-plane imaging platform. TL tube lens, T1 and T2 telescope lenses. (b) Multi-plane image splitter (for all specifications and parameters see Section A.2).

Due to the classical layout of the microscope, adding an epi-illumination fluorescence channel is straightforward (see Fig. 2.11). The combination of both imaging modalities merges the advantages of phase microscopy such as label-free, long-term dynamic cell imaging with the complementary features of fluorescence, e.g. molecular specificity and single molecule detection. We named our multi-plane microscope Phase Retrieval Instrument with Super-resolution Microscopy (PRISM), as wide-field super-resolution imaging can be easily integrated via the fluorescence channel.

PRISM splits the fluorescence signal into eight simultaneously acquired depth images and is ideally suited for 3D Super-resolution Optical Fluctuation Imaging (SOFI). Fast, background-free, super-resolution imaging with inherent optical sectioning is possible by analysing time-series of independent, stochastically blinking emitters with higher-order cumulant statistics[65]. SOFI can be applied on the same dataset as (d)STORM and PALM[80, 81]. It also provides reliable results for high labelling densities and limited photon budget, which is an advantage for analysis of the brightness reduced multi-plane images. Cross-correlation (or precisely cross-cumulant) analysis is not limited to the lateral dimension. In consequence, if the inter-plane distance is adjusted smaller than the axial PSF extent and the 3D image

stack is acquired simultaneously, a 3D super-resolved image acquisition can be realized. The parallel acquisition significantly reduces the overall imaging time and thus the photobleaching compared to sequential recording of image stacks. We demonstrated a lateral resolution of 110 nm and an axial resolution better than 500 nm for 3rd order 3D SOFI[69]. The chosen specifications for the new MP configuration allows a robust multiplexed image acquisition matching all these requirements. Using PRISM, we demonstrate high-speed live cell phase microscopy and the combination of SOFI with phase imaging in 3D.

2.7   High-speed dynamic 3D phase imaging

To highlight the fast acquisition of PRISM 3D phase imaging, we monitored a living human fibroblast at an imaging speed of 200 Hz as it migrates on a glass substrate. The overview in Fig. 2.12a shows the cell body with the nucleus and lamellipodia extending into the direction of migration for a selected plane. The membrane of the nuclear envelope separating the nucleus from the cytoplasm is clearly visible. In the zoomed region of interest (green-dashed square in Fig. 2.12a), the fast movement of a vesicle (white circle) and an apparent fusion of two small organelles (white arrow) are indicated (Fig. 2.12b). A kymograph perpendicular to the leading edge of the cell (along the magenta line in Fig. 2.12a) shows membrane ruffles that move centripetally towards the main body[82] (Fig. 2.12c). Intracellular vesicle movement in 3D can be observed in the close-up of a color-coded maximum phase z-projection of the green-dashed region of interest (Fig 2.12d, the particle that is indicated moves up and down (yellow-red-yellow)).

2.8   Combining SOFI and phase imaging

We explored the full potential of our PRISM multimodal multi-plane imaging by investigating different cell types using super-resolution optical fluctuation imaging followed by phase imaging, both in 3D (Fig. 2.13). As a proof of principle, we first acquired image sequences of microtubules in fixed HeLa cells that were fluorescently labelled with Alexa Fluor 647 by indirect immunostaining. We obtained 3D super-resolved images by computing second and third order bSOFI[68] images of the fluctuating signals of blinking labels (Fig. 2.13a). This SOFI implementation linearizes the brightness response of the cumulants to balance the image contrast. The optical sectioning capability and the removal of out-of-focus background are apparent in the bSOFI images. A selected xy-plane displays the rich (intra-) cellular context provided by the subsequently acquired corresponding phase tomogram (Fig. 2.13d). Clearly, the cell nucleus coincides with the void volume that is surrounded by the labelled cytoskeleton filaments, whose network extends almost to the outline of the cell. A color-coded maximum z-projection of the green-dashed region of interest indicated in the 2D phase illustrates the 3D nature of the phase images (Fig. 2.13g). Our correlative phase and bSOFI images are intrinsically co-aligned, as they were taken successively using the MP microscope without moving the sample.
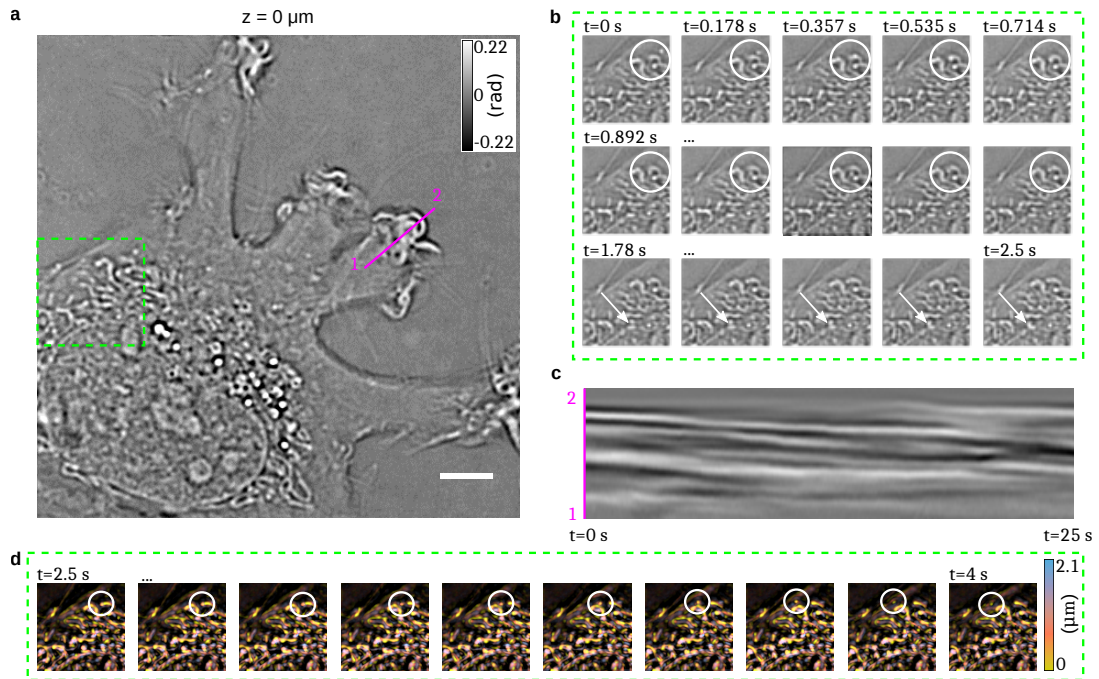
Figure 2.12 – Fast live cell 3D phase imaging of cellular dynamics. (a) Human fibroblast migrating on a glass substrate. First frame of a 25s movie imaged at 200 Hz for a selected plane. (b) Close-up of the green-dashed ROI indicated in (a) at different times illustrates intracellular organelle movement, indicated by a white circle and a white arrow. (c) Kymograph for every 10th frame along the magenta line 1-2 in (a) shows ruffling of lamellipodia. (d) Close-up of the green-dashed ROI indicated in (a) across all planes at different times illustrates intracellular organelle movement in axial direction, indicated by a white circle. Phase color-coded maximum z-projection (threshold T = 0 rad). Scale bar 5 μm.

Fig. 2.13b, e and h summarize the imaging of mouse hippocampal primary neurons that were treated with α-synuclein fibrils. The protein is abundant in the brain and abnormal accumulation of aggregates is a characteristic for a number of neurodegenerative diseases including Parkinson's[83]. SOFI reveals the 3D architecture of newly formed Alexa Fluor 647-immunostained α-synuclein aggregates (Fig. 2.13b). Several long fibres extend over the whole imaging depth. The corresponding phase tomogram (Fig. 2.13e, h) shows that, in this case, most of the α-synuclein aggregates are found within a bundle of neurites. The outline of a neuronal cell body is barely visible slightly off the centre of the 2D image.

Next, we investigated live cells with 3D phase imaging and SOFI. To do so, we transfected RAW 264.7 macrophages with a reversibly photoswitchable fluorescent protein construct, Lifeact-Dreiklang. This fluorescent fusion protein labels actin filaments in live cells[84], that are visualized in 2nd order bSOFI (Fig. 2.13c). A visual comparison between fluorescence and phase imaging reveals that only one out of five cells in the field of view are expressing Lifeact-Dreiklang (Fig. 2.13c, f). The semi-adherent macrophages have a round shape with several thin, actin driven protrusions that emerge from the cellular membrane.
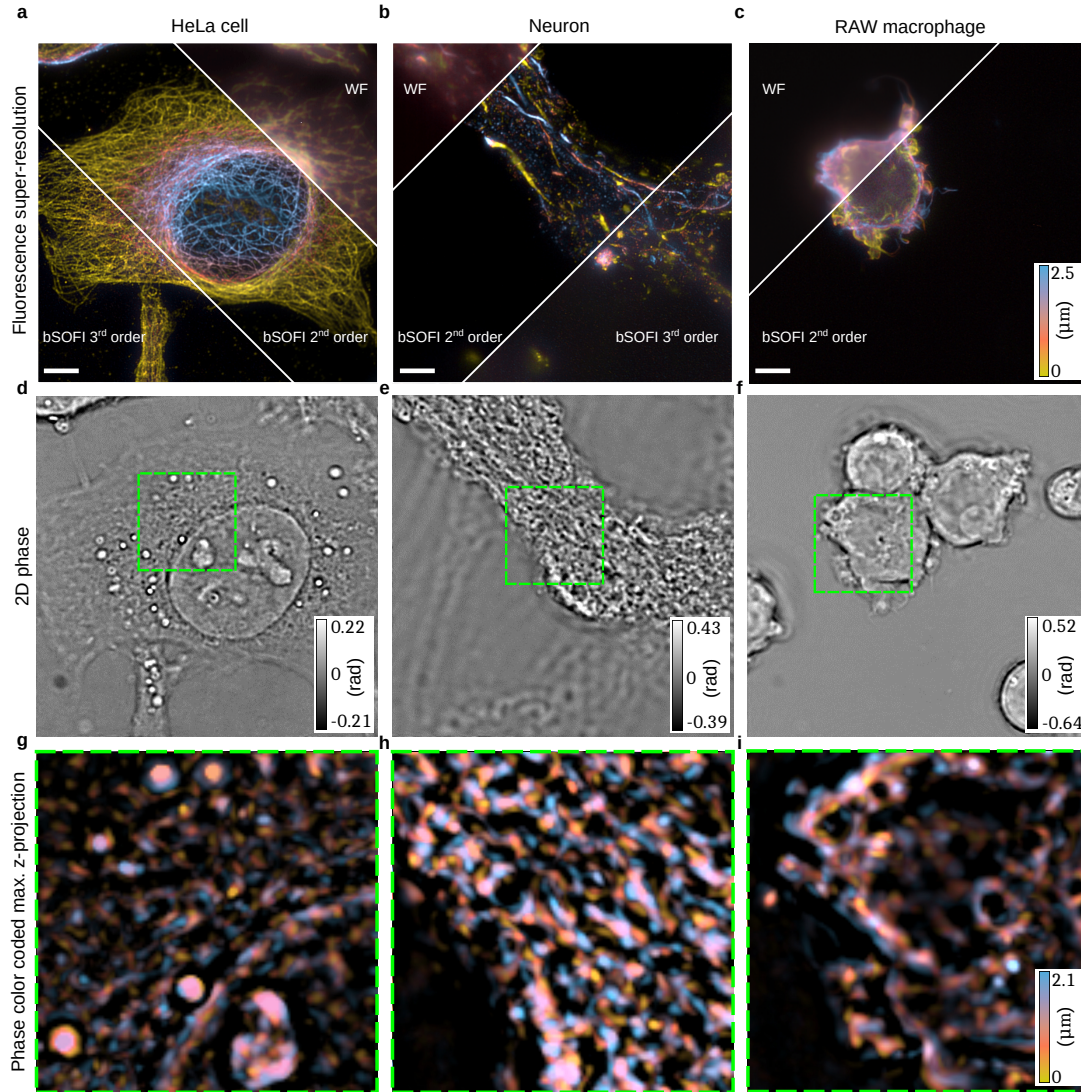
Figure 2.13 – Multi-plane SOFI and phase imaging. SOFI maximum intensity projection, selected 2D phase image, and colour coded maximum phase z-projection of the corresponding highlighted area (threshold T = 0 rad). (a), (d), (g) HeLa cell with Alexa Fluor 647 antibody-labelled microtubules, (b), (e), (h) mouse hippocampal primary neurites incubated with external α-synuclein fibrils and immunostained for newly formed α-synuclein aggregates Alexa647 and (c), (f), (i) live murine RAW 264.7 macrophages expressing Lifeact-Dreiklang. SOFI acquisition at 50 Hz of 5000 frames for Alexa647 and of 3000 frames for Dreiklang imaging. Subsequent phase imaging camera exposure time 20 ms, Scale bar 5 μm.

2.9 Summary and discussion

We provide a novel concept for retrieving the phase information in all 3 spatial dimensions. The theory is based on the Helmholtz wave equation and is embedded in the framework of the generalized Wiener-Khintchine theorem[71]. We consider elastic light scattering using the first order Born approximation. An Ewald sphere construction reveals the attainable frequency

support of the image spectrum. Measuring the interference of the forward weak scattering with the illumination enables decoding of the phase information along the z-direction. The theoretical effort goes in parallel with a fast and elegant algorithm comprising a masking operation to recover the 3D phase information from an acquired volumetric intensity stack. The common-path configuration integrated with white-light Koehler illumination and high detection NA provides stable and speckle-free high-resolution quantitative phase imaging of sub-cellular structures. Our simulations confirmed and matched an experimental lateral and axial resolution of 350 nm and 560 nm. We demonstrated the quantitative nature of our method by assessing the relative step heights of a nanometric phase object, referenced using AFM measurements and confirmed by imaging polystyrene beads of known size. The method allows one to upgrade a classical bright-field microscope into a simple and reliable 3D phase microscope.

The experimental counterpart is based on an innovative multi-plane configuration, containing an image splitting prism for "volumetric" multiplexing, i.e. the simultaneous acquisition of 8 images originating from 8 conjugated object planes with an inter-plane distance of 350 nm. Our Phase Retrieval Instrument with Super-resolution Microscopy (PRISM) combines fast 3D phase imaging with 3D fluorescence super-resolution microscopy for a unique 4D imaging modality.

This powerful and innovative concept opens the door to a wide range of applications, here demonstrated by imaging different cell samples. As shown, retrieving the 3D phase information at an acquisition rate up to 200 Hz responds to an ever growing demand for imaging fast dynamic cell processes. However, the gain in acquisition rate based on phase imaging is paired with a lack of specificity. Since our proposed MP configuration allows super-resolved fluorescence imaging based on super-resolution optical fluctuation imaging, fluorescence based specificity and high acquisition speed are realized in the same 3D platform. This multimodal and versatile microscope promises to fulfil the expectations for many novel applications and investigation in biology and life sciences.

3 Multi-plane SIM, High power high-speed multi-color SIM and experimental combination of SOFI with SIM

3.1 High speed multi-plane Structured Illumination Microscopy of living cells using an image-splitting prism

Super-resolution structured illumination microscopy (SR-SIM) can be conducted at video-rate acquisition speeds when combined with high-speed spatial light modulators and sCMOS cameras, rendering it particularly suitable for live cell imaging. If, however, three-dimensional (3D) information is desired, the sequential acquisition of vertical image stacks employed by current setups significantly slows down the acquisition process. In this work we present a multi-plane approach to SR-SIM that overcomes this slowdown via the simultaneous acquisition of multiple object planes, employing a recently introduced multi-plane image splitting prism combined with high-speed SIM illumination. This strategy requires only the introduction of a single optical element and the addition of a second camera to acquire a laterally highly resolved three-dimensional image stack. We demonstrate the performance of multi-plane SIM by applying this instrument to imaging the dynamics of mitochondria in living COS-7 cells.

The following section is the preprint version of the published manuscript

[1]LBEN and LOB, EPFL, 1015 Lausanne, Switzerland
[2]Biomolecular Photonics Group, Bielefeld University, Bielefeld, Germany
[3]Nanobiology Lab, KU Leuven, Leuven, Belgium

Chapter 3. Multi-plane SIM, High power high-speed multi-color SIM and experimental combination of SOFI with SIM

3.1.1 Introduction

Conventional fluorescence microscopy is inherently limited in its spatial resolution due to diffraction. Optical super-resolution imaging techniques allow us to overcome this limitation. For super-resolution structured illumination microscopy (SR-SIM) this is achieved by using high spatial illumination frequencies that down-modulate spatial frequencies beyond the cut-off into the passband of the microscope[29, 43, 85, 86].

Linear implementations of SR-SIM create a sinusoidal interference pattern in the sample plane, leading to a spatial resolution improvement of at best two-fold over wide-field microscopy, and additional contrast enhancement for high spatial frequencies and strong suppression of out-of-focus light by filling the missing cone of the instrument's optical transfer function[43, 87, 88]. In return, only a small number of raw images with defined illumination patterns (9 in the standard 2D implementation, less when using advanced algorithms[89]) are needed for the image reconstruction process. The excitation powers are comparable to conventional wide-field imaging, so photo-damage can be minimized, and no special dyes (e.g. dyes that are photo-switchable or inherently blinking) are required for the approximately two-fold resolution enhancement. The combination of these features makes SR-SIM a very fast super-resolution imaging technique, with current instruments[90, 91] providing 2D imaging with approximately 100 nm spatial resolution in the lateral direction at video-rate speed and even faster.

Live-cell imaging is the primary domain for SR-SIM. Here, its high temporal resolution excels, especially when observing highly dynamic processes on sub-second time-scales. If, however, 3D volumetric imaging is required, current state-of-the-art SR-SIM systems slow down the acquisition rate significantly, due to the need to physically move the object through the focal plane, e.g. by piezo-translation stages. The slowdown arises not just from the repeated image acquisitions, but also from the intermediate sample movement that needs to be accounted for. Also, advanced control electronics are required if stage movement, SR-SIM illumination and camera exposure are to be synchronized precisely.

Such delays can be avoided if a full 3D volume of the sample could be acquired at once. Two different approaches to multi-plane image detection currently exist: A diffractive element, based on a phase-shifting spatial light modulator (SLM) or a lithographically-produced optical element[92, 93], can be introduced into a conjugated image plane and create almost arbitrary multi-plane detection schemes. Chromatic aberrations can be corrected using additional elements[94]. Recently, this approach was combined with a commercial SR-SIM microscope[95] and provided the first multi-plane SR-SIM images in a prototype system. Although this proved to be a great demonstration of the future of SR-SIM imaging, these tests ended up being limited by the slow speed of the commercial SR-SIM platform, which was not originally conceived for video-rate super-resolution imaging. Here, we present a multi-plane imaging approach to SR-SIM that circumvents these issues and achieves high-speed imaging rates previously only available to 2D SR-SIM.

3.1. High speed multi-plane Structured Illumination Microscopy of living cells using an image-splitting prism
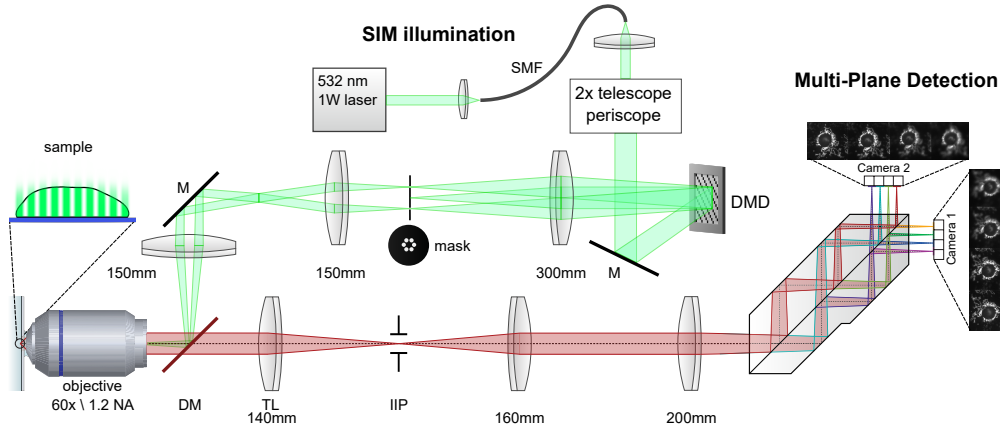

Figure 3.1 – Opto-mechanical schematics of the high-speed multi-plane SR-SIM imaging system. The SR-SIM pattern is created by a 532 nm 1 W laser (Roithner) coupled into a single mode fiber for mode cleaning. The light at the distal end of the fiber is then collimated, expanded by a factor of 2 and directed onto a digital micro-mirror device (DMD), which is used as a fast, electronically controlled optical grating. A segmented aperture mask removes spurious diffraction orders, arising due to the binary nature of the DMD. A relay lens system focuses the light into the back focal plane of the objective lens (Olympus UPLSAPO 60 x/1.2 NA water immersion). Excitation and emission light is wavelength-separated by a dichroic mirror (DM). In the detection path, the tube lens (TL) forms an intermediate image (*Image Plane*), where a field stop (IIP) sets the field-of-view size and prevents overlapping signals in the multi-plane detection system. A magnification of 58.5 x is achieved, which corresponds to a projected pixel size of 111 nm for the sCMOS cameras (ORCA Flash 4.0, Hamamatsu). Lenses form a relay telescope into the main component, the precision-made multi-plane prism [79]. It provides 2 × 4 copies of the image onto 2 scientific sCMOS cameras, where each copy has a defined path-length difference and thus defined, axially offset focal plane.

3.1.2 Multi-plane SIM

Our work is based upon an imaging strategy for multi-plane detection that divides the detected fluorescence light into multiple image planes by introducing discrete optical path length differences to the image path [69, 79, 96]. This path length difference guarantees perfect object-image conjugation for 8 object planes equally displaced along the axial direction. As seen in Fig. 3.1, the classical 8f set-up of the detection path allows us to easily realize a telecentric instrument ensuring identical scaling of all 8 images obtained from different axially displaced object planes.

While image splitting via subsequent changes in detection path length is a robust concept, its typical implementation with discrete optical elements is sensitive to thermal drifts and vibration and rather difficult to align. A recent development[79] solved this problem by integrating this approach into a single, stable, precision-made optical element: a compound image-splitting prism. This device allows for the simultaneous detection of up to 8 diffraction limited images obtained at equally spaced vertical planes with only minimal alignment of the overall optical set-up. Compared to diffraction based multi-plane microscopy[95], our
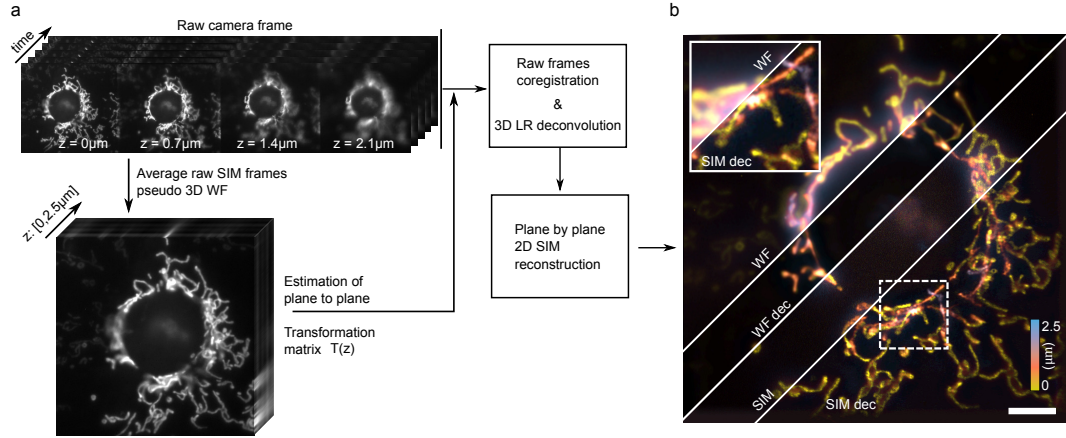
Figure 3.2 – Data processing and SIM image reconstruction procedure. (a) The raw images are first averaged to produce a pseudo wide-field image. This image is then used to estimate the inter-plane transformation matrix $T(z)$. This matrix is used to coregister the raw SIM images and reorder the data in x,y,z,t space. Then, the data is either averaged (WF), deconvolved in 3D (WF dec), reconstructed (SIM) or deconvolved and reconstructed (SIM dec). (b) Color coded maximum intensity z-projection of 3D images for all 4 modalities on a fixed COS-7 cells labelled with MitoTracker Orange. Inset shows a zoomed in comparison between WF and deconvolved SIM. Scale bar 5 μm.

approach has the advantage that the prism consists of a single, compound refractive element instead of 2 separate gratings and a refractive correction prism. This greatly improves the stability and simplifies the alignment of the system. While the diffractive solution can in principle be tailored to a specific imaging application, the method presented here is very versatile, and, through a careful selection of tube lenses, can be used at any wavelength, allowing for example 3D correlative microscopy [79].

We combined our prism-based detection path with a coherent SIM excitation path based on a high-speed digital mirror device (DMD - DLP7000, Vialux) and a high-power laser (532 nm, 1W, Roithner). By utilizing two synchronized sCMOS cameras (Hamamatsu Orcaflash V4.0), we achieved high-speed volumetric imaging with 50 ms exposure time. Taking camera readout and device synchronization into account, this results in about 1.3 reconstructed SIM data sets per second, to image a full volume of about $40 \times 40 \times 2.45 \, \mu m^3$. Both the DMD-based spatial light modulator and the cameras could, in principle, be tuned to provide even higher imaging speeds[90], if required by the application and if sufficiently bright fluorophores are used to compensate for the lower signal to noise ratio.

In its current configuration, the SIM is operated in coherent *two-beam* mode. Here, the $\pm 1^{st}$ diffraction orders generated by the DMD grating pattern can interfere in the sample plane to generate a lateral modulation of the excitation pattern. The 0th order is blocked, so no axial modulation of the SIM pattern is introduced. This approach sacrifices the axial resolution improvement possible in full three-beam SIM, but comes with a set of advantages. First of
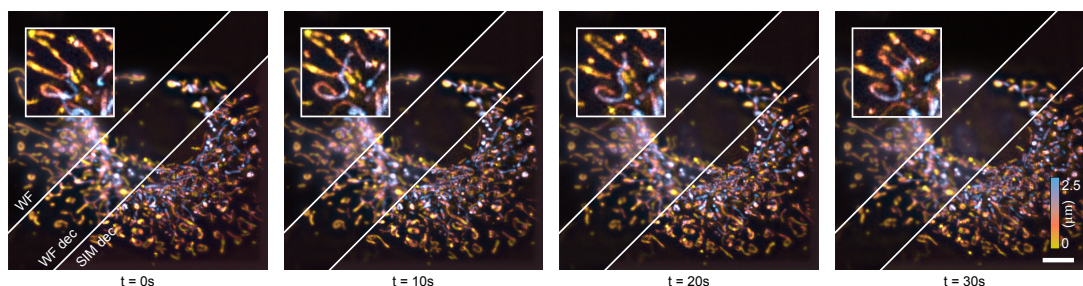
Figure 3.3 – Time series of SR-SIM imaging data following mitochondrial dynamics (stained with MitoTracker Orange) in COS-7 cells, color coded maximum intensity z-projection of the deconvolved and SIM reconstructed 8 planes (see Fig. 3.2). The full series contains 74 time points, each acquired with 50 ms SR-SIM acquisition time to allow for motion-artifact-free imaging (see Visualization 1). The series has been renormalized in brightness to compensate for photo-bleaching, but no further processing beyond a standard SIM reconstruction had to be performed. Insets (FOV $7x7\,\mu m^2$) show deconvolved SIM exhibiting high spatial motility of the mitochondria during the imaging. Scale bar 5 μm.

all, including SIM modulation along the axial direction would entail aligning each z-plane with the axial periodicity of the SIM pattern, which would take away some of the systems robustness and simplicity. Also, the acquisition of 15 instead of 9 raw images is required for a direct SIM reconstruction of three-beam SIM data, which impacts overall imaging speed, as well as sample photobleaching and phototoxicity. Most importantly, the optical sectioning intrinsically provided by three-beam SIM can also be obtained in a two-beam approach (albeit at lower axial resolution) by trading in some of the lateral resolution enhancement for optical sectioning capability. In brief, using a slightly coarser SIM pattern (frequency of $1.8\,\mu m^{-1}$, or 555nm periodicity, here) leads to an overlap of the shifted copies of the optical transfer function obtained by SIM, which, in turn, allows to fill their missing cone and thus provides axial sectioning [87, 88].

Additionally, using a coarser SIM pattern simplifies the aspect of polarization control. For optimal pattern contrast, the polarization of the interfering beams would have to be rotated to match the three orientations of the SIM pattern. However, when using a coarser pattern, and thus steeper interference angles, the influence of polarization becomes less pronounced[97]. This allows us to use a fixed linear polarization while maintaining reasonable pattern modulation contrast for all pattern orientations, which both simplifies the optical setup and avoids light loss in the filter elements that would otherwise occur. To summarise, we tuned the SIM system to a compromise of both optical sectioning and lateral resolution improvement, while operating at the minimum of 9 raw SIM frames to achieve high imaging speeds.

3.1.3 Results

We applied our multi-plane SIM system to the fast imaging of mitochondrial dynamics [98, 99]. Here, SIM is an enabling imaging method, as its increase in spatial resolution and inherent

background suppression allows us to visualize the mitochondria and their three-dimensional morphology and dynamic changes thereof which cannot be observed with conventional wide-field resolution [37]. Furthermore, the rapid movement of mitochondria requires high imaging speed, while their three-dimensional nature greatly benefits from acquiring signals from multiple z-planes. However, the structures are still rather "thin" compared to their length, and a coverage of $2.45\,\mu$m (8 planes with an axial sampling of 350 nm) as provided by our system is typically sufficient to capture the entire three-dimensional mitochondrial structure in a single shot multi-plane exposure. In this case, no axial movement of the sample is needed at all, which greatly simplifies data acquisition and decreases the acquisition time. The data processing and results are presented in Fig. 3.2, where our imaging was performed with 50 ms exposure time per raw data frame. As mentioned earlier, 3 angles and 3 phases are required for the 2D SIM image reconstruction process, thus reaching 770 ms acquisition time for the full imaged volume.

Fig. 3.2a summarizes the flow of data. A key challenge is that the the 8 planes are all slightly shifted with respect to each other, due to unavoidable limitations in the prism manufacturing. By cross-correlating two consecutive planes, we are able to recover the prism transformation matrix $T(z)$ and perform a sub-pixel coregistration for all the raw SIM frames. We then average all the frames to form a pseudo-widefield image (WF), deconvolve the 3D WF using 10 iterations of Lucy-Richardson (LR) deconvolution (deconvlucy, Matlab 2017b), reconstruct the SIM image plane by plane (SIM) or deconvolve in 3D the raw SIM frames and reconstruct the SIM images plane by plane (SIM dec). Results are shown in Fig. 3.2b, where we encoded the depth information using a color-coded maximum z-projection. Using the recently introduced image resolution estimation method [100], we measure a resolution of 460nm for WF and 434nm for WF dec. This relatively high value is due to the presence of out-of-focus light, which is partially removed by the 3D deconvolution. For SIM, we measure 266nm (263nm for SIM dec), which corresponds to a resolution gain of about 1.7 compared to WF. We note that for SIM, the deconvolution mostly improves the image contrast and does not change the resolution.

We used a custom 2D SIM reconstruction algorithm implemented in Matlab, following closely the work from [101]. For the 3D LR deconvolution, we used an experimentally acquired 3D PSF of the setup, obtained by imaging, localizing and averaging the 3D image of 15 sparsely distributed sub-diffraction (100nm diameter) fluorescent beads.

In Fig. 3.3, the time series of a second data set is shown. With an exposure time of 50 ms we achieved about 1.3 fps volumetric SIM imaging speed. We estimate for the resolution 520nm for WF, 460nm for WF dec, 375nm for SIM and 265nm for SIM dec. The small degradation of resolution for SIM and WF is due to unavoidable sample movement. No further degradation of resolution over time is observed. However, we find (see Visualization 1) that this speed allows us to capture the 3D dynamics of the mitochondrial network. While the reconstructed sequence had to be bleach-corrected by normalizing the average of each frame, 74 time points (about 60 sec) could easily be acquired, without the need to resort to any advanced image reconstruction algorithms.

3.1.4   Conclusion

The results presented here demonstrate the first proof-of-concept of high-speed two-beam multi-plane SIM imaging of living cells using an image-splitting prism. They show that the combination of multi-plane image detection with fast two-beam SIM illumination indeed yields the desired high speed volumetric imaging. These results also indicate that this system is well suited to image mitochondrial dynamics, as both the necessary temporal and spatial resolution is reached.

Our work also provides several insights into current limitations and challenges. For example, the current DMD implementation encounters significant losses of the excitation light due to spurious diffraction, with a maximum of about 3 mW reaching the sample (single-mode fiber coupling: 25%, DMD transmission: 6%, SIM mask: 30%, dichroic and objective lens: 70%). Newer liquid crystal on silicon (LCOS)-based designs will allow for a 10× improvement in power management albeit at the cost of more complex timing requirements. By utilizing polarization control and higher pattern frequencies, the lateral spatial resolution could also be pushed towards ~ 130 nm. In combination with more advanced algorithms taking full advantage of the 3D information for low signal to noise image reconstruction, we envision that 5-10 ms exposure times, and thus volumetric imaging within 50-100 ms will be possible.

Very recent development into advanced denoising SR-SIM reconstruction algorithms[102] point to solutions that will allow for the use of significantly lower signal levels in the image reconstructions, and thus might allow us to push for even faster imaging speed. Advanced fluorescent dyes will allow for even more extended observation times. Novel, smart data-driven feedback loops should also be able to dynamically adapt the imaging speed depending on the observed dynamics. These approaches will all complement multi-plane video-rate SR-SIM imaging quite well.

In its current state, image-splitting multi-plane SR-SIM technology provides an early demonstration of what this technology will be able to achieve in more improved configurations. As the approaches and their implementations evolve, we believe they will provide an important tool for future high-speed super-resolution 3D imaging of living cells and organisms.

Sample preparation and staining

#1.5 cover glass coverslips were cleaned with a piranha solution and coated with fibronectin (0.5 μM/ml). Cells were grown in DMEM without phenol red medium, containing 10 % of fetal bovine serum. Mitochondria were stained with 100 nM MitoTracker Orange (Thermo Fisher) according to manufacturer-provided staining protocol for 30 min. Then cells were either fixed with 4% PFA or used for live cell imaging. For live-cell imaging, cells were washed twice with grown medium and imaged in PBS pH=7.4, which proved to reduce background fluorescence and short-term imaging was perform in a custom build incubator at 37 ° C.

3.2 High power high-speed multi-color SIM

In order to generate a high frequency sinusoidal pattern in the sample plane, two coherent beams need to interfere at the sample location. As already presented in the introduction, several solutions (fixed phase grating, liquid crystal device, digital micro-mirror device) exist with different limitations regarding speed, losses, multi-color compatibility and complexity. In particular, the use of a digital micro mirror device, presented in Chapter 3, allows for flexible and high speed projection of a variety of patterns. It however suffers from very high losses due to unavoidable diffraction of light outside of the optical path. The use of a grating to generate the structured illumination also complicates the implementation of several illumination colors since the diffraction pattern strongly depends on the wavelength.

Here we report the design of an achromatic, high power, fast SIM illumination design. The setup can operate in two or three-beams configuration, is compatible with polarization control and can in principle reach 100% transmission efficiency. We start by describing how the pattern is generated and show its performance on fixed cell sample. We then demonstrate the ability of the setup to achieve multi-color SIM imaging. Finally, we show the first experimental realization of the combination of SOFI with SIM.

The setup is presented in Fig. 3.4 and note that the SIM design and the ideas presented in this chapter were obtained independently of the publication [103].
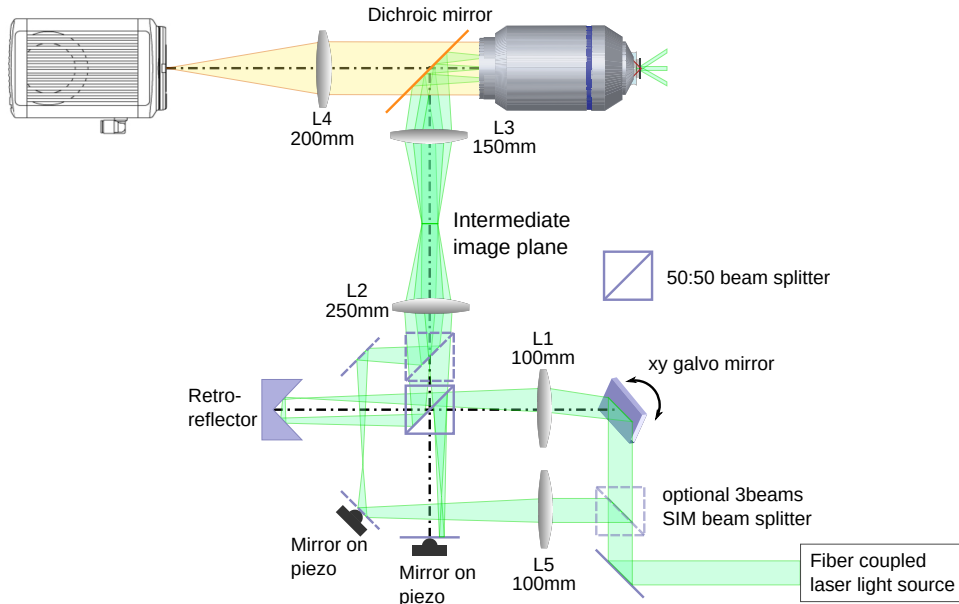

Figure 3.4 – Achromatic high-power fast SIM setup. The setup description is provided in the text.

A collimated laser light beam is directed towards a 2-axis galvanometer mirror (GVSM002-EC/M, Thorlabs), located at a distance f of the lens L1 (f=100 mm). The converging beam is then sent in a balanced Michelson interferometer. One arm consists of a mirror mounted

on a piezo (PE4, Thorlabs, Open loop control) to provide fast phase modulation. The second arm consists of a fixed hollow retro-reflector (HRR201-P01, Thorlabs) which laterally shifts the beam. Both beams are then collimated by the lens L2 (f=250 mm) to form the intermediate illumination image plane where both beams interfere and form a sinusoidal pattern. For 3beams SIM mode, two additional beam splitters and the lens L5 (f=100 mm) have to be placed before the galvo system and after the Michelson interferometer and another mirror mounted on a piezo is required to modulate the phase of the central beam. The pattern is then imaged on the sample using the lens L4 (f=150 mm) and the objective (Olympus water immersion 60x, 1.2 NA). The fluorescence collected by the objective is transmitted by the dichroic (AHF, TIRF Quad Line Beam splitter zt405/488/561/647rpc) and focused on the camera (Hammamatsu Orca Flash V4.2) by the tube lens L4 (f=200 mm). The residual laser light is filtered using a Quad Line Laser Rejection band (AHF, ZET405/488/561/647).

Since we avoid the use of a grating, the proposed SIM illumination is well suited for multi-color imaging. The galvanometer system and piezo can easily be driven in the millisecond range. The limiting speed factor is then given by the fluorescence signal or the camera frame rate. The illumination is also compatible with polarization control for optimal pattern contrast. With the use of a polarized beam splitter and quarter wave-plates, 100% of the light can in theory be directed towards the sample. In its current implementation, we measure an illumination efficiency of 40%, the losses being mainly due to the beam splitter.

3.2.1 System control and calibration
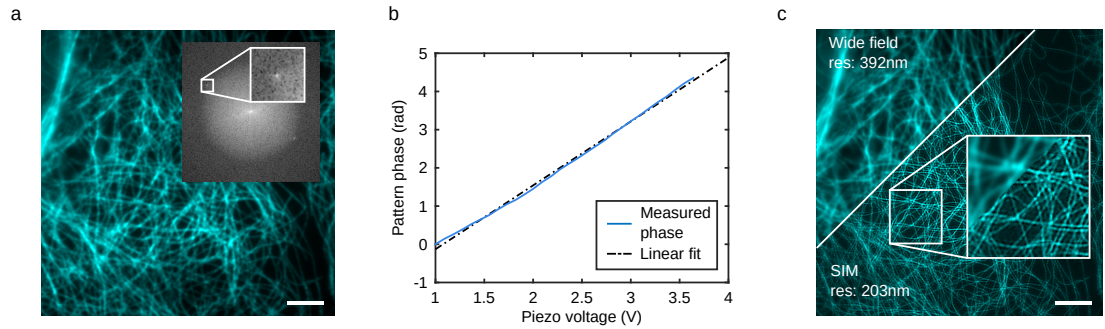
Figure 3.5 – Setup calibration (a) Atto565 stained microtubules of fixed COS7 cells with pattern projected near microscope cut off (inset: log of absolute Fourier transform of (a) showing the presence of a sinusoidal pattern). (b) Estimated pattern phase as a function of voltage applied to piezo. (c) SIM reconstruction using 3 angles and 3 phases. Resolution estimated using the method presented in chapter 5. Scale bar 5 μm.

The Fig. 3.5a shows a typical image of atto565 stained microtubules of fixed COS7 cells using a water immersion objective ($60x$, NA = 1.2) and an Hammamatsu Orca Flash V4.2 (projected pixel size of 97 nm). By applying a voltage to the 2-axis galvanometer system ($V_x = 2.1$ V, $V_y = 3.19$ V), we generate a 2D sinusoidal illumination (laser wavelength of 561 nm) with a period of 390 nm. Since this pattern is close to the cut off of the system, it is barely visible in real space. We show in inset of Fig. 3.5a the log of absolute Fourier transform of Fig.

3.5a, which indicates the presence of the pattern in the form of two peaks close to the image frequency support.

To ensure equally spaced phase between each SIM pattern, it is mandatory to calibrate the change of the pattern phase as a function of the voltage applied to the piezo. Fig. 3.5b shows the result of the calibration. The pattern phase was estimated following the work of Wicker et. all. [39]. We see that the response of the piezo is nearly linear and that 5 V analog voltage output can almost produce a full revolution of the pattern phase.

Finally we show in Fig. 3.5c the result of a 2D SIM reconstruction using 3 angles and 3 phases (custom SIM reconstruction algorithm, see Appendix C), with an exposure time of 50 ms per frame. Using the method presented in chapter 5, we estimate a wide field resolution of 392 nm and a SIM resolution of 203 nm, which is expected since the pattern frequency is located at the edge of the wide field frequency support. The illumination frequency k_i is almost equal to the frequency support of the object k_c and the SIM reconstruction will have a frequency support of $\approx k_c + k_i \approx 2k_c$.

To reliably handle the camera triggering and voltage control sequence of the piezo and galvo system, we rely on a FPGA board (NI 9147 4 Slot Ethernet Expansion chassis) equipped with 8 0-5 V analogue outputs (NI-9381). The programming of the board was done using Labview FPGA and enable the acquisition of raw SIM frames at 1 ms exposure time. The current system frame rate is currently limited by the readout time of the camera (Hammamatsu Orca Flash V4.2) of about 4.5 ms in single frame trigger mode.

3.2.2   Multi-color SIM

In order to demonstrate the ability of the setup to perform sequential multi-color SIM, we imaged dense layer of fluorescent tetra-speck beads (T7280, ThermoFisher) with a diameter of 200 nm deposited on a glass coverslip. For the demonstration, we used a laser combiner (MLC 400B, Agilent Technologies) with 488, 561 and 647 nm laser lines. For each color channel, the laser power was adjusted to stay close to saturation of the camera (exposure time of 30 ms). We projected 5 angles with 3 phases per angle with variable pattern period.

The results are shown in Fig. 3.6. Fig. 3.6a shows the wide field and SIM reconstruction using a laser wavelength of 647 nm. We estimate a resolution of 450 nm and 245 nm for the wide field and SIM image. The resolution improvement is consistent with the used pattern period of 477 nm. Fig. 3.6b shows the same sample imaged at 561 nm. As expected, the wide field resolution slightly decreases to 380 nm. The SIM resolution of 228 nm is also consistent with the pattern period of 510 nm. Fig. 3.6c shows the same sample imaged at 488 nm with a pattern period of 359 nm. We measure a resolution of 350 nm for wide field and 203 nm for SIM. Since the pattern period is almost equal to the wide field resolution, we expect to observe a two fold improvement of the resolution. The resolution estimation is limited by the sample since we are using 200 nm beads. The image in not diffraction limited but it is the object itself that does not contain any higher frequencies (see also section 4.4.2). Finally, Fig. 3.6d shows line
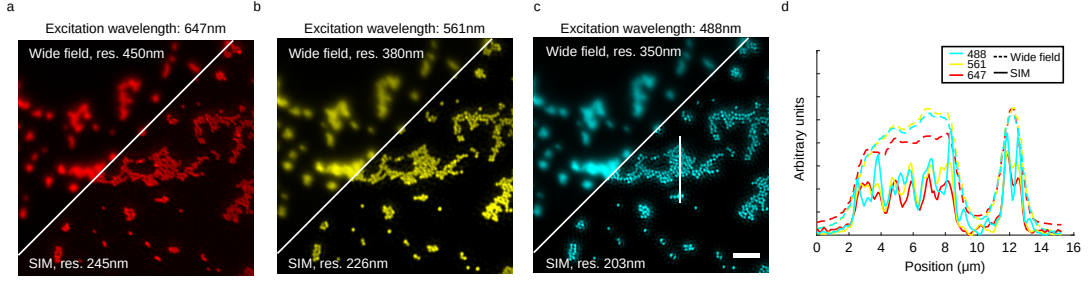
Figure 3.6 – Multi-color SIM imaging on beads sample. (a) Wide-field and SIM at 647 nm. (b)Wide-field and SIM at 561 nm. (c) Wide-field and SIM at 488 nm. (d) Line profile indicated in (c). Scale bar 5 μm.

profiles (indicated in Fig. 3.6c) of all the imaging conditions.

The next step of this project would be to implement the laser combiner into the Labview control software, optimize the pattern frequency as a function of the wavelength and image a live cell sample at high speed.

3.3 SOFI-SIM

The non-linear response of SOFI can be combined with SIM to achieve resolution improvement unreachable by the techniques alone[104, 105]. In theory, 4th order SOFI-SIM could outperform 25th order SOFI, which would be of high interest for the imaging of live samples with very high label density.

The image formation is nearly identical to the one presented in the introduction (see equation 1.32), except for the dye brightness which is now modulated by the position dependent pattern intensity $p(\mathbf{x_i})$. We have for the nth order SOFI image

$$\kappa_n(\mathbf{x}) = \sum_i^N A_i^n p^n(\mathbf{x_i}) U^n(\mathbf{x} - \mathbf{x_i}) \kappa_n\{s_i(t)\} + \kappa_n\{b(\mathbf{x})\} + \kappa_n\{n([x], t)\} \tag{3.1}$$

The SOFI image is now modulated with a non-linear pattern $p^n(\mathbf{x})$ which has been raised to the nth power. Taking a sinusoidal function to the nth power gives rise to high-frequency harmonics, carrying sample information lying outside of the frequency support of the same SOFI image without any modulations. By shifting the phase of the pattern and acquiring more SOFI image ($2n + 1$ per angle), we can unmix the contributions of the different harmonics and increase the resolution of the SOFI image.

In theory, we expect a resolution increase of $\sqrt{n} + n$, where $\sqrt{n}$ is the contribution of the non-linearised SOFI cumulants and n is the contribution of the non-linear SIM reconstruction. In practice, there are several factors that will limit the gain in resolution.

- **Drift :** A typical experiment requires 7500 to 15000 frames and takes 2-15 minutes depending on the exposure time. During the acquisition, the sample must be stationary with respect to the illumination pattern. Drift in the direction of the pattern is equivalent to changing the phase of the pattern by an unknown amount. All the frames need to be rearranged for SOFI processing based on their pattern orientation and phase. The drift contribution will appear as a spread of the phases for each substack, ultimately leading to a loss in pattern visibility. Only the drift in the direction perpendicular of the pattern can be compensated in a post-processing step.

- **Homogeneity of the phases :** SIM reconstruction algorithm expects the intensity variations between the phases to be due to the pattern phase shift. This assumption is challenged by the stochastic blinking required for SOFI, where the difference between two SOFI subsequences can be due to stochastic switching. To minimize this contradiction, dense labelling, high on-time ratio and long acquisitions are required.

- **Pattern SNR :** The resolution gain of n from the non-linear SIM reconstruction requires the successful unmixing of the nth order harmonic. However, the harmonic SNR decreases with the order, which limits the ability to unmix high order harmonics. To minimize this effect requires high contrast SIM pattern, dense sample and relatively long exposure time.

In summary, we need a densely labelled sample for homogeneous structure and visible pattern, high-power illumination, relatively long exposure time to maintain high SNR and no drift.

3.3.1   Experimental results

For this experiment, a 350mW 561nm continuous laser (gem 561, Laser Quantum) was coupled to a single mode fiber (55% coupling efficiency) and redirected at the input of the setup shown in Fig. 3.4. At maximum power, we have about $70mW$ reaching the sample, illuminating an area of about $75x75\mu m$ (maximum illumination power density of $1.2kW/cm^2$). The drift was minimized by leaving the sample on the microscope for 20-30 minutes prior to imaging.

We imaged the microtubule network of fixed COS-7 cells densely immunostained with primary anti-tubulin (1:50 dilution) and secondary donkey anti-mouse-AbberiorFlip565 antibody (1:50 dilution) with Abberior Flip self blinking dye in PBS buffer with 50% glycerol for longer ON-time using a water immersion objective ($60x$, NA = 1.2). We used 3 angles with 7 phases per angle, required to unmix third order SOFI images, and 700 frames per pattern (total of 14700 frames). We projected a pattern period of 460 nm and used an exposure time of 30 ms (+6 ms between each frame for camera eadout). The choice of the pattern period is based on the compromise between resolution gain and pattern contrast.

As already discussed, the homogeneity of the SIM phases is required for a successful reconstruction. The data acquisition can be carried out in two different ways. The first method (SOFI first then SIM) consists in projecting a fixed pattern for 500 to 1000 frames, then change the

phase or angle of the pattern and repeat the acquisition. This approach has the disadvantage to introduce inhomogeneous bleaching between each SIM images. The second method (SIM first then SOFI) consists in continuously changing the SIM pattern. This approach distribute the bleaching evenly but introduces a time lag proportional to the number SIM pattern between each SOFI frames. To minimize the bleaching artefacts, all the results shown have been obtained using the second acquisition method.

In theory, the reconstruction can also be carried out in two different ways. The first method consists in reconstructing the SIM for each frames and then computing SOFI. This approach has the disadvantage that it requires very fast exposure to record all the patterns faster than the On-time, which significantly reduces the raw SNR and leads to unreliable reconstruction. The second approach consists in computing SOFI on each subsequence and then compute SIM. This approach does not require fast exposure but requires a dense sample such that all the frames processed with SOFI shows the same structure. We note that the SOFI processing consists in computing the raw cross-cumulant and image flattening[66].

In summary, we found out that the optimal acquisition-processing pipeline was of the form SIM-SOFI for acquisition and SOFI-SIM for the reconstruction.
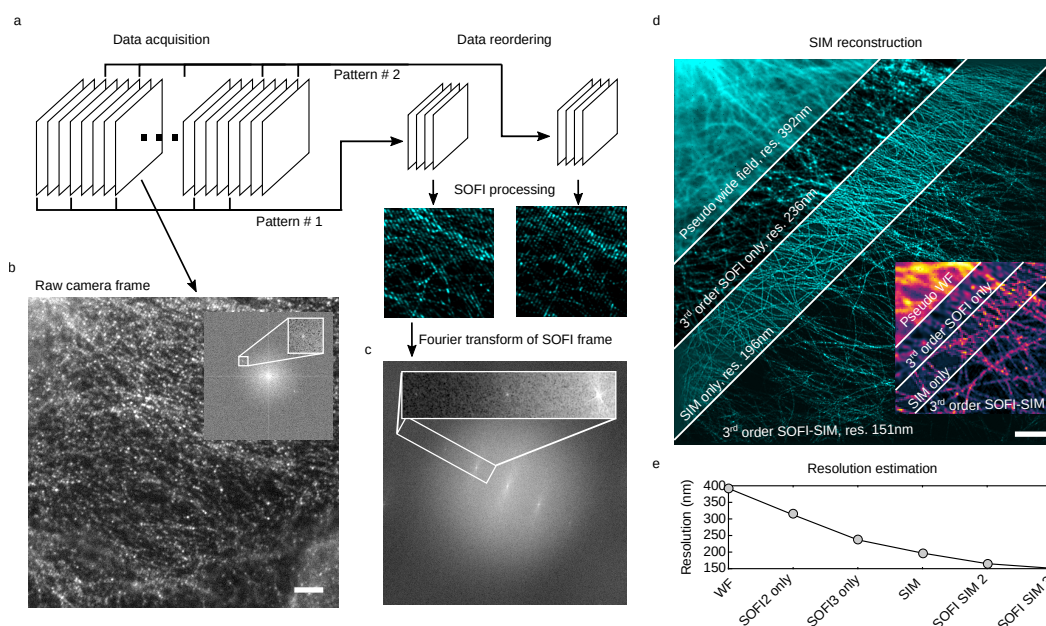
Figure 3.7 – Experimental realization of SOFI-SIM (a) Schematic of data acquisition, data reordering and SOFI processing on each patterns. (b) Raw camera frame. The Fourier transform of the frame is shown in inset. (c) Fourier transform of 3rd order raw SOFI frame, showing up to 3rd order non-linear peak. (d) SIM reconstruction and comparison of pseudo wide field (average of all the frames), 3rd order raw SOFI, SIM reconstruction on averaged pattern and 3rd order SOFI-SIM. (e) Resolution estimate as a function of the modality. Scale bar 5 μm

Fig. 3.7a shows the processing pipeline from the data acquisition, data reordering and grouping of the different pattern and phases for SOFI processing. Fig. 3.7b shows a raw camera

frame of dense labelling. The Fourier transform of the raw image is shown in inset, with easily identifiable structured illumination peak. Fig. 3.7c shows the Fourier transform of a 3rd order raw SOFI frame. The non-linearity of SOFI is visible in the presence of high-order peaks. Fig. 3.7d shows the resulting SIM reconstruction, compared with different modalities. The pseudo wide-field has been obtained by averaging all the frames and has a resolution[100] of 392 nm. The 3rd order raw SOFI was obtained by averaging all the patterns and computing SOFI. We estimate a resolution of about 236 nm. The SIM image was obtained by averaging all the frames with the same pattern and reconstructing the SIM image. We estimate a resolution of 196 nm. The two fold resolution improvement is consistent with the wide field resolution and illumination frequency. Finally, the 3rd order SOFI-SIM image shows a resolution of 151 nm.

From the theory and assuming infinity SNR, we expect a two fold resolution improvement compared to 3rd order raw SOFI, similar to the resolution improvement from wide-field to SIM. We therefore expect a 3rd order SOFI-SIM resolution of about 116 nm (236/2), which is not reached due to the low SNR of the 3rd order non-linear SIM peak. Each order provides a gain in resolution of about $116/3 \approx 39$ nm, and we have in this case $236 - 2*39 = 158$ nm. Presumably, the information carried out by the 3rd order peak is too close to the noise level to produce significant correlations.

Finally, Fig. 3.7e shows the estimated resolution as a function of the modality. As we can see, there is almost no improvement from SOFI-SIM2 (165 nm) to SOFI-SIM3 (151 nm). Even if it was possible to successfully compute higher order SOFI images, the reconstruction of high-frequency content will still be limited by the SNR.

3.3.2 Conclusion

We present the first experimental realization of the combination of SOFI with SIM. Although the results are promising, several options could be investigated to further improve the performances of the method, mainly by improving the signal to noise ratio.

Using a high NA TIRF objective and TIRF SIM would greatly improve the signal to noise ratio and minimize the out-of-focus signal. The pattern contrast could be maximized by implementing a polarization control scheme using a quarter-wave plate with a liquid crystal retarder. The implementation of an active drift correction would also be beneficial to the method. From the processing point-of-view, more advanced low-noise SIM reconstructions[102, 106] could be used.

4 Parameter-free resolution estimation

Super-resolution microscopy opened diverse new avenues of research by overcoming the resolution limit imposed by diffraction. Exploitation of the fluorescent emission of individual fluorophores made it possible to reveal structures beyond the diffraction limit. To accurately determine the resolution achieved during imaging is challenging with existing metrics. Here, we propose a method for assessing the resolution of individual super-resolved images based on image partial phase autocorrelation. The algorithm is model-free and does not require any user-defined parameters. We demonstrate its performance on a wide variety of imaging modalities, including diffraction-limited techniques. Finally, we show how our method can be used to optimize image acquisition and post-processing in super-resolution microscopy.

The following chapter is a reorganized version of the published manuscript

Descloux, A.C.[1], Grußmayer, K.S.[1] and Radenovic, A.[1], 2019. Parameter-free image resolution estimation based on decorrelation analysis. Nature methods, 16, pp.918-924.

[1]LBEN and LOB, EPFL, 1015 Lausanne, Switzerland

4.1   Introduction

Over the past decades, a broad range of novel imaging methods have emerged, providing unprecedented insights into sub-cellular structures[107, 108]. When designing a microscopy experiment, one should select an appropriate imaging modality taking into account the required spatio-temporal resolution. The image quality greatly varies among different techniques and is influenced by sample properties. Image formation can be modelled as the convolution of a ground-truth object with the specific point-spread function plus various method-related noise contributions. In Fourier space, the object spectrum is multiplied by the transfer function of the system. Its shape depends on the imaging method, but common to all techniques is image low-pass filtering, characterized by a cut-off frequency. This spatial frequency limit already known to Abbe[109] is generally expressed as $k_c = \text{NA}\frac{2\pi}{\lambda}$, where NA is the numerical aperture and λ the illumination central wavelength, and corresponds to the resolution in coherent imaging.

Super-resolution techniques overcome the diffraction limit by exploiting specific fluorophore properties such as stimulated emission or temporal fluctuations. Therefore, image resolution needs to be reconsidered by taking into account the fluorescent properties of the sample[110]. Ideally, this resolution criterion should work on a single image, be independent of the imaging method, have no user-dependent settings and be compatible with classical resolution. Such an estimator of resolution is of particular interest for autonomous adaptive microscopes[111, 112] that require robust tools to automatically achieve and maintain optimal performance in long-term imaging of biological samples.

In 1982, van Heel[113] and Saxton[114] independently proposed Fourier Ring Correlation (FRC) using two independent images of the same object for resolution estimation of electron microscopy images. The idea was quickly expanded to 3D via Fourier Shell Correlation by Harauz[115] and several threshold concepts have been proposed (0.5, 0.14310, 2σ [114–117], SSNR[118]) to extract a resolution measure. Later, Banterle[119] and Nieuwenhuizen[120] independently extended, reconsidered and applied the method to assess the resolution of single-molecule localization microscopy (SMLM) images. They define the cut-off frequency as the spatial frequency where the so-called FRC curve drops below 0.143.

In SMLM, the two image realizations are typically accomplished by splitting the localizations into two distinct subsets. In general, it can be achieved for any imaging technique[121] by acquiring two consecutive images under the same conditions. Maintaining these conditions may be difficult due to, e.g., bleaching or temporal fluctuations of the fluorescence signal. This is especially pertinent in live-cell imaging and significantly challenges the stationarity assumption of FRC.

Here, we propose a new method for resolution estimation based merely on an individual image without further requirements or a priori knowledge. The algorithm expects only a non-saturated, bandwidth-limited signal with adequate spatial sampling. This novel estimator is based on partial phase correlation and does not rely on any user-defined parameters. The algorithm is fast, uses only linear operations and enables the real-time objective assessment of

image resolution and Signal to Noise Ratio (SNR). We successfully applied our new approach on a variety of microscopy data sets, ranging from widefield imaging to SMLM and STED microscopy. We show that our estimator can also be used to optimize image resolution, both during experiments and throughout data post-processing.

4.2 Method

To achieve objective threshold-free resolution estimation, we introduce a processing method termed decorrelation analysis. The main algorithm is divided into two steps. First, the Fourier transform of the image is computed after standard edge apodization to suppress high-frequency artefacts. The Fourier transform is normalized as $I_n(k) = \frac{I(k)}{|I(k)|}$. The input image $I(k)$ and its normalized version $I_n(k)$ are then cross-correlated in Fourier space using Pearson correlation and condensed in a single value between 0 and 1 (Fig. 4.1a). Second, the operation is repeated, but the normalized Fourier transform is additionally filtered by a binary circular mask of radius $r \in [0, 1]$ expressed in normalized frequencies (Fig. 4.1b). By repeating the calculation, we compute $d(r)$ which is expressed as

$$d(r) = \frac{\iint \Re\{I(k) I_n^*(k) M(k; r)\} dk_x dk_y}{\sqrt{\iint |I(k)|^2 dk_x dk_y \iint |I_n(k) M(k; r)|^2 dk_x dk_y}} \tag{4.1}$$

where $k = [k_x, k_y]$ denotes Fourier space coordinates, $I(k)$ the Fourier transform of the input image, $I_n(k)$ the normalized Fourier transform and $M(k; r)$ the binary mask of radius r. For a detailed mathematical derivation and additional considerations, see section 4.2.1.

The core idea of the method is that by normalizing the Fourier transform of the input image, we balance the signal and noise contributions while the information of the object structure is preserved in the phase (the phase is responsible for organizing the constructive and destructive interferences of the complex exponentials to form the image, the amplitude plays only a minor role in this process). Taking a binary mask radius of 1 allows the extraction of the correlation value related to the original ratio of signal and noise. If we consider an image containing only white noise, we see that $d(r = 1) \approx 1$, since the white noise power spectrum is constant by definition (the normalization does not affect the signal). If we add a bandwidth-limited signal to the image, the correlation value for $r = 1$ will decrease (the normalization now has a direct effect on the added signal and thus $I_n(k)$ only partially correlates with $I(k)$).

By decreasing the radius of the mask ($r < 1$), we progressively remove the noise contribution but preserve the signal due to its bandwidth-limited nature. If the image contains only noise, the cross- correlation value will decrease linearly as a function of radius r. If we now add a signal, the decorrelation function $d(r)$ will exhibit a local maximum of amplitude A_0 that indicates the spatial frequency r_0 of best noise rejection and signal preservation ratio. Restricting the mask further removes more signal than noise, reducing the correlation below A_0 until it drops to 0 for $r = 0$. The position r_0 of the local maximum is therefore
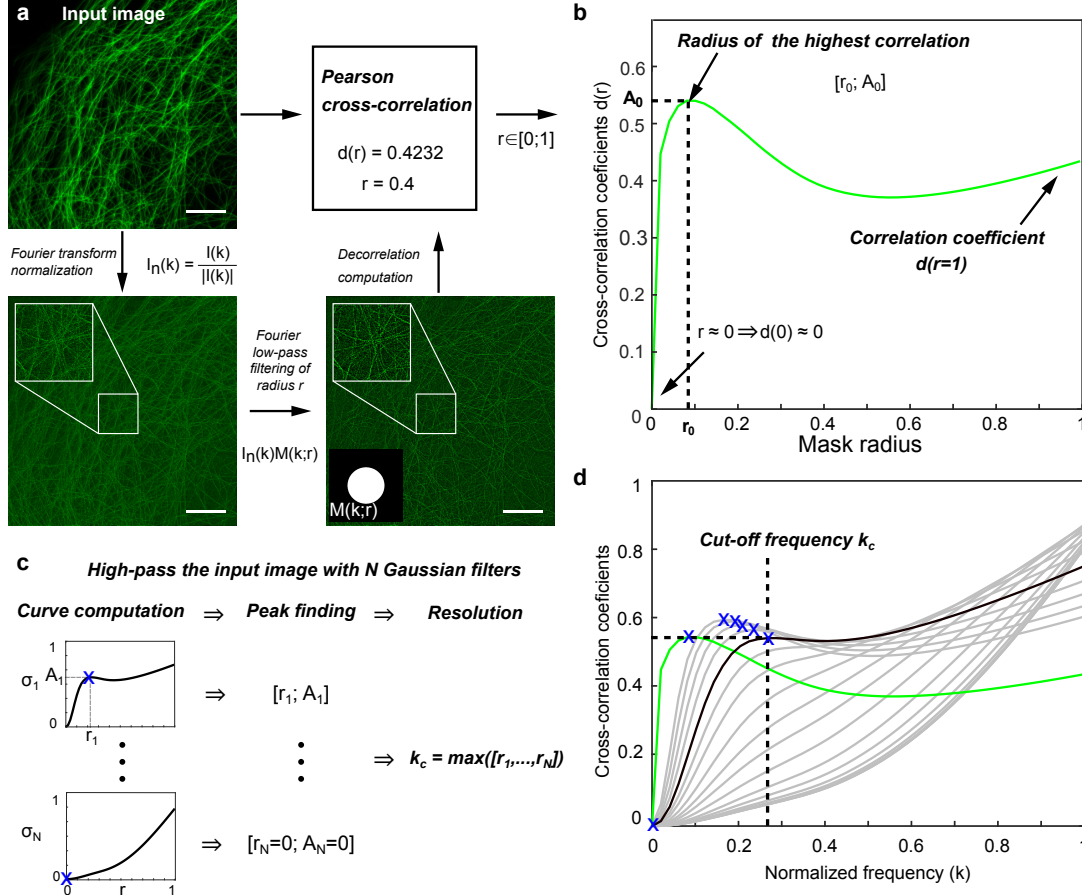
Figure 4.1 – Image decorrelation analysis workflow. (a) Cross-correlation of the image with its Fourier-filtered normalized version. (b) Cross-correlation coefficient as a function of the mask radius. (c) High-pass filtering of the input image and resolution estimation. (d) The plot of all decorrelation functions computed for the image and resolution estimation; Green: Decorrelation function without any high-pass filtering, Grey: Decorrelation functions with high-pass filtering, Blue cross : Local maxima, Black: decorrelation function of highest frequency peak, Vertical dashed line: cut-off frequency k_c. Scale bar, 5 μm.

directly related to the spatial frequency distribution of the image and its amplitude A_0 is positively correlated with the image SNR, however the use of A_0 as an SNR metric would require additional investigations. See section 4.2.1 for a detailed description of the algorithm and decorrelation function behaviour with respect to different noise statistics, aberrated transfer functions, cut-off frequencies, SNRs and high-pass filtering.

While being related to the spatial frequency content of the image, the position of the maximum does not directly indicate the resolution of the image. The input image is then subjected to a total of N_g high-pass filters (from weak to very strong filtering) to attenuate the energy of low frequencies. For each filtered image, a decorrelation function is computed and the peak position r_i and amplitude A_i are extracted, generating a set of $[r_i, A_i]$ pairs (Fig. 4.1c). If the

high-pass filtering removes too much signal, the decorrelation function will not exhibit a local maximum and the peak position and amplitude will both be set to 0. We investigated two strategies for resolution estimation (see section 4.2.3) and define the estimate as

$$k_c = max\left[r_0, \ldots, r_{N_g}\right] \qquad (4.2)$$

which corresponds to the local maximum of highest frequency (Fig. 4.1d). The resolution is then resolution $= \frac{2 \text{ pixel size}}{k_c}$, where k_c is expressed in normalized frequencies. By computing the resolution with varying sampling of $d(r)$ and varying number of high-pass filtering N_g, we confirm the robustness of the algorithm and estimate the precision to be ± 1 to 3 nm, independently of the type of image. Simulations of point emitters, MTFs, rings and crossing lines, corroborate that our resolution estimate depends linearly on the frequency support of the image and that the amplitude of the local maximum A_0 before any filtering is directly correlated with the image SNR.

Instead of searching for the frequency at which the transfer function vanishes (only possible in the absence of noise), we estimate the highest frequency from the local maxima of the decorrelation functions, enabling parameter-free image resolution estimation. The presented method does not estimate the theoretical resolution as stated by Abbe, but rather the highest frequency with high enough correlated signal with respect to the uncorrelated noise. It provides a rapid and objective way to quantify the frequency content of a single image without any user-defined parameter.

4.2.1 Mathematical framework- derivation of the analytical expression of the decorrelation function *d(r)*

We consider an incoherent imaging apparatus characterized by the ideal transfer function $H(k)$ of frequency support k_{th}

$$H(k) = \begin{cases} 1 - \frac{|k|}{k_{th}} & |k| < k_{th} \\ 0 & \text{otherwise} \end{cases} \qquad (4.3)$$

where $k = \sqrt{k_x^2 + k_y^2}$. We image an idealized point emitter of brightness A located on the optical axis. During the acquisition, the image is corrupted with pure white noise. The resulting intensity $I(k)$ is expressed in Fourier space, as

$$I(k) = A\left(1 - \frac{|k|}{k_{th}}\right)(|k| < k_{th}) + e^{i\theta(k)} \qquad (4.4)$$

where $\theta(k)$ is the random phase of the white noise.

The decorrelation analysis, i.e. the computation of the partial phase cross-correlation between the original image and its normalized version is expressed in Fourier space as

$$d(r) = \frac{\iint_{-\infty}^{\infty} \Re\left\{ I(k) \frac{I^*(k)}{|I(k)|} M(k;r) \right\} dk_x dk_y}{\sqrt{\iint_{-\infty}^{\infty} |I(k)|^2 dk_x dk_y \iint_{-\infty}^{\infty} \left| \frac{I(k)}{|I(k)|} M(k;r) \right|^2 dk_x dk_y}}$$ (4.5)

where $M(k;r)$ is a binary mask of radius r. The expression of the partial phase correlation in Fourier space allows us to make several general considerations. Using complex arithmetic, the numerator can be simplified as $I(k) \frac{I^*(k)}{|I(k)|} = |I(k)|$, while the denominator is composed of two terms. The first is simply the energy of the input image. This number does not depend on r and normalizes the function $d(r)$ between 0 and 1. Finally, due to the normalization, the last term is equal to the mask $\left| \frac{I(k)}{|I(k)|} M(k;r) \right|^2 = M(k;r)$.

Transforming equation 4.5 to polar coordinates $[k_x, k_y] => [k_r, \theta]$, we obtain

$$d(r) = \frac{\int_0^{2\pi} \int_0^1 |I(k)| M(k;r) k_r dk_r d\theta}{\sqrt{E \int_0^{2\pi} \int_0^1 M(k;r) k_r dk_r d\theta}}$$ (4.6)

where E stands for the energy of the input image (which is independent upon coordinate transform) and where we used the Cartesian-Polar transformation $dk_x dk_y = k_r dk_r d\theta$.

Using the simplified imaging model introduced above (equation 4.3), it is possible to analytically solve the expression for $d(r)$ and get a better understanding of how the function depends on the image transfer function.

We start with the numerator of equation 4.6 and use the fact that the mask $M(k;r)$ is 0 for $k_r > r$.

$$\int_0^{2\pi} \int_0^1 |I(k)| M(k;r) k_r dk_r 2d\theta = 2\pi \int_0^r \left| A\left(1 - \frac{|k|}{k_{th}}\right) (|k| < k_{th}) + e^{i\theta(k)} \right| k_r dk_r$$ (4.7)

In order to be able to integrate the noise term $e^{i\theta(k)}$ analytically, we make the additional assumption that the random phase fluctuations averages out under integration, which allows to approximate the expression 4.7 as the sum of the transfer function and the noise:

$$2\pi \int_0^r \left| A\left(1 - \frac{|k|}{k_{th}}\right) (|k| < k_{th}) + e^{i\theta(k)} \right| k_r dk_r \approx 2\pi \int_0^r A\left(1 - \frac{|k|}{k_{th}}\right) (|k| < k_{th}) k_r dk_r + \pi r^2$$ (4.8)

The remaining integration is trivial and we obtain for the numerator of equation 4.6

$$d_{num}(r) \approx \begin{cases} 2\pi A\left(\frac{r^2}{2} - \frac{r^3}{3k_{th}}\right) + \pi r^2 & \textit{for } r \leq k_{th} \\ \frac{\pi A}{3}k_{th}^2 + \pi r^2 & \textit{for } r > k_{th} \end{cases} \tag{4.9}$$

Using similar argumentation, we can express the signal energy E as

$$E = \pi\left[\frac{A^2 k_{th}^2}{6} + \frac{2A k_{th}^2}{3} + 1\right] \tag{4.10}$$

and the normalized denominator term of equation 4.6 as

$$\int_0^{2\pi}\int_0^1 M(k;r)\,k_r\,dk_r\,d\theta = \pi r^2 \tag{4.11}$$

Using equations 4.9, 4.10 and 4.11, we obtain for the decorrelation function $d(r)$ (for $r < k_{th}$)

$$d(r) = \frac{2\pi A\left(\frac{r^2}{2} - \frac{r^3}{3k_{th}}\right) + \pi r^2}{\sqrt{\pi\left[\frac{A^2 k_{th}^2}{6} + \frac{2A k_{th}^2}{3} + 1\right]\pi r^2}} \tag{4.12}$$

From equation 4.12, we clearly see that if $A \ll 1$, i.e. the signal is extremely weak compared to the noise, the decorrelation function becomes a line with a slope of 1.

$$d_{A\ll 1}(r) \approx \frac{\pi r^2}{\sqrt{\pi^2 r^2}} = r \tag{4.13}$$

We find the position of the local maxima by computing the partial derivative of the analytical expression of equation 4.12 with respect to r. We find

$$r_{max} = \frac{3k_{th}(A+1)}{4A} \tag{4.14}$$

We would like to note that the expression 4.14 is only valid for $r < k_{th}$ and that $r_{max} = k_{th}$ when $A = 3$. For this basic model, an amplitude below 3 will not yield any local maxima.

This result shows that, as long as the signal is strong enough, there is always a local maximum. Moreover, the position of the local maximum is directly connected to the cutoff frequency k_{th}.

Following our mathematical framework, in Fig. 4.2a , we calculate decorrelation function $d(r)$ with (orange, corresponds to equation 4.12) and without (blue) idealized noise as well as their corresponding transfer functions (orange and blue dashed lines). The position of the local maxima of the orange curve corresponds exactly to the analytical expression. We observe a deviation from the theoretical model when dealing with white noise. The fact that the maximum shifts to a lower frequency (and that its amplitude decreases) translates the degradation of the transfer function (the cutoff frequency is no more clearly identifiable).
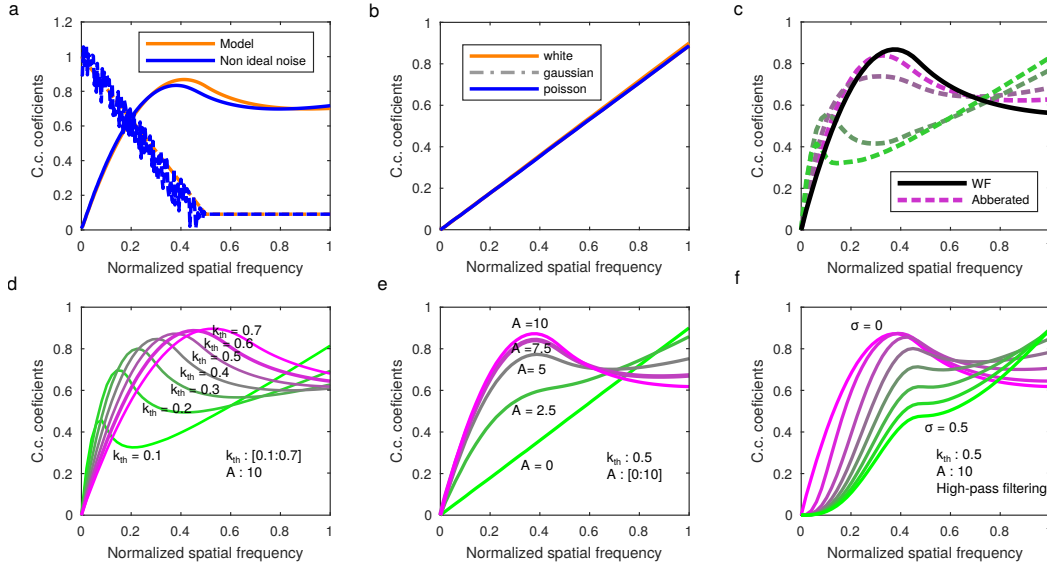

Figure 4.2 – Detailed behavior of decorrelation analysis. (a) Comparison of idealized vs non-ideal noise for the function $d(r)$ (solid lines) and radial average of the Transfer function (dashed line). (b)The plot of d(r) for three different noise statistics. (c) The plot of d(r) for aberration-free and aberrated point-spread function. (d) The plot of d(r) for fixed amplitude and varying cutoff. (e) The plot of d(r) for fixed cutoff and varying amplitude. (f)The plot of d(r) for various high-pass filtering of the input image.

We also show in Fig. 4.2b computation of $d(r)$ for various noise figures (white noise, Gaussian and Poisson). Here, we observe a very interesting feature of the algorithm. Spatially uncorrelated signal corresponds to a straight line, independently of the noise statistics. The fact that the functions are not equal to 1 for $r = 1$ is due to the fact that their power spectral densities are not perfectly flat.

We also illustrate in Fig. 4.2c, d and e, how $d(r)$ evolves as a function of aberrations, the cutoff frequency and the Signal-to-Noise ratio. For aberrations, we computed multiple transfer functions with a fixed cutoff ($k_{th} = 0.5$) and SNR ($A = 10$) and increased defocus by adding a circular symmetric quadratic phase $\left(e^{iWr^2}\right)$ to the pupil function, with W varying between 0 and 100. As expected, increases in defocus shifts the position of the maxima to the left. The decrease in the amplitude of the maximum is due to a decrease in SNR due to the spread of the point-spread function. A similar effect is seen when varying the cutoff frequency (Fig.

4.2d) from 0.7 to 0.1, where the position of the maximum follows the cutoff frequency. Again, the change in amplitude is due to the fact that the total energy of the signal decreases with the cutoff while the noise energy remains constant. On the contrary, when keeping the cutoff frequency fixed and changing the SNR via the parameter A, we observe that the position of the peak does not change until the signal is too weak to produce a peak. This corresponds to the limit of the method.

Finally, we show how $d(r)$ behave when the input image is filtered with a high-pass filter (in our case, we use a standard inverted Gaussian). As we increase the filtering strength, the position of the maximum shifts towards higher-frequencies. At some point we observe that too much signal has been removed from the image as no more peaks are observable. By filtering the input image, we are effectively modifying the transfer function in order to emphasize the high-frequencies. This provides a unique and robust way of estimating the resolution of the image based on the position of the peaks.

Due to the fact that the function is computed by integration over a disk of radius r, our analysis produces smooth and noiseless functions, without the need to apply any additional smoothing or any kind of fit. Two neighboring values $d(r)$ and $d(r+\Delta r)$ share a large amount of information. They are therefore naturally correlated and evolve slowly with respect to r.

4.2.2 Algorithm implementation

The following section describes the implementation of the method. The source code is publicly available on github (https://github.com/Ades91/ImDecorr.git) and is currently implemented in Matlab (CPU and GPU) and Java (CPU, as an ImageJ plugin, see Appendix B).

Pre-processing

We first compute the mean and subtract it from the image. We then apodize the edges by multiplying the image with a cosine window function defined as

$$W(x) = \begin{cases} \cos\left(k_x |x| + \varphi\right) & |x| \geq x_{max} - w \\ 1 & |x| < x_{max} - w \end{cases} \tag{4.15}$$

where $x \in [-x_{max}, x_{max}]$, x_{max} is half the field of view, w is the window length, $k_x = \frac{\pi}{w}$ and $\varphi = \pi - \frac{\pi}{w} x_{max}$. High frequency artefacts arising for edge discontinuities are consequently minimized. The image is then Fourier transformed and all values for $r > 1$, where r is the normalized radial frequency, are set to 0.

Initial decorrelation computation and peak finding

The initial decorrelation function $d(r)$ is computed according to equation 4.1. For speed

consideration, the computation is performed in Fourier space as

$$d(r) = \frac{\sum\sum_{k_x,k_y} \Re\left\{I(k_x,k_y)M(r)I_n(k_x,k_y)^*\right\}}{\sqrt{\sum\sum_{k_x,k_y}\left|M(r)I_n(k_x,k_y)\right|^2 \sum\sum_{k_x,k_y}\left|I(k_x,k_y)\right|^2}}$$ (4.16)

As discussed in section 4.2.1, the function $d(r)$ has a local maximum which we need to locate. This is a very general signal processing task and many solutions exist. In our case, the decorrelation function always exhibit a highly specific shape where it is equal to 0 for $r = 0$, raises to a certain value based on the SNR and decreases as it decorrelates. Using our knowledge of the shape of $d(r)$, we propose the following strategy for determining the local maxima.

We pick the maximum of $d(r)$. If the position of the picked maximum is the last value of the array, this means that either the tail of $d(r)$ is larger than the local maximum or there is no local maximum. In both cases, we exclude the value from the array and repeat the operation with the remaining values. We stop the loop as soon as we find a maximum that is not the last element of the array (local maximum exists) or if we run out of values (no local maxima at all). By processing a significant amount of simulated and experimental images, we concluded that our strategy for localizing the local maximum of any decorrelation function was robust enough and that we did not need to implement more sophisticated approach.

In order to avoid the selection of noisy local maxima (very rarely arising when analyzing post-processed or poorly sampled images), we also impose that the local maximum should be at least 0.001 larger than the smallest value from the position of the maximum to the last value of the array. We point out the fact that, unlike the Fourier Ring Correlation or Power Spectral Density threshold, it cannot be used to tune the resolution as it works only as a rejection criterion and is only useful in very specific situations rather than being mandatory.

The average image SNR estimate is set as $A_0 = d(r_0)$ and the position of the local maximum of r_0 is used as a first guess for the spatial frequency content, useful for the following high-pass refinement steps (Fig. 4.1c).

High-pass filtering and resolution estimation

In order to find the highest significant frequency, the input image has to be high-pass filtered in a smooth way, in order to weaken low frequencies contributions. Here we propose the use of Gaussian filtering. In both Matlab and ImageJ implementation, this operation is performed in real space (conveniently using B = imgaussfilt(A) for Matlab or the GaussianBlur() class for ImageJ). This operation could also be implemented in Fourier space for processing speed optimization. We obtain the high-pass filtered version of the image I as:

$$I_{HP}(x) = I(x) - I_{LP}(x;\sigma)$$ (4.17)

where $I_{LP}(x; \sigma)$ is the low-pass version of the image with a σ.

In the current implementation, we propose to compute N_g (typically 10) high-pass version of the input image with $\sigma_i = e^{\frac{i}{N_g}\left(\log\left(\frac{2}{r_0}\right) - \log(0.15)\right) + \log(0.15)}$. Each σ is then exponentially distributed between $\frac{2}{r_0}$ (weak high-pass) and 0.15 (very strong high-pass) where r_0 is expressed in pixels units. For each high-pass filtered image, a corresponding decorrelation function is computed and the local maximum position and amplitude are extracted $[r_i, A_i]$.

We then get the highest frequency peak and the largest geometric mean from all peaks.

The σ_B corresponding to the "best" curve is identified for both criterion and the whole procedure is repeated with refined high-pass filtering distributed between $min\left(\sigma_{B,gm}, \sigma_{B,max}\right)$ and $max\left(\sigma_{B+1,gm}, \sigma_{B+1,max}\right)$.

While it is not the fastest implementation (more advanced method could be used to improve the convergence and minimize the number of correlations to be computed), it guarantees a result in a fixed and reasonable computation time (typical processing speeds are ranging from 1 to 15 seconds depending on the implementation, the size of the image and the number of points N_r and N_g used for the computation).

The image resolution is then defined as resolution $= \frac{2 \text{ pixel size}}{k_c}$, where $k_c = \max\limits_{i=[1,N_g]} r_i$ is expressed in $[1/\mu m]$.

4.2.3 Resolution criterion, frequency sampling and error estimation

So far, we have introduced a way to process an image to extract several curves that exhibit a local maximum directly linked to the spatial frequency content of the image. The remaining operation consists of selecting the most suitable peak to be our resolution estimator. We consider the two most natural choices that are: the peak corresponding to the highest frequency $\left(k_{c,m} = \max\limits_{i=[1,N_g]} r_i\right)$ or the peak corresponding to the highest geometrical mean $\left(k_{c,GM} = r_i \mid \max\limits_{i=[1,N_g]} \sqrt{r_i A_i}\right)$ (giving the same amount of weight to the amplitude of the peak, i.e. SNR, and the spatial frequency).

We conducted a large study, computing the resolution using both criteria, with a varying sampling of $d(r)$ (N_r = [30:100] in steps of 10) and different numbers of high-pass filtering (N_g = [10:30] in steps of 5). Fig. 4.3a displays the STED image used to show how the resolution estimated from the highest frequency $\left(k_{c,m}\right)$ changes with respect to Nr and Ng.

Fig. 4.3b shows the resolution estimate using the maximum frequency criterion $res = 2/k_{c,m}$, where $k_{c,m}$ is expressed in [1/um] as a function of N_r and N_r. Using the geometric mean criterion, we measure an average resolution of $113nm$ and a precision of $\pm 1.8nm$ (not shown here) and $113 \pm 1.3nm$ using the maximum frequency (see Fig. 4.3b). This demonstrates the robustness of the method to large changes in processing parameters and the absence of bias
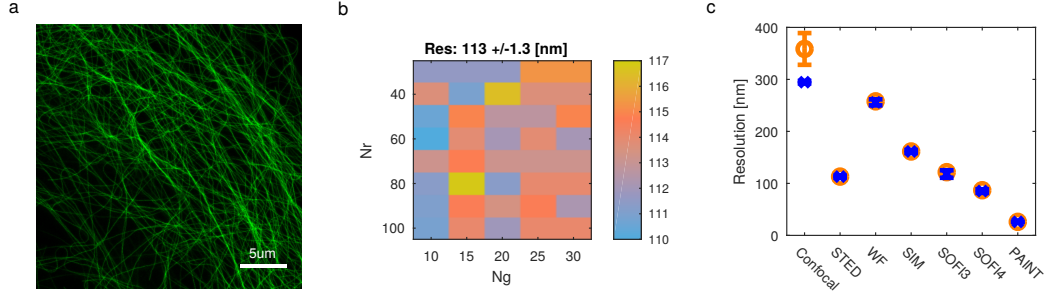
Figure 4.3 – esolution estimate and criterion vs N_r and N_g. (a) STED image used as an example for (b). (b) Estimated resolution of (a) as a function of N_r and N_g, with an average and standard deviation of 113 ± 1.3nm . (c) Resolution estimate average and standard deviation (n=40) for different modalities and the two resolution criteria: geometric mean (orange circles) and highest frequency (blue crosses). (Confocal: Fig. 4.11a, STED: Fig. 4.11c, WF: Fig. 4.14a, SIM: Fig. 4.14c, SOFI3-4: Fig. 4.17a and PAINT: Fig. 4.18f).

introduced by the choice of the parameters. Fig. 4.3c shows the same comparison for different imaging modalities presented in Fig. 4.11,4.14,4.18). Besides for confocal data, there is no significant difference between the estimated resolution using the geometric mean (orange circles) or the maximum frequency (blue crosses) criteria and the precision is typically $\pm 3nm$ or less. The reason why the confocal data has a different behavior is linked to the shape of its transfer function and can be directly seen in Fig. 4.11. The amplitude of the peaks drops very quickly for a small increase in spatial frequency. This is due to the fact that confocal transfer function has a quadratic decrease in amplitude as a function of spatial frequency. Therefore, the criterion that includes SNR is more likely to be conservative when estimating the resolution.

Unless specified otherwise, all resolutions and cutoff frequencies shown in the manuscript are calculated using the highest frequency criterion.

4.3 Simulations

Point emitters

To validate the ability of the proposed analysis in estimating the resolution and Signal-to-Noise Ratio (SNR), we performed additional simulations. The simulated object consists in a random distribution of point emitters, contributing incoherently to the image intensity. The image SNR is controlled by the amplitude of the incoherent point spread function and the resolution is controlled by the extent of the transfer function $H(k)$. We then compute several images with a cutoff frequency ranging from 0 to 0.8. The incoherent transfer function $H(k)$

can be expressed as

$$H(k) = \begin{cases} A\left(1 - \frac{|k|}{k_{th}}\right) & |k| < k_{th} \\ 0 & otherwise \end{cases} \tag{4.18}$$

where k_{th} is the theoretical cutoff frequency and A controls the amplitude of the transfer function. The noise level is controlled by Gaussian additive noise of statistic 100+/-2 counts (corresponding to averaged dark frames statistics of a Hamamatsu Orca Flash V4.0) and additional Poisson noise.

Consequently, we can attribute to each simulated image a theoretical resolution k_{th} and a signal to noise ratio $SNR = \frac{\mu_{sig}}{\sigma_{noise}} = \frac{<I(x)>-100}{2}$. We then vary the image resolution over the range $k_{th} = [0, 0.8]$ and the image SNR over $SNR = [0, 500]$ (via adequate tuning of A).

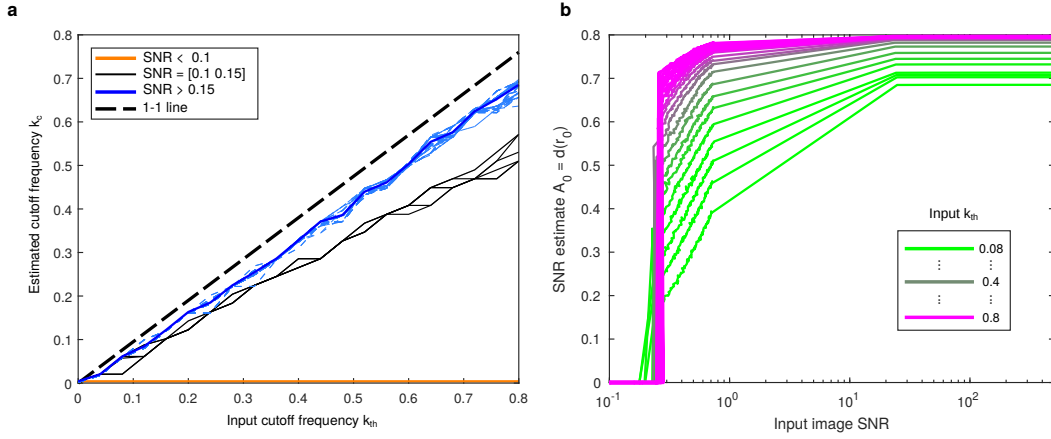Figure 4.4 – Simulations (a) Estimated cutoff frequency vs simulated NA for various image SNR (Orange line: SNR < 0.1, Solid black lines: SNR between [0.1 and 0.15], Solid blue line: SNR > 0.15 (average of dashed blue lines), Dashed black line: 1-1 reference line). (b) The amplitude of the initial decorrelation function vs simulated image SNR for various normalized cutoff frequency.

Our algorithm exhibits (Fig. 4.4a) a linear dependency with the simulated cutoff k_{th}, with an offset of about 10% when the image SNR is above ≈ 0.15. $H(k)$ drops to 0 at the frequency k_{th}. In the case of lower SNR, this frequency cannot be reliably estimated. For an image SNR between 0.1 and 0.15, the algorithm recovers a lower resolution, which is consistent when considering low SNR images where the transfer function is partially embedded in the noise. Images with a SNR smaller than 0.1 do not exhibit any peaks in the analysis.

Fig. SR1.1b shows the amplitude A_0 of the peak of the original decorrelation function without any high-pass filtering. While the cutoff frequency estimate is independent of the image SNR (in the high SNR case), we see that our SNR estimator depends on both the input image SNR and the cutoff frequency. This is due to the fact that, in our simulation, we are keeping the

amplitude of the transfer function $H(k)$ constant as a function of the cutoff frequency k_{th}. This means that the signal energy (that is the volume under the surface defined by $H(k)$) decreases with the cutoff. Since we are keeping the noise energy constant, the SNR decreases with reduced cutoff, which is what we observe. A detailed plot of the functions is shown in Fig. 4.2d.

The modulation transfer function (MTF)

One of the important tools by which image resolution is measured is the Modulation Transfer Function (MTF). This object consists of a series of parallel lines with progressively decreased spacing. As the lines get closer, the line modulation contrast $\left(M = \frac{I_{max} - I_{min}}{I_{max} + I_{min}} \right)$ drops to 0.
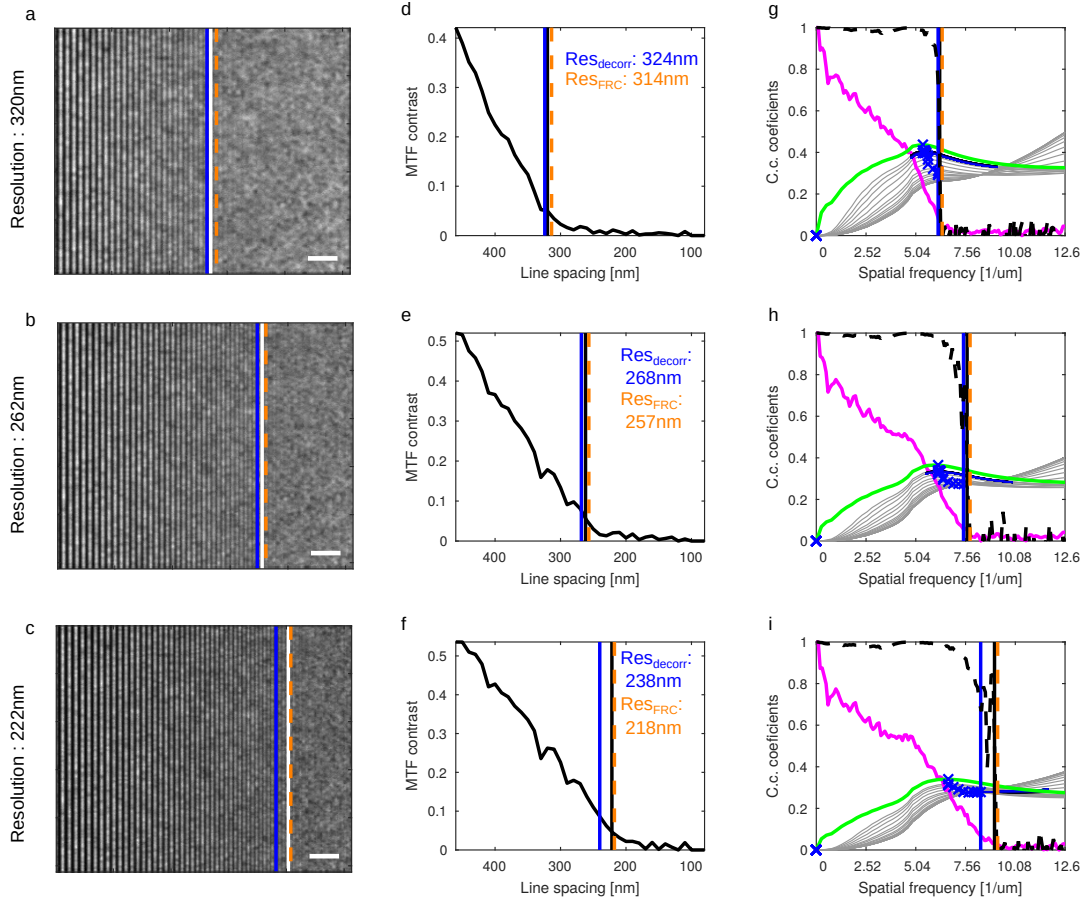
Figure 4.5 – MTF simulations and resolution estimation (a-c) Simulated MTF for 3 different resolutions (Blue line: max. resolution, Orange dashed line: FRC resolution, White line: Input resolution), Scale bar: 2um. (d-f) MTF curves extracted from (a-c). (g-i) Decorrelation analysis of (a-c) (Magenta line: Radial average of log of abs of the Fourier transform of (a-c), Green line: d0, Gray lines: all high-pass version of d, Black dashed line: FRC curve, Vertical blue line: estimated resolution, Orange dashed line: FRC resolution, Vertical black line: input resolution). Scale bar: 2μm.

We simulated a widefield image of a dense (about 500 emitters per μm^2 in average) distribution of point emitters forming an MTF pattern. We have a FOV of 20μm and started with a period of 460nm up to 80nm, decreasing in steps of 10nm. Each period is repeated two times. Each point emitter contributes incoherently to the image intensity. We show in Fig. 4.5 (a-c) three MTF images of varying resolution ($res = \frac{\lambda}{2\text{NA}}$, 320, 262 and 222nm, corresponding to a NA of respectively 0.9, 1.1 and 1.3 for a wavelength of 576nm). The blue line denotes the estimated resolution and the white line the theoretical resolution. The FRC resolution (314, 257 and 218nm), obtained by computing the second image in identical conditions, is shown as an orange dashed line and is slightly over-estimating the theoretical resolution. We then compute MTF curves (Fig. 4.5d-f) by averaging along the direction perpendicular to the pattern and selecting adequate sub-windows for contrast computation. Again, we indicate the estimated resolution (blue line) and the theoretical resolution (black line). Fig. 4.5 (g-i) shows the results of the decorrelation analysis.

Ring and sparse lines structures
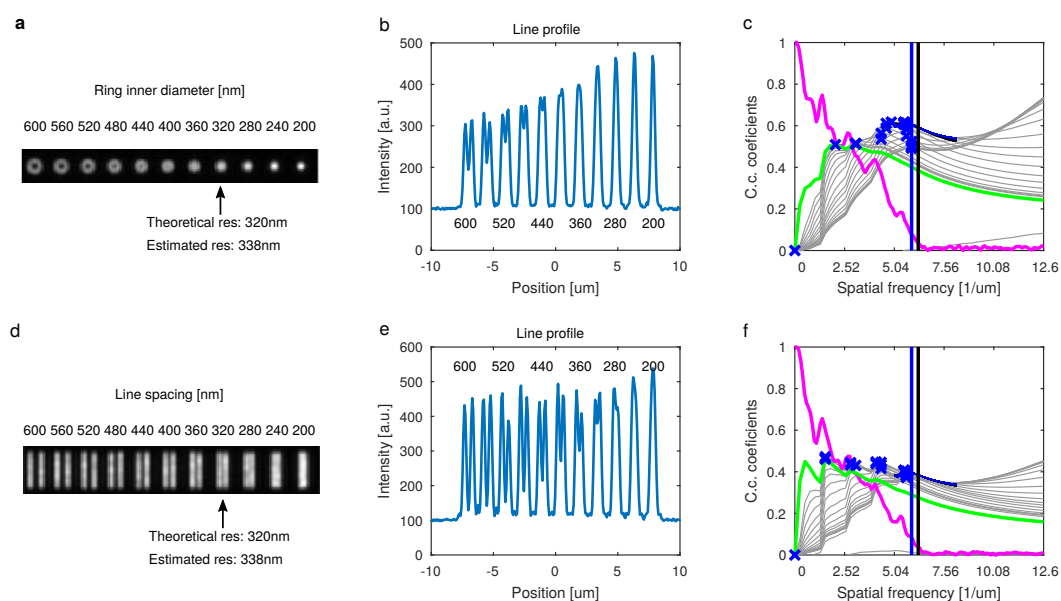
Figure 4.6 – Test objects in simulations. (a) The simulated intensity of ring structures (inner diameter of 600 to 200nm in steps of 40nm) with an input resolution of 320nm. (b) The line profile showing the decreases of the contrast in the ring centers. (c) Decorrelation analysis with an estimated resolution of 338nm. (d) The simulated intensity of sparse line structures with similar spacing and conditions. (e) The line profile showing the decreases of contrast with decreased spacing. (f) Corresponding decorrelation analysis with an estimated resolution of 338nm. Scale bar: 2μm.

We also simulated ring structures with an inner diameter ranging from 600 to 200nm and a width of 30nm. We set the theoretical resolution to be equal to the inner diameter of a ring. Each ring is constituted of 1000 molecules, resulting in about 10'000 to 40'000 emitters per

μm^2.

We show in Fig. 4.6a the resulting image. Interestingly, the ring with an inner diameter equal to the theoretical resolution cannot be resolved. This is due to the shape of the structure. The contribution of all the emitters actually decreases the contrast of the dip. This means that to be able to resolve a ring, one needs to have a resolution of a least two times the inner diameter. To confirm this effect, we show in Fig. 4.6d-f sparse line structures with similar spacing as the rings, simulated under the exact same conditions. The lines with a spacing equal to the resolution are this time resolved. By computing another image, we measure an FRC resolution of 316nm.

Crossing lines

Finally, we simulated crossing lines (Fig. 4.7a-c) as another structure of interest to quantify the validity of our resolution estimator. The structure consists in two 30nm width and 10μm long lines crossing each other with an angle of 5°. Each line is made of 6000 randomly distributed emitters.
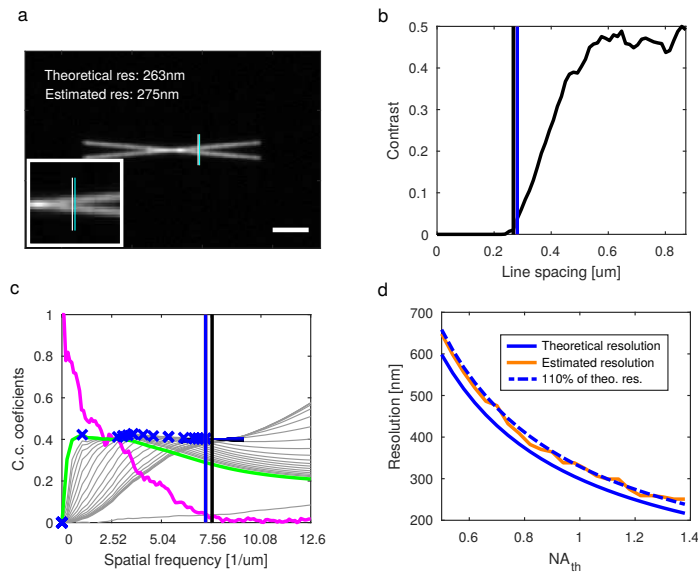
Figure 4.7 – Decorrelation resolution estimation for crossing lines. (a) The simulated intensity of crossing lines with a theoretical resolution of 263nm and an estimated resolution of 275nm. The white and blue vertical lines indicate the position where the spacing between the two crossing lines is equal to the theoretical resolution (white line) and the estimated resolution (cyan line). (b) Contrast as a function of line spacing (Black line: Theoretical resolution, Blue line: Estimated resolution). (c) Corresponding decorrelation analysis with an estimated resolution of 275nm. (d) Resolution estimation for a theoretical NA ranging from 0.5 to 1.4 (Solid blue line: Theoretical resolution, Orange line: Estimated resolution, Dashed blue line: 110% of theoretical resolution). Scale bar: 2μm.

With a theoretical resolution of 263nm, the algorithm independently estimated a resolution of 275nm, which is consistent with all the other simulations and what is expected from the theory. We repeated the simulation and changed the input numerical aperture from 0.5 to 1.4 NA (Fig. 4.7d). The estimated resolution (orange curve) follows precisely the theoretical resolution (solid blue curve). We also notice that, similar to the results obtained in Section 4.3, the estimated resolution is equal to about 1.1 times the resolution as defined by Abbe. Our resolution estimator does not exhibit any structure dependent bias. By computing another image, we measure an FRC resolution of 256nm.

4.4 Experimental results

4.4.1 GATAquant nanorulers

Due to their high reproducibility and nanometric accuracy, DNA origami have been proposed as calibration standards for resolution measurement in classical and super-resolution microscopy[122]. To demonstrate the validity and broad applicability of the method, we processed DNA origami nanorulers images with different geometries[123] kindly provided by GATTAquant (courtesy of P. Tinnefeld and J. Schmied). The resolutions estimated by our algorithm are smaller than the mark-to-mark distances of the nanorulers, which corroborates the fact that they are resolved in all imaging modalities.

For the PAINT dataset (see Fig. 4.8), we localized 10 molecules, co-aligned them and averaged them to get the resolution estimate. Particle-averaging methods widely used in *cryo-electron microscopy*, have been also adopted by researchers using SMLM . For example, several labs, working with hightroughput SMLM setups used, particle averging to elucidate labeled protein organization in structures such as of the nuclear pore complex[124] and centrioles[125]. We also computed the resolution over the whole field of view and obtained a resolution of 32nm using FRC and 45nm using our method. The difference between the particle averaged resolution and the whole FOV resolution can be attributed to sub-optimal co-alignment.
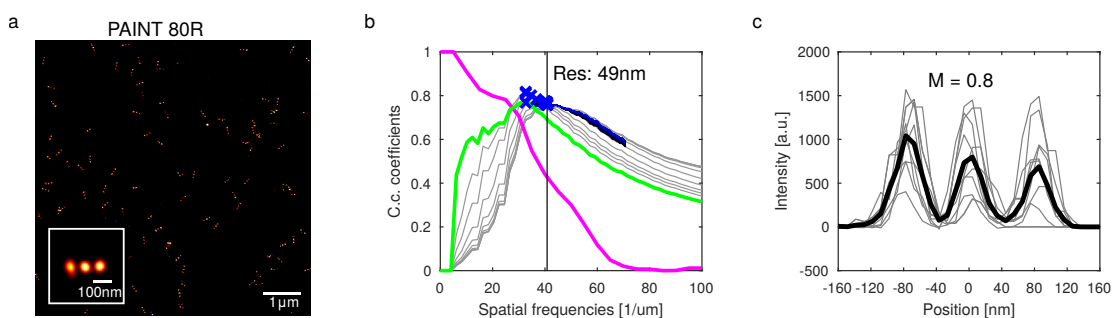

Figure 4.8 – GATTAquant nanorulers and resolution estimate for PAINT microscopy. (a) PAINT image of nanoruler (inset: Average of 10 manually localized and co-aligned molecules). (b) Decorrelation analysis performed on the averaged image. (c) Line profile of inset of (a) and modulation contrast M.
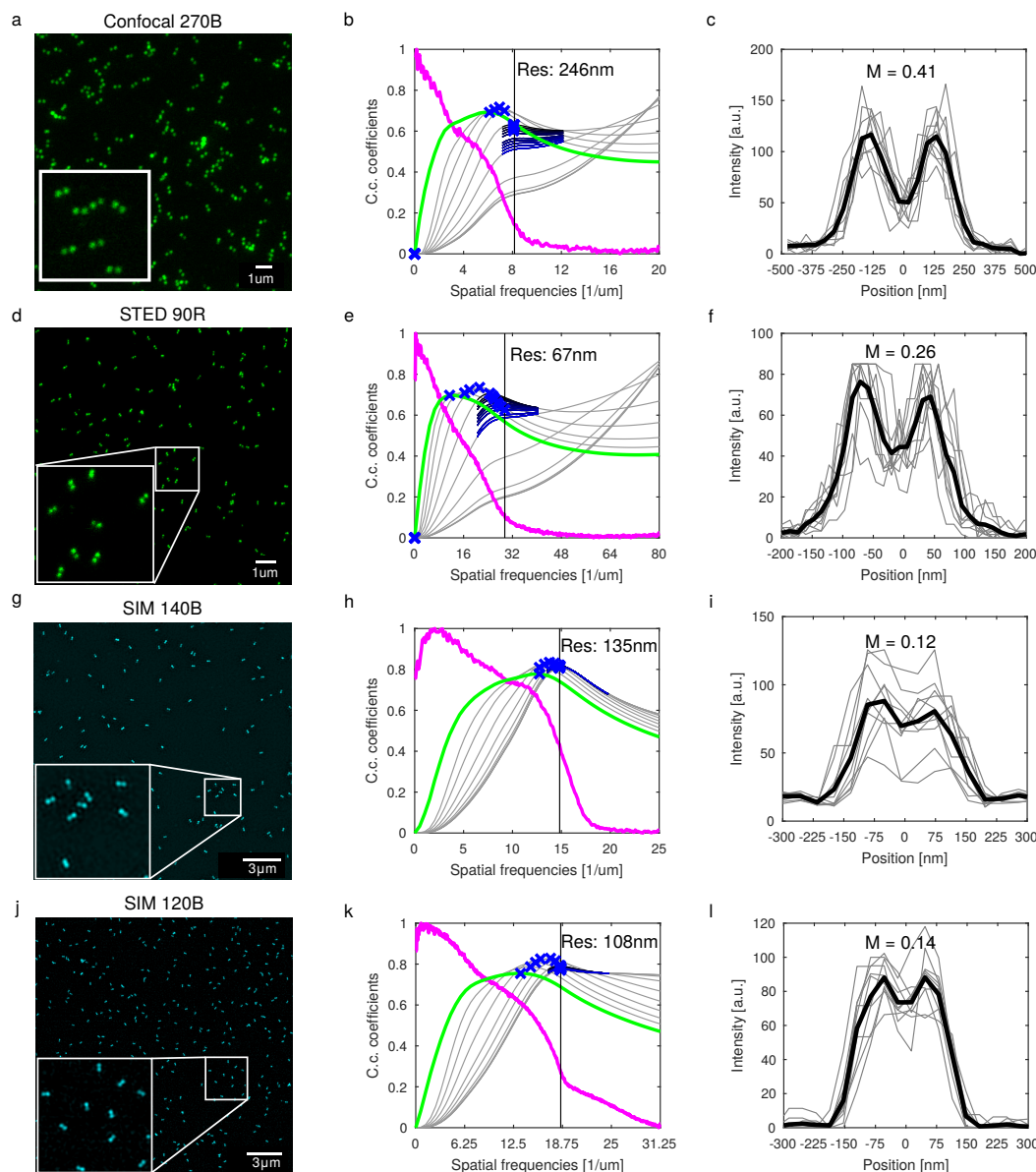
Figure 4.9 – Figure SR2.1: GATTAquant nanorulers and resolution estimate. (a-c) Confocal imaging. (d-f) STED imaging. (g-l) SIM imaging. (Left column) GATTAquant nanorulers images. Nanoruler type is indicated above the image, the number indicates the mark-to-mark distance in nm. (Middle column) Corresponding decorrelation analysis and resulting resolution. (Right column) Average (black line) lines profiles of 10 (gray lines) individual molecules and modulation contrast M.

In order to demonstrate the validity and robustness of our method, we processed several datasets nanorulers directly provided by GATTAquant (Fig. 4.9 a,d,g,j). Independently of the modality, the resolution estimate (Fig. 4.9 b,e,h,k) is in perfect agreement with the samples

specifications and manually selected line profiles (Fig. 4.9 c,f,i,l). We see that when the structure is properly resolved, as it is the case for confocal, STED and PAINT images, the resolution estimate is significantly smaller than the nanoruler size. For the two SIM images, the resolution estimate is much closer to the DNA origami size, which is consistent with the line profiles and contrast measurement, where the structure can barely be resolved.

4.4.2 Fluorescent beads resolution

A typical way to assess the performance of a microscope is to image a single layer of fluorescent monodispersed beads. If the beads are sufficiently smaller than the system point-spread function and if the beads are well separated, a fit of the beads image can provide a good estimate of the microscope resolution in idealized conditions.

Here we demonstrate how our method performs on a technical sample (Tetraspeck beads, 175 nm). Two large z-scan (10μm, steps of 25nm) were acquired (Fig. 4.10, a-d), with 488 and 635nm excitation. As it can be seen, most of the beads formed clusters. This sample is therefore not suitable for fitting. Each frames were then processed with our algorithm to estimate the cutoff frequency.
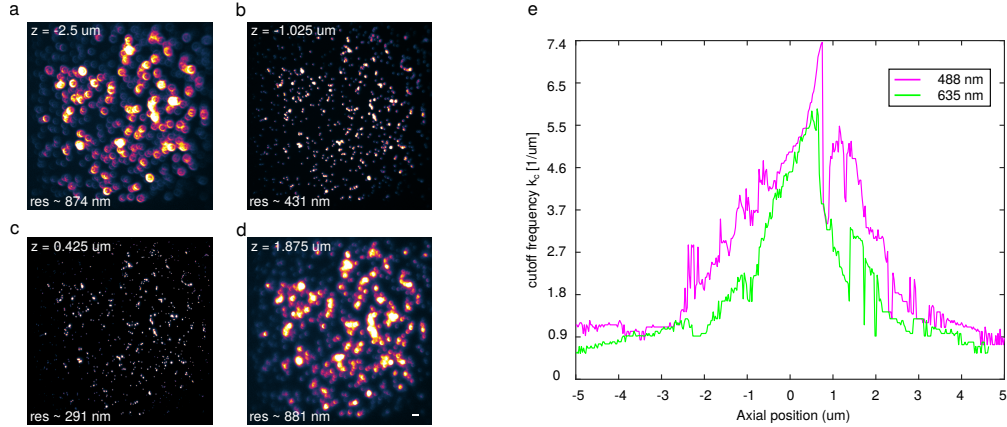
Figure 4.10 – Resolution of fluorescent beads. (a-d) Images of Tetraspeck beads excited with 488nm excitation laser line at various axial positions. (e) Cutoff frequency estimate as function of the defocus for 488 (magenta) and 635nm (green) excitation. Scale bar 5 μm.

Fig. 4.10e shows how the cutoff frequency evolves through the z-scanning. As expected, the 488 excitation leads to an overall better resolution, independently of the z-position.

We measure the lowest resolution of 332nm with 640nm excitation and 276nm with 488 nm. Considering the size of the beads (175nm, which cannot be considered to be an ideal point emitter), the excitation wavelength and the objective NA (Nikon super-resolution water immersion 1.27NA), we can approximate the expected resolution as Res_{640} $\sqrt{256^2 + 175^2} = 310nm$ and Res_{488} $\sqrt{196^2 + 175^2} = 262nm$. Both measurements show good agreement with

the theoretical value.

We observe the expected resolution is reached, but only on a very narrow 200nm range. The asymmetry of the cutoff as a function of z shown in Fig. 4.10e reflect the asymmetry of the point-spread function. Consequently, we propose our method as a practical way to test the performance of an objective lens and the alignment of a microscopy setup.

4.4.3 Confocal and STED

Confocal[126] and Stimulated Emission Depletion (STED) microscopy[23, 127] are point-scanning techniques that can be realized on the same setup, allowing the transition from diffraction-limited to super-resolution imaging. STED microscopy is a super-resolution method that uses confocal illumination for excitation and a donut-shaped depletion beam to de-excite the surrounding fluorophores prior to fluorescence emission. The resolution of STED microscopy for a given fluorophore depends on the spatial and temporal co-alignment of the two beams[128], the shape, and the quality of the depletion beam and its power[129].

Using a commercial state-of-the-art microscope, we imaged the microtubule network of COS-7 cells both in confocal and pulsed STED mode. Fig. 4.11a-d show the resulting images and their corresponding decorrelation analysis.

As expected, all decorrelation functions exhibit a local maximum, with STED showing a 2.52-fold resolution improvement over confocal imaging. We plotted in Fig. 4.11c the manually selected line profile of a microtubule cross-section, a method typically used to estimate the resolution. The measured FWHMs are in good agreement with our estimates.

Fig. 4.11e and f show the result of the analysis performed on a time series of eight consecutive STED images. As expected, repeated imaging of the same structure gradually bleaches the fluorophores, progressively degrading the SNR as indicated by the parameter A_0 . We also observe a consistent deterioration of the resolution until the 7th frame, where we reach a resolution close to confocal imaging. The bleaching is so strong that the structure is no longer continuous. The proposed method confirms the expected degradation of image resolution and provides an estimate of the image SNR and resolution (see 4.12). Fig. 4.11g and h illustrate how our resolution estimation can be used to optimize STED imaging. Imaging under several STED illumination powers was performed, adjusting the excitation power to maintain the optimal dynamic range of the image to avoid noise-limitation of STED resolution15. Using 20% STED laser power has a significant improvement on the resolution (2.4 fold) but further doubling the power only decreases the resolution by a factor of 1.1 as expected due to the non-linear behaviour of STED. Further increases in STED power do not lead to significant changes in resolution, possibly due to misalignment of the excitation and STED beam, imperfect "zero" of the STED doughnut as well as excess photo-bleaching and background induced by the STED beam[127]. We conducted additional experiments, investigating more acquisition parameters such as the STED delay, pixel size and comparing the performance of different dyes to choose the optimal label (see 4.13). Our algorithm provides a direct and straightforward estimation
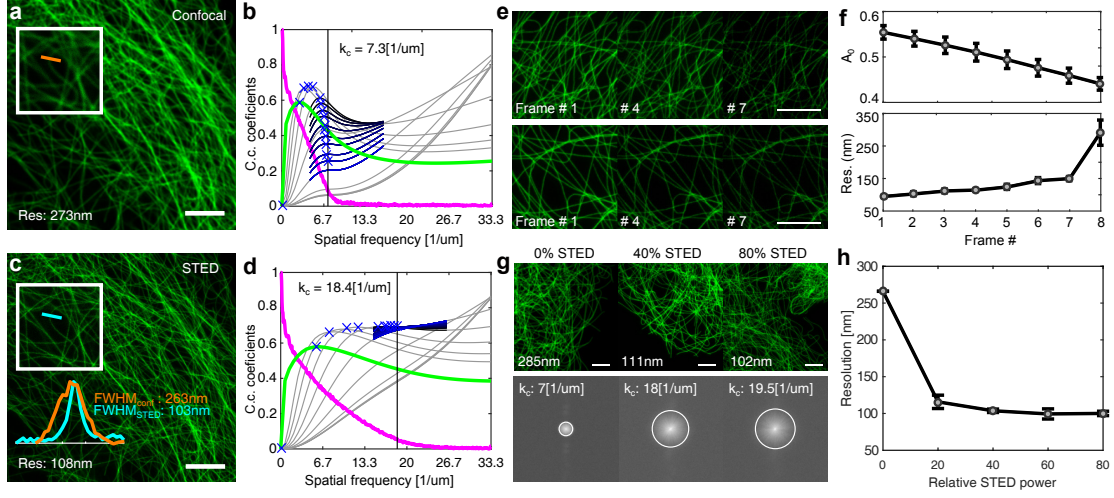
Figure 4.11 – Confocal and STED. All images show microtubules in fixed COS-7 cells immuno-labeled with Abberior Star 635P. (a) Confocal image and (b) its corresponding decorrelation analysis. Green line: decorrelation functions before high-pass filtering. Magenta line: Radial average of log of absolute value of Fourier transform of (a). Gray lines: all high-pass filtered decorrelation functions. Blue to Black lines: decorrelation functions with refined mask radius and high-pass filtering range. Blue crosses: all local maxima. Dashed vertical line : cut-off k_c (for the sake of readability, we used the same color and style representation for all the subsequent analysis). (c) STED image of the same structure as in (a) with line profile of selected microtubule and (d) its corresponding decorrelation analysis. (e) Sequential STED imaging of two different cells (f) SNR estimator and resolution (average and standard deviation) of a total of 4 STED sequences of different cells as a function of time. (g) STED images as a function of STED power. The lower panel shows the corresponding Fourier space with indicated cut-off frequency. (h) Resolution as a function of STED power (average and standard deviation of 5 images of different cells per STED power). Scale bar, 5 μm.

of image resolution to objectively find the best acquisition settings and optimize sample preparation, based on a single image of the sample of interest without imposing additional requirements on the data acquisition scheme. In principle, it should be possible to use our resolution estimate to tune the microscope alignment, e.g. to adjust the overlap of the STED donut with the confocal excitation spot.

Fig. 4.12a shows the evolution of the non-filtered decorrelation function d_0 used for SNR estimation for the STED data in Fig. 4.11e-f. We clearly see that as the frame number increases (magenta to green), the peak amplitude drops. If we continued the imaging, the peak would have eventually vanished as the function will tend towards a straight line. Figure 4.12b-f shows the full decorrelation analysis of STED for 5 different relative depletion powers for Fig. 4.11g-h. We see that at 0%, the resolution is that of a normal confocal. As we increase the STED power, the resolution improves as expected. We observe no significant improvement in resolution between 60 and 80%. The ideal relative STED power is then estimated between 40 and 60%.
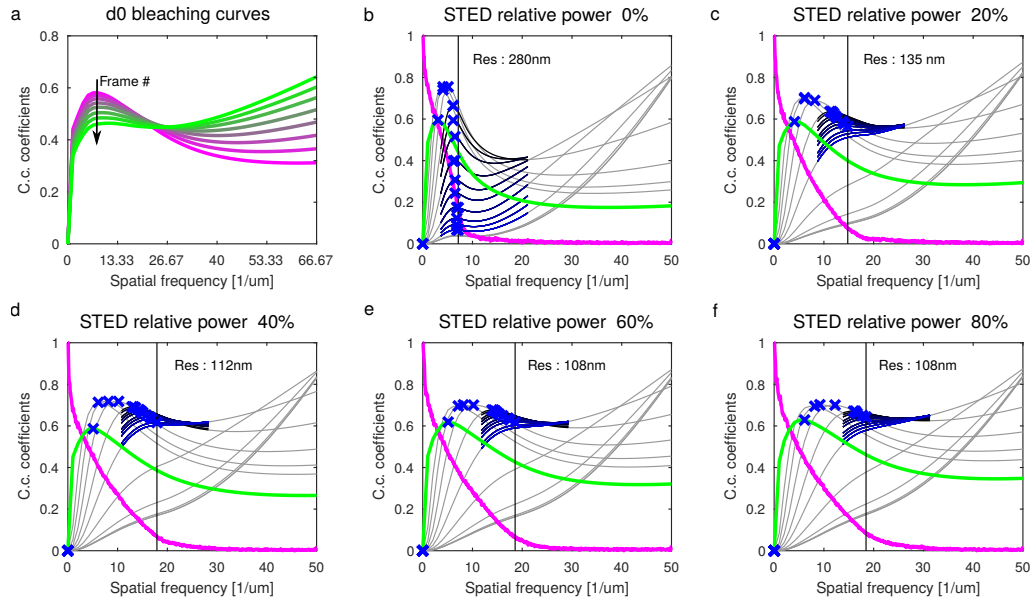
Figure 4.12 – Detailed decorrelation functions for STED. The data corresponds to Figure 4.11g,h. (a) Non-filtered decorrelation function d0 of repeated STED imaging. (b-f) Decorrelation analysis of STED images with varying relative STED power ranging from 0-80%.

STED microscopy critically depends on photophysics that can also be exploited to increase the resolution (lifetime10, photostability11, spectra12, etc.). For pulsed STED experiments, the best resolution is reached when the depletion pulses immediately follow the excitation pulse. We used our resolution estimate as a readout to adjust the delay between the pulses in the Leica system as well as other parameters (STED power, dyes, excitation wavelength, STED delay, etc..) associated with any microscopy experiment.

We show in Fig. 4.13a how the resolution improves as a function of the STED beam intensity for COS7 microtubules labelled with Atto594. We observe that the maximum resolution is reached at about 40 to 60% of relative STED power. Further increases in the STED power has even a detrimental effect on the resolution. Similar experiments were done with Atto940LS. We see (Fig. 4.13b) that the optimal STED power now lies in between 80 to 100% of relative STED power. Fig. 4.13c shows representative data of Fig. 4.13b. We show in Fig. 4.13d that the confocal resolution estimate does not significantly depend on the pixel size. Another crucial parameter for STED imaging is the delay between the excitation and depletion of the fluorophores. An incorrect pulse synchronization will result in less efficient depletion and significantly impact the final image resolution.

We show in Fig. 4.13e the resolution as a function of the STED delay and corresponding representative data in Fig. 4.13f. We observe a drastic improvement in resolution at about Δt=1800ps. Previously, an indirect strategy based on minimizing the remaining fluorescence intensity[130] or an FRC resolution estimate was used[121].We see that an added delay of at
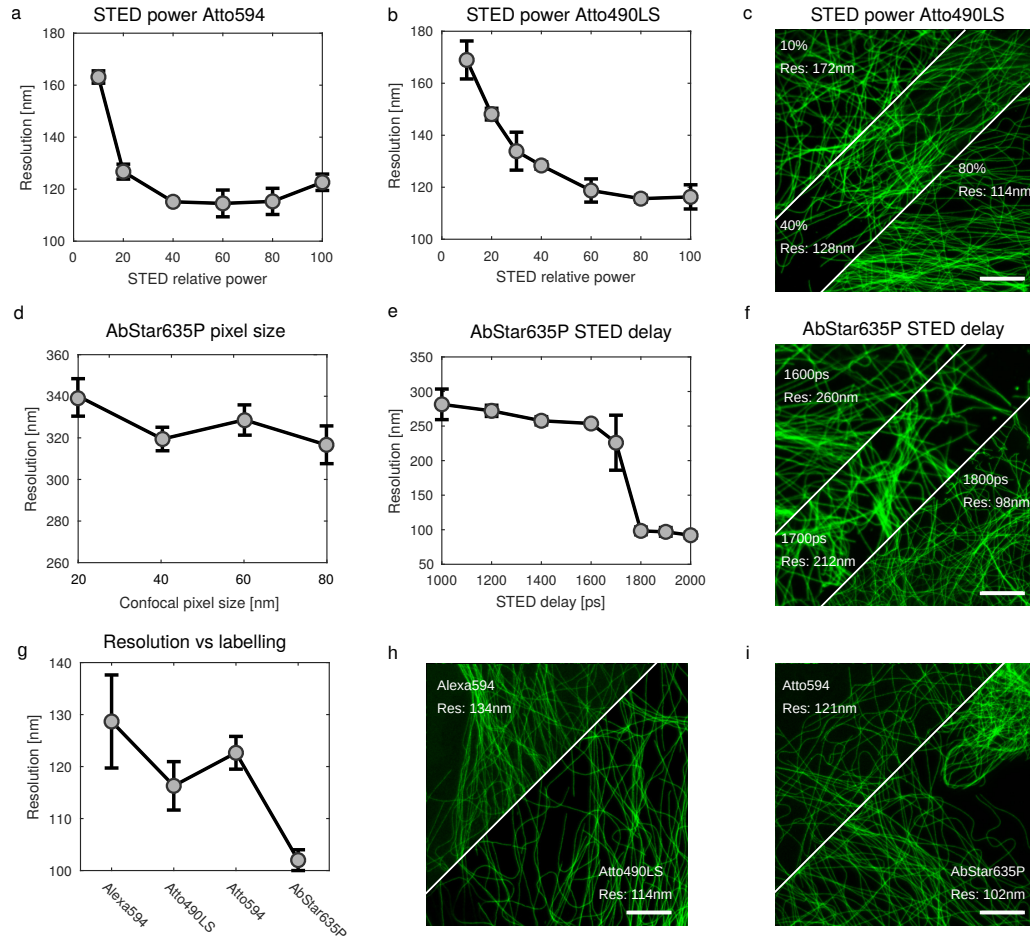
Figure 4.13 – Additional STED experiments (a) Resolution vs STED power for Atto594 labelling. (b) Resolution vs STED power for Atto490LS labelling. (c) Representative STED images for 10, 40 and 80% STED power for the data in (b). (d) Confocal resolution vs pixel size for AbberiorStar 635P labelling (short: AbStar635P). (e) Resolution vs added delay between the excitation and STED laser pulse for AbberiorStar 635P labelling. (f) Representative STED images for 1600, 1700 and 1800ps STED delay for the data in (e). (g) STED resolution for different labelling at 100% STED power. Alexa594 is short for Alexa Fluor 594. (h-i) Representative images of STED for different labelling for the data in (g). The data points were always acquired using a newly focused FOV and/or cell. The gray dots represent the mean value per condition (n=3 for the whole figure) and the error bars indicate the standard deviation. Scale bar, 5 μm.

least 1800ps is required in order to reach the optimal STED regime.

Finally, we also show in Fig. 4.13g how the resolution varies as a function of the dye. Fig. 4.13h and 4.13i show representative images.

4.4.4 Wide field and SIM

High-resolution live-cell STED imaging has been performed, but care should be taken to avoid sample damage due to high-depletion laser powers by special imaging procedures[127]. A super-resolution method that is widely used for imaging dynamics of living cells is Structured Illumination Microscopy[29–31] (SIM). SIM aims at improving the lateral and axial resolution by multiple imaging of the sample with high-frequency illumination patterns[131]. The theoretical resolution improvement of SIM is linked to the illumination spatial frequency. In practice, SIM resolution depends on refractive index mismatch, the pattern modulation contrast and local distortion[42]. Fig. 4.14a shows a pseudo widefield image of actin filaments in U2OS cells28 obtained on a commercial SIM instrument (courtesy of T. Huser). A resolution of about 253nm is estimated by decorrelation analysis (see Fig. 4.14b). Fig. 4.14c shows the SIM reconstruction and its corresponding decorrelation analysis in Fig. 4.14d, estimating a 1.56 fold improved resolution of 161nm. Measuring the position of the illumination peaks in the Fourier transform of the raw data (4.75 and 9.5[$1/\mu m$ for the first and second diffraction order respectively), provides a way to estimate the theoretically expected resolution improvement. We observe that the contribution of the first diffraction order with wide-field resolution $\left(\frac{7.9+4.75}{7.9}\approx 1.6\right)$ fits well with our estimation, indicating that the information encoded in the second diffraction order is not sufficiently contrasted. The use of more advanced reconstruction algorithms may improve this result.
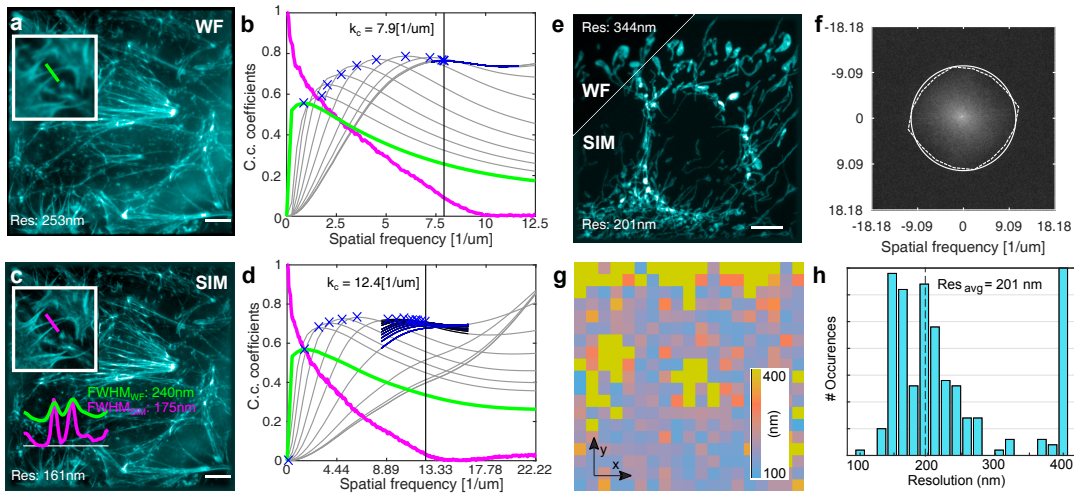
Figure 4.14 – Widefield and SIM (a) Pseudo widefield image (WF, average of the SIM sequence) of the actin network in fixed U2OS cells labeled with phalloidin-Atto 488 (Courtesy of T. Huser). (b) Corresponding decorrelation analysis. (c) SIM reconstruction of (a) with selected cross-sections. (d) Corresponding decorrelation analysis. (e) Pseudo widefield and SIM reconstruction of mitochondria network in U2OS cells labeled with mitotracker (Courtesy of M. Sauer). (f) Sectorial resolution estimation (dashed white line) and average resolution (solid white circle). (g) Local resolution estimate of (e) in tiles of 70x70 pixels with an overlap of 20 pixels. (h) Histogram of local resolution shown in (g). Dashed line indicates the median resolution. Scale bar, 5 μm.

So far, we only considered the global resolution, i.e. averaged over the whole image. In order to account for non-isotropic resolution, we subdivide the Fourier space into sectors and compute the cut-off frequency as a function of the direction (sectorial resolution). Fig. 4.14e shows a pseudo widefield and SIM reconstruction of mitochondria[101] in U2OS cells measured on a different commercial microscope (courtesy of M. Sauer, resolution gain of 1.73). Fig.4.14f displays the Fourier transform of the SIM reconstruction, overlapped with the sectorial and average resolution.

By subdividing the image into smaller tiles (as for FRC in [120]), we can estimate the resolution over the whole field-of-view and reveal local variations in resolution (Fig. 4.14g). Due to the very weak signal in the top and center part of Fig. 4.14e, corresponding sub-regions have large resolution values. In order to preserve the dynamic range, all resolutions larger than 400nm were set to 400nm. Furthermore, the resolution map can be plotted as a histogram (Fig. 4.14h), providing yet another perspective. We also see that the average resolution is approximatively the median of all local resolutions.

4.4.5 Sectorial resolution

The proposed method is very flexible and can be easily translated into higher dimensions. In order to estimate the sectorial and axial resolution, the shape of the mask has to be adjusted. Fig. 4.15a shows another STED image of the microtubules. The Fourier transform of (a) is shown in Fig. 4.15b and reveals a clear asymmetry of the Fourier spectrum. The dashed white circle represents the resolution estimated by our method when applied to the whole image. In order measure the resolution as a function of the direction, the shape of the mask as to be adjusted. Fig. 4.15c indicates how the circular mask has to be segmented in order to estimate the sectorial resolution in 8 directions. In this case, a total of 8 sectors (S1-S8) are defined and a standard decorrelation analysis is performed for each sector.
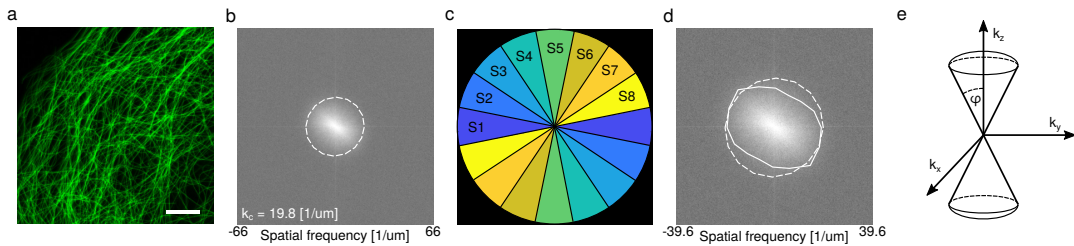
Figure 4.15 – Sectorial and axial resolution (a) Example image. (b) log of abs of Fourier transform of (a) indicating the average resolution as a white dashed circle. (c) Shape of the masks used for the sectorial resolution estimation in 8 directions. (d) Sectorial resolution estimate (solid line) and average resolution (dashed circle). (e) Theoretical shape of the 3D mask required in order to estimate axial resolution. Scale bar, 5 μm.

Fig. 4.15d shows the resolution dependent cutoff frequency (dashed white line), correctly measuring the anisotropy of the Fourier spectrum. Fig. 4.15e illustrates the shape of the mask

required for axial resolution estimation. The parameter φ is the angle of the cone oriented along the z-direction and defines the trade-off between the selectivity of the mask and the noise (small φ means good selectivity but few data points leading to a noisy estimate, large φ means poor selectivity but more robust estimate). The extension of the algorithm to 3D requires to move from polar to spherical coordinate. Another strategy for the estimation of z-resolution could be based on the computation, for all x and y position, of a 1D decorrelation function along the z-axis. This will result in a 2D image, containing the cutoff frequency estimate for each point. A histogram analysis may be used to determine which resolution was the most prominent, providing an alternative mean to assess the axial resolution with ideal selectivity of the z-resolution. However, this question requires further work, investigating for example the effect of a limited number of z-plane.

4.4.6 Bright-field microscopy

In addition to fluorescence microscopy, our method can also be applied to partially coherent imaging.
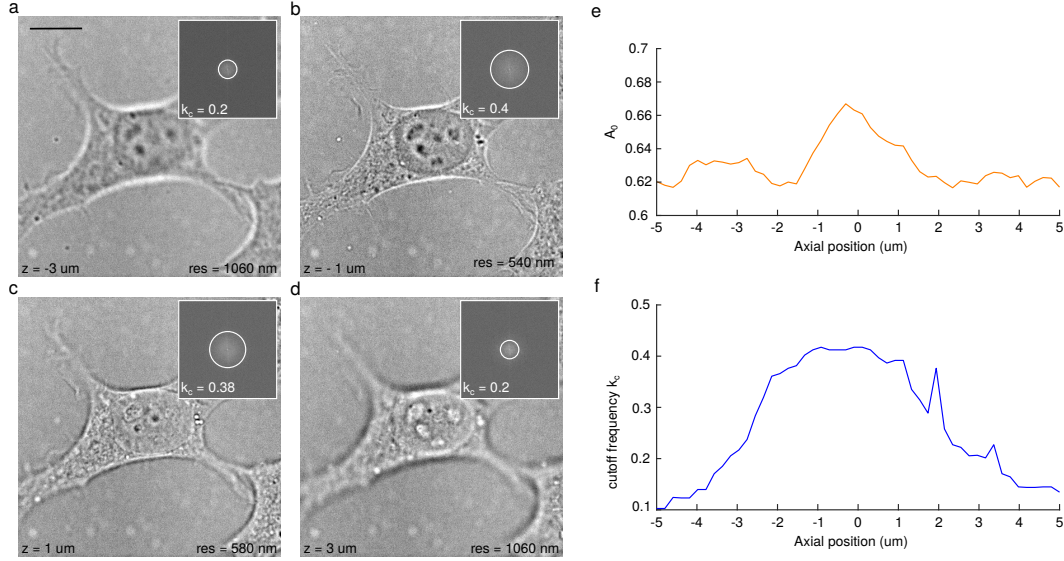
Figure 4.16 – Bright field analysis (a-d) Selected slice of a 3D bright field stack of fixed HeLa cell (Inset: corresponding Fourier transform and estimated cutoff indicated by white circle). (e) A_0 as a function of the axial position. (f) Estimated cutoff frequency as a function of axial position. Scale bar, 5 μm.

We processed a bright-field z-stack (50 slices, 200nm axial step size) of a fixed HeLa cell (Fig. 4.16a-d)4. We see (Fig. 4.16e) that the estimate A_0 is maximal when the cell is in focus and well contrasted. The cutoff frequency estimate demonstrates the ability of the method to estimate the spatial frequency content. As we approach the focus, the cutoff frequency rises continuously until we reach the coverslip at around -2μm. As we move through the cell, the

resolution stays roughly constant, until it starts to drop at around 1μm. The cutoff frequency peaks observed at 2 and 3.4μm are due to highly scattering vesicles.

4.4.7   Stochastic Optical Fluctuation Imaging

Sub-diffraction imaging can also be achieved by analysing a time series of stochastically blinking emitters. Stochastic Optical Fluctuation Imaging5,6 (SOFI) achieves super-resolution by computing high-order spatiotemporal cumulants. SOFI processing is of interest to analyse because it predicts a resolution improvement of $1/\sqrt{n}$, where n is the correlation order and $1/n$ after deconvolution and brightness linearization. It provides an ideal test case for our resolution estimator.

Fig. 4.17a shows the results of SOFI analysis (up to 6th order) of MEF cells expressing paxillin labelled with mEos277 (courtesy of H. Deschout[81]). Fig. 4.17b displays the results of the decorrelation analysis, where the raw cumulants follow the theoretical resolution improvement up to 70 nm for 6th order linearized SOFI, indicating good blinking statistics. The deviation observed for the widefield (average of the whole sequence, here denoted as SOFI 1) and 2nd order SOFI can be attributed to sub-optimal out-of-focus light rejection. Similarly, the linearized SOFI cumulants, obtained by 10 iterations of Lucy-Ridcharson deconvolution and taking the nth root of the SOFI image, follow a similar trend close to the theoretical value. The deconvolution operation by itself constitutes an interesting case study for our algorithm. We show (see Section 4.4.10) that the resolution can be set to any value, as a function of the input point-spread function and number of iterations of the deconvolution. It is the duty of the user to ensure that the resolution is not enhanced beyond the limit supported by the microscopy method. Our algorithm can thus be used to quantify deconvolution strength but not the validity of the deconvolution.

To minimize bleaching and drift artefacts, practical SOFI processing is achieved by first subdividing the whole acquisition into sub-sequences, computing SOFI and averaging the results of the sub-sequences[65, 132]. By using our decorrelation analysis over the resulting SOFI image for various sub-sequences lengths, we are able to identify the optimal resolution-SNR sub-sequence length for the given input data. Fig. SR4.1c shows the results of such an analysis (sub-sequence length ranging from 50 to 4000 frames), performed on a sequence of blinking Alexa647 targeting microtubules of HeLa cell (images shown in Fig. 4.21, Fig. 4.17a, 8000 frames in total). For this data, we found an optimal sub-sequence length of 1500 frames.

Fig. 4.17d and 4.17e demonstrate how the total number of frames used to compute SOFI impacts the resolution in HeLa-cell microtubules labelled with Alexa 647. We see that 50 frames already allow the computation of a 3rd order SOFI image. However, due to the blinking kinetics, many more frames are required to properly resolve the underlying structure. We also see that the resolution is slightly better when the image consists only of sparse point-like structures. This is due to the fact that our algorithm estimates the resolution from a single image. Using only 50 frames, the algorithm sees a sparse distribution of high-frequency dots. As we include more frames in the analysis, a larger-scale structure containing more low
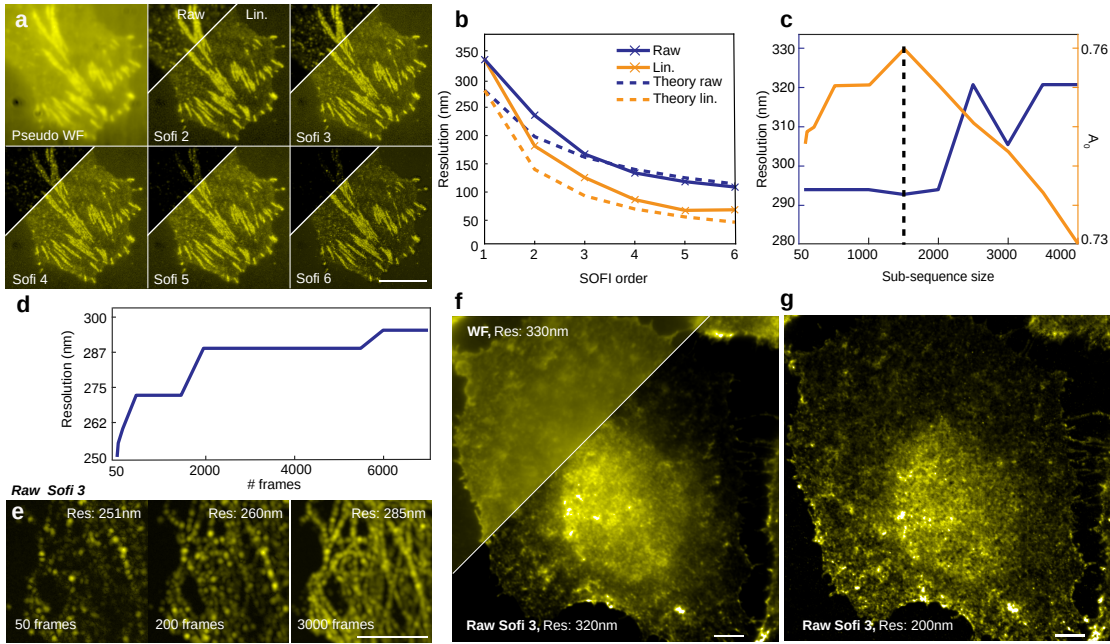
Figure 4.17 – SOFI (a) Raw SOFI and Linearized SOFI images of focal adhesions in MEF cells expressing paxillin-mEos2 (courtesy of H. Deschout) shown up to order 6. (b) Estimated and theoretical resolution vs the SOFI order. (c-e) Cumulant analysis of microtubules in HeLa cells immunolabeled with Alexa Fluor 647. (c) Resolution and SNR estimate vs the sub-sequence size used for SOFI processing. (d) Resolution estimate vs number of frames. (e) Raw SOFI 3 images for 50, 200 and 3000 frames. (f) Un-optimized raw SOFI image of fixed HeLa cells labeled with wheat germ agglutinin-Atto 565 using "default" processing parameters. (g) Same images as (f) after optimization of the resolution. Scale bar, 5 μm.

frequencies starts to emerge, leading to a slightly modified resolution estimate. Finally, Fig. 4.17f shows a raw 3rd order SOFI image of HeLa cells stained with wheat germ agglutinin-Alexa 488, processed with default parameters (first 1000 frames removed and sub-sequence length of 500 frames). Fig. 4.17g shows the same image, after optimization of the sub-sequence length and the number of frames to be removed at the beginning and the end of the acquired data to obtain the best resolution (1800 first frames removed, subsequence length of 1000, no frames removed at the end of the sequence). The optimized processing procedure results in a 1.6-fold improvement of resolution compared to the starting image.

4.4.8 Single molecule localization microscopy

Finally, we applied our method on single molecule localization microscopy [45, 48, 133] data. In this case, super-resolution is achieved by the individual localization of a subset of sparsely and stochastically blinking emitters in successive image frames. By fitting the emission point-spread functions, single- and multiple-emitter positions can be determined with nanometric accuracy[134, 135]. To estimate the resolution, our method requires a rendered image. We

validated, using simulations, that our algorithm is able to correctly estimate the resolution in SMLM. Fig. 4.18a shows a STORM image based on 16000 frames of Abberior Flip 565 - immuno-labelled microtubules in COS-7 cells.
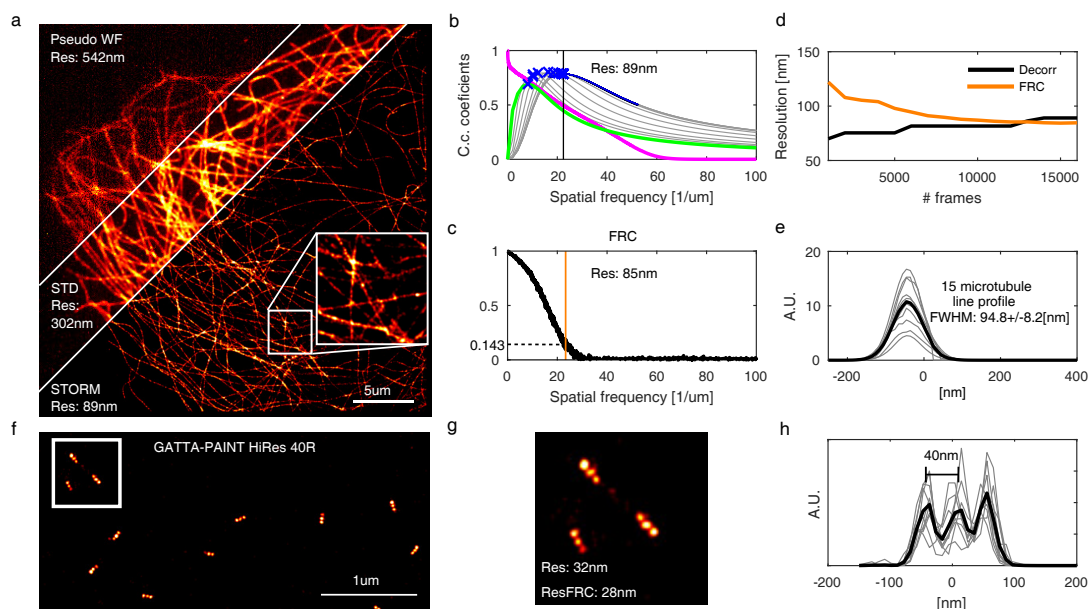

Figure 4.18 – Localization microscopy (a) Pseudo widefield (WF), standard deviation (STD) and STORM image of microtubules in COS 7 cells labelled with Abberior Flip 565 based on 16000 frames. (b) Decorrelation analysis of (a). (c) Fourier Ring Correlation analysis of (a). (d) Decorrelation resolution (black line) and FRC resolution (orange line) as a function of a number of frames. (e) Line profile of 15 randomly selected microtubule cross-sections (f) (f) GATTAquant PAINT image of HiRes 40R nanoruler with mark-to-mark distances of 40nm. (g) Zoom of (f) and decorrelation and FRC resolution estimate. (h) 10 line profiles of HiRes 40R molecules indicating a resolution better than 40nm.

With self-blinking dyes[136, 137], it is not possible to take a widefield image. We thus obtained a pseudo widefield (WF) and standard deviation (STD) image by computing the temporal average and STD of all frames. We estimate a resolution of 542nm for WF due to the low SNR of the image, 302nm for the STD image and 89nm for the STORM image. Fig. 4.18b and c display the corresponding decorrelation analysis and FRC curve, respectively. Both estimates agree on the resolution, with FRC (estimated resolution of 85nm) being slightly more optimistic, consistent with the behaviour observed in simulations and reported recently by Marsh et al[134].

Fig. 4.18d shows how our method and FRC resolution vary as a function of the number of frames. We observe a drastic difference in the predicted resolution only up to 5000 frames. For a low number of frames, the localization events in the two split FRC images are too sparse to produce significant correlations, leading to a large resolution estimate. On the other hand, our method only considers a single image, consisting of sparse Gaussians with no apparent structure but excellent SNR (rendered localization image without noise). This leads to a

very optimistic resolution estimate with the localization uncertainty as a lower bound. As we increase the number of frames, the two random subsets of localization events start to correlate and the FRC resolution estimate decreases. Similarly, as we include more localization events, a larger-scale structure (containing low spatial frequencies) emerges. Consequently, our resolution estimate increases as the structure is built up. We observe that both methods converge at approximately the same speed at around 12000 frames, with FRC estimating a slightly better resolution[138]. Fig 4.18e shows randomly selected microtubules cross-sections. The apparent average microtubule diameter of about 95nm is consistent with the resolution estimate and secondary immunostaining, which increases the apparent microtubule diameter by 10-30nm[139, 140].

Fig. 4.18f displays an image of GATTAquant HiRes 40R nanorulers[122] (courtesy of P. Tinnefeld and J. Schmied). The closeup of three molecules (Fig. 4.18g) as well as line profiles of individual molecules (Fig. 4.18h) show that the three point-source spaced by 40nm can be resolved. Our algorithm estimates a resolution of 32nm while FRC estimates a resolution of 28nm, again being slightly more optimistic.

4.4.9 Single Molecule Localization Microscopy simulations

To confirm that our algorithm is also able to estimate the resolution of localization based image, we conducted simulations. The simulation consists in a total of 16000 point emitters forming a regular pattern of pair of lines with decreasing spacing, starting from 128nm to 8nm (see Fig. 4.19a). Each line is 400nm long and 2nm wide, corresponding to a density of 625'000 molecules per μm^2. The effect of diffraction and of the limited numerical aperture is simulated by convolving the point emitters (represented on an oversampled grid with an up-sampled pixel size of 1nm) with an incoherent 2D airy function (corresponding to a wide field resolution of 215nm) of integrated intensity I_{ON} determining the average number of photons per frame and per emitters. The blinking required for the localization of the emitter is simulated by a Markovian process where the ON time (number of frames where the molecule emits photons), the OFF time (number of frames where the molecule does not emit photons) and the bleaching time (number of frames before the molecule is not able to emit photons anymore) all follow an inverse exponential law of characteristic time $T_{ON} = 2$, $T_{OFF} = 1000$ and $T_{bl} = 2000$. Therefore, at each frame and for a total of 1000 frames, only a sparse subset of emitters contributes to the signal intensity, typical for SMLM. The final camera signal is then obtained by adding shot noise and a Gaussian background noise (Fig. 4.19b). The molecules are then localized using ThunderSTORM[141], filtered to reject unphysical or poor localization events and rendered in Matlab by replacing each localization by a Gaussian of standard deviation equal to the localization uncertainty[62, 63] (Fig. 4.19c) that we compute in Matlab.

Each pair of lines are then isolated and averaged along their major orientation (Fig. 4.19d), which allows us to compute the contrast between the maximum intensity I_{max} and the intensity in the dip between the two lines I_{dip}, defined as $M = \frac{I_{max} - I_{dip}}{I_{max} + I_{dip}}$. By repeating this

computation for all the sub-structures, we are able to compute an effective Modulation Transfer Function (MTF), which provide an objective way to determine the resolution of the reconstructed image (Fig. 4.19e). We see that as the spacing between the lines diminishes, the contrast drops almost linearly. We then define the resolution of the image to be the intersection of the MTF with the threshold 0.1, which corresponds to the modulation contrast of two point emitters spaced by a distance equal to the resolution as defined by Abbe. We obtain an effective resolution of 32nm.

We then use our algorithm on the reconstructed image (Fig. 4.19c) and compare its value with the effective resolution. Our algorithm estimates a resolution of 36nm (Fig. 4.19e, green dashed line), which is in perfect agreement with the previous simulations (see section 4.3 above). The resolution estimate provided by the FRC metric and a threshold of 0.143 predicts a resolution of 27nm, which is more optimistic estimate as it corresponds to a contrast of 0, consistent with the literature[138].

We repeated the simulations by varying the number of counts per point spread function (via adequate tuning of I_{ON}) and keeping the background noise constant. For each I_{ON}, we varied the off-time T_{OFF} from 500 to 1250 in steps of 250, effectively changing the average number of emitters ON per frames from 34 to 14 and the average number of blinks per emitters from 0.98 to 0.38. For each reconstructed image, we then computed (Fig. 4.19f) the Ground Truth (GT) resolution from the MTF for $M = 0.1$ (solid black line) and $M = 0$ (dashed black line), the resolution using the decorrelation analysis (solid green line) and the FRC resolution using the 0.143 threshold (solid magenta line) and using the 3σ criterion (dashed magenta line). We see that both methods are able to pick up the resolution improvement due to the higher number of photons per psf. However, we also see that our estimate is in good agreement with the ground truth resolution estimate, while both FRC criteria overshoots the ground truth resolution with $M = 0$.

We also show (Fig. 4.19g) how both algorithm performs as a function of the uncertainty threshold imposed on the localization prior to rendering. We filter any localization event with an uncertainty greater than the uncertainty threshold. We see from the ground truth resolution that as we remove poorly localized events, we indeed improve our ability to resolve the fine structures in the image. Our algorithm is also able to pick up this trend. We do however observe a clear difference of behavior when removing more than 78% of the total localization. In this case, the FRC resolution jumps to about 100nm while our resolution estimate drops below the ground truth resolution. This behavior is due to the difference in how the two algorithms try to estimate the resolution. FRC is based on splitting the localization in two stochastically independent subsets. If the number of localization is too low, the two images cannot correlate and thus the algorithm predicts a deterioration in resolution. On the other hand, the decorrelation analysis, which works on a single image will have a completely opposite prediction. All the algorithm see is a sparse distribution of very high-frequency Gaussians. The corresponding resolution in terms of Fourier space frequency content is therefore over-estimated.
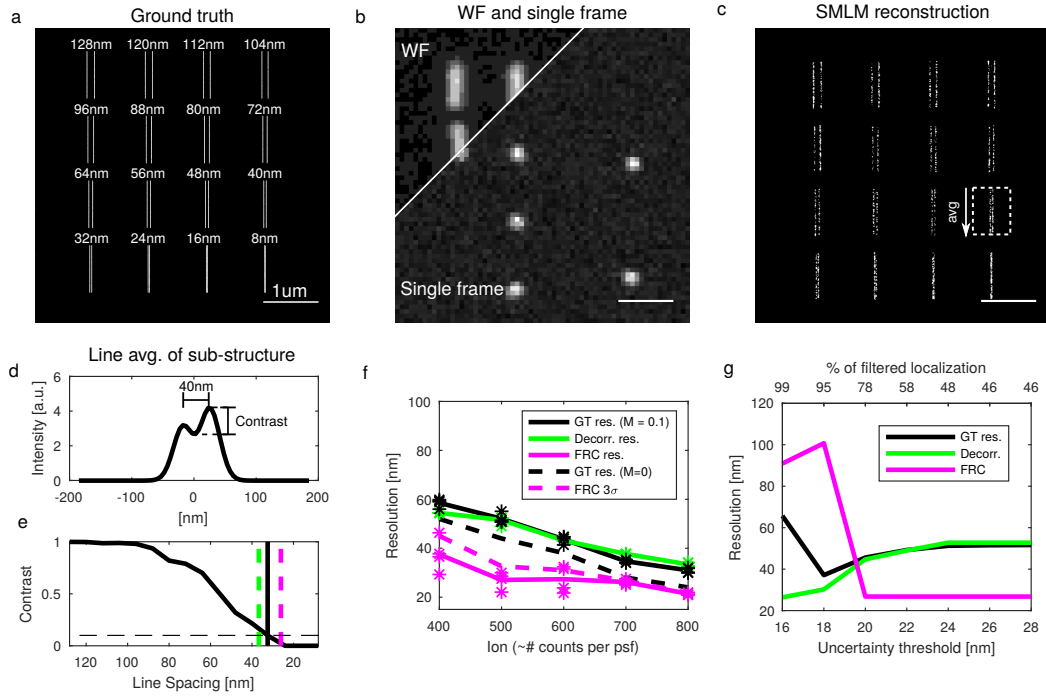
Figure 4.19 – Simulations of Localization microscopy. (a) Spatial distribution of point emitters forming a series of lines with decreasing spacing from 128 to 8nm. (b) Temporal average (wide field) and single-frame of blinking emitters. (c) SMLM reconstruction using ThunderSTORM and Matlab; the dashed rectangle indicates the selection of a sub-structure and the arrow the direction of averaging. (d) Intensity profile of the sub-structure indicated in (c). (e) Contrast as a function of the line spacing for the image shown in (c); vertical black line: Ground truth resolution, green dashed line: decorrelation resolution, magenta dashed line: FRC resolution. (f) Ground truth resolution (black line: M=0.1, dashed black line: M=0), decorrelation resolution (green line) and FRC resolution (magenta line: 0.143 threshold, dashed magenta line: 3σ as a function of I_{ON} for various T_{OFF} (the lines are showing the mean resolution over T_{OFF}; stars are showing the data points for the GT res, decorr. res. and FRC res.). (g) Ground truth (black line), decorrelation resolution (green line) and FRC resolution (magenta line) as a function of the uncertainty threshold.

Finally, it has been shown that multiple blinking events can severely impact the FRC resolution estimate by introducing spurious correlations[120]. While this effect can in principle be mitigated, it requires an accurate estimation of the underlying blinking statistics[142]. While it is possible to compensate for this effect by estimating the spurious correlation factor Q from the reweighted numerator of the FRC, it is not easily applicable when the blinking statistic is not precisely known. We performed simulations with added multiple blinking events. All fluorescent emitters that just turned OFF has a certain probability, controlled by the number pMB (probability of multiple blinking), to switch ON again. We show in Fig. 4.20a the log of the histogram of number of blinking events per molecule for different pMB. As expected, the larger the probability, the more a molecule is likely to blink during the same amount of time

(1000 frames). We also show in Fig. 4.20b the resolution estimation as a function of pMB. We see that the FRC resolution (orange line) estimation gets lower with the probability due to increasing spurious correlations. In contrast, we see that our estimate (blue line) as well as the ground-truth resolution estimate (black line) are insensitive to the probability of multiple blinking events.
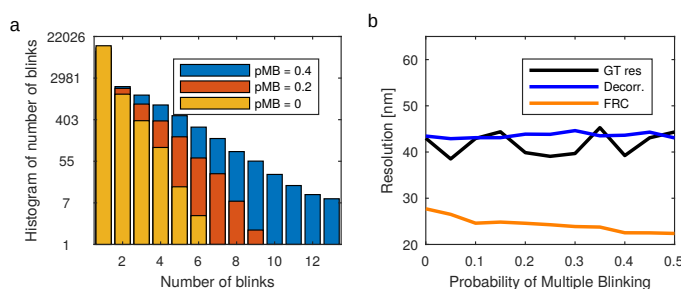

Figure 4.20 – Resolution estimation vs multiple blinking. (a) Histogram of number of blinking events for three different values of probabilities of multiple blinking (pMB) on a logarithmic scale. (b) Ground-truth (black line), decorrelation (blue line) and FRC (orange line) resolution as a function of the probability of multiple blinking.

4.4.10 Deconvolution and post-processing

In the following section, we discuss and illustrate issues arising when applying various post-processing algorithm prior to the decorrelation analysis.

First we show in Fig. 4.21a, 3rd order raw SOFI image of microtubule network labelled with Alexa647. The Fourier transform is shown in the inset. Fig. 4.21b shows its corresponding decorrelation function. Fig. 4.21c shows the same image after a basic Fourier filtering operation. In this case, a simple binary mask with a normalized radius of 0.6 has been applied. While the image looks almost identical to the original, the decorrelation analysis is strongly affected by this artificial operation. It interprets the mask as a transfer function. In this very specific case, the mask does not affect the shape of the function near the real cutoff frequency so one could circumvent the issue by only computing the curve up to the spatial frequency 0.5 for example (Radius max. = 0.5 in the case of the imageJ plugin). However, if the mask is closer to the cutoff, this simple trick is likely to fail and no resolution estimate could be performed on such image.

Fig. 4.21e shows the same image, after Lucy-Richardson deconvolution (Matlab R2017b "deconvlucy") with various input Gaussian PSF FWHM (ranging from 108 to 238nm). The decorrelation analysis shows very drastic changes where the resolution goes from 288 to 100 nm. Fig. 4.21f shows their corresponding Fourier transform, where the effect of deconvolution is now clearly visible (10 iterations of LR, psf FWHM of 238, 180 and 108nm respectively). Fig. 4.21g shows the resolution estimate of the same image for different FWHM and number of iterations of Lucy-Richardson deconvolution.
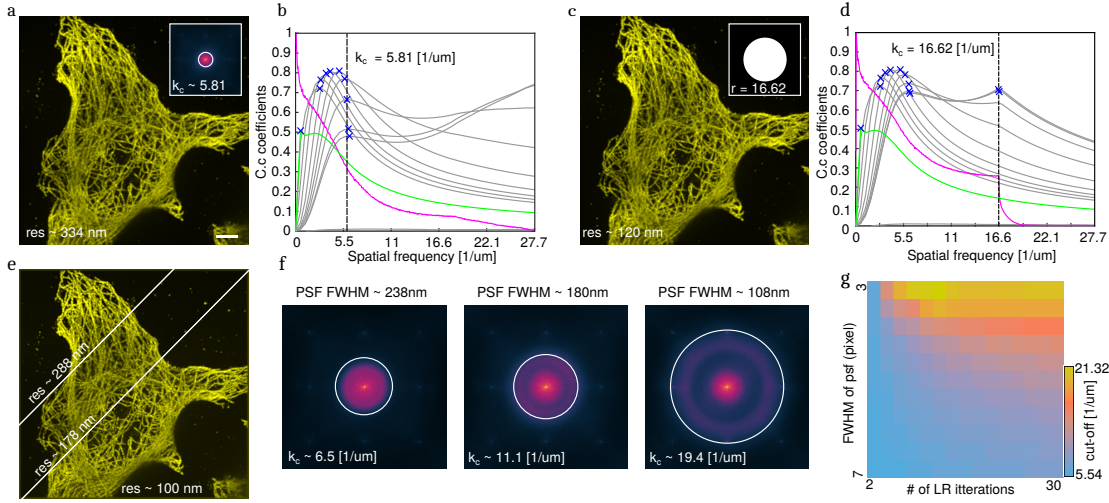
Figure 4.21 – Fourier filtering and deconvolution (a) Raw SOFI 3 images and its Fourier transform in inset. (b) Corresponding decorrelation analysis. (c) Fourier filtered version of (a) with the used mask in inset. (d) Corresponding decorrelation analysis, showing incorrect result due to the artificial intervention. (e) Lucy-Richardson deconvolution using 20 iterations and a FWHM of 238, 180 and 108nm. (f) Corresponding Fourier transform, showing how the deconvolution modified the frequency spectra and the resolution estimate. (g) Resolution estimation for various FWHM and number of iterations of LR deconvolution. Scale bar, 5 μm.

It demonstrates that the resolution can be artificially set to any value. We here have to mention that we do not recommend to blindly deconvolve an image and that proper deconvolution ideally requires an experimentally acquired point-spread function. The purpose of this section is just to demonstrate how ANY deconvolution will influence, in general, our method. This means that our algorithm can be used as a tool to quantify the deconvolution strength and also to estimate the ideal number of iterations but not check the validity of the deconvolution.

In addition to Fourier filtering and deconvolution, there are also several sources of artificial high-frequencies that we came across during the development of the algorithm. This is a non-exhaustive list of common practice that may hinder the ability of the algorithm to estimate the resolution:

- Removing negative values by applying a threshold creates local non-linearity, adding a high-frequency signal to the image.

- Background subtraction algorithms (especially morphological operation based such as the rolling-ball algorithm) are prone to produce high-frequency artefacts.

- Camera lines artefacts or fixed pattern noise are very-high frequency signals that might lead to overestimation of the resolution. The camera pattern should be characterized and used to pre-normalize the image.

- Image up-sampling/down-sampling, in real space or via Fourier zero-padding, should be avoided.

- Small images are more vulnerable to noisy peaks in the decorrelation analysis (256x256 is usually large enough).

- Quantization error when changing the bit-depth of the data may introduce edges all over the image, which can result in wrong estimate. The images should be normalized to the full bit-depth prior to quantization.

5 Deep neural network optical DNA mapping

5.1 Optical DNA mapping

So far we only discussed the use of fluorescence and super-resolution microscopy for qualitative structural assessment of biological sample. However, it can also be used to achieve quantitative measurement of biological sample. We now consider the field of optical DNA mapping, where measurements aim to extract quantitative information from the microscopy image.

Optical mapping[143] has been an excellent technique for large-scale reading of DNA sequences. In short, the working principle of optical mapping is to bind fluorescent molecules (see Fig. 5.1) at specifics DNA sequences (CG, TCGA, etc...) through the use of methyltransferase enzymes[144] (respectively MpeI, TaqI, etc...) or intercalating dyes of AT-rich regions [145]. Similar to a barcode, the relative distance between two labels provides a sequence specific information. By imaging the intensity profile of the labelled DNA molecule using nanofluidics [146] or stretching the DNA on a glass slide[143] and comparing it to a database of sequence [147, 148], it is possible to identify to which species it belongs and even find its position into the larger genomic sequence.

One application of DNA mapping is the species identification of a mixture of viral and bacterial sample. Optical DNA mapping can provide high throughput species identification and requires
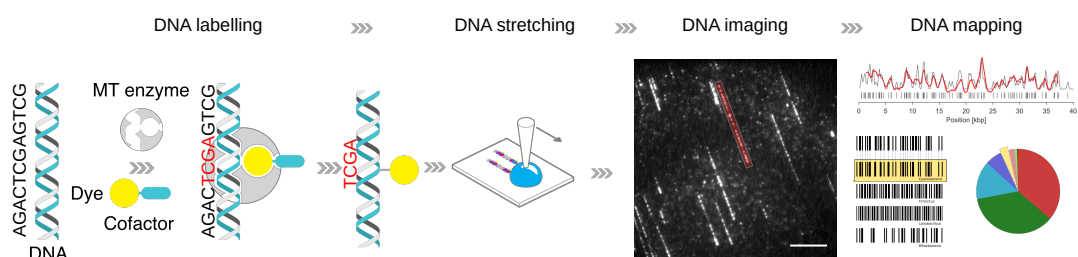

Figure 5.1 – Workflow of optical DNA mapping. This figure is adapted from [148].

long sequence read [149], compared to other approaches such as 16s ribosomal DNA or whole-genome sequencing [150] which are unable to achieve both long sequence read and high throughput[148]. Being able to estimate the bacterial population of a given sample finds interest in the study of microbiome composition, which has been shown to be correlated with health and diseases[2, 151, 152].

This chapter will present two approaches where we used deep neural networks to assist the segmentation of the DNA intensity profile from images and to map the intensity trace to a database of species.

The automatic segmentation of DNA images is a mandatory step for high-throughput optical DNA mapping. The challenge of automatic segmentation is that, at a small scale, the DNA molecule appear as sequence of dots with random gap between them. At a larger scale, the dots are arranged in a line with a small curvature. While there exist many approaches that can be design to automatically extract the DNA molecules, they all suffer from an excessive number of user-defined parameters that have to be manually adjusted to account for image to image variations. If we include these variations in a database, a neural network would be able to learn how the image of a DNA look like and output a normalized probability map that a DNA molecule is present in a pixel. A simple line detection algorithm could then be used to extract the DNA molecule position.

There already exist several approaches to classify optical DNA map such as the Smith-Waterman algorithm or cross-correlations combined with statistical resampling and p-value. The issue is that these methods are computationally expensive and do not scale well with the length of the DNA map. We investigate here how using neural networks as correlators might speed up the matching process.

5.2 Machine learning and Neural networks

The term *machine learning* was coined in 1959 by Arthur Samuel[153]. It refers to the ability of a computer program to learn, in a supervised or unsupervised manner, how to perform a given task based on a set of data. Typical tasks of early machine learning algorithm include classification of data into predefined class, building of a mathematical model (regression algorithm) or finding unknown structure in the data (cluster analysis).

An artificial neural network[154] is a class of machine learning which architecture follows a specific structure inspired from nervous activity. The building block of a neural network is called the perceptron[155]. It is a mathematical structure that accepts a fixed number N of inputs $x = \{x_0, ..., x_N\}$, takes their weighted average $w = \{w_0, ..., w_N\}$, applies a non-linear activation function $g(s)$ and returns a single number y. Formally, it can be written

$$y = g\left(\frac{1}{N} \sum_i^N x_i w_i \right) \tag{5.1}$$

The goal of the activation function is to add non-linearity into the network. Typical activation functions used in this chapter are the sigmoid activation $g(s) = \frac{1}{1+e^{-s}}$ and the hyperbolic tangent function, which have both the property to map any input to a number between -1 and 1. A collection of perceptrons which accepts an arbitrary number of inputs is called a dense layer. The number of outputs is given by the number of perceptrons in that layer. By stacking several layers, we form the simplest form of a deep neural network also called a fully connected network.

To perform a certain task, the many weights of the network need to have a certain value. Obtaining theses values is the purpose of the training. In order to train a network, a database containing a pair of inputs and target output has to be constituted. The training procedure consists in feeding the network with the input and measuring the error between the network output and the target output. The error is then back-propagated through the network to apply a small correction to the weights such that feeding the same input to the network will produce a slightly lower error. In order to avoid biases toward the training dataset, the dataset is split into a training and a validation dataset. The validation is not used to update the weight but is used to verify that the information learned by the network also improves its performance on unseen data. The training is divided into several epoch were the training and validation data set might be shuffled and several training parameter updated. After convergence of the network, the network is tested against a test dataset. Unlike the validation set, the test dataset was never shown during the training which allows to measure the final performance of the network.

Fully connected network are very powerful for classification or compression task but are not well suited for image processing as they do not take advantage of spatial correlations. Another type of network used in this chapter that solves this problem is called a convolutional neural network[156]. A convolution layer works by convolving the input image with a filter of kernel size n and weights $w = \{w_0, ..., w_{n^2}\}$. This time the weight of the filter are updated during the training. Convolution layer can be combined with fully connected layer and vice-versa. Many more layers exists to solve problem specific issues and to build more complex architecture such as generative adversarial network[157] or long-short term memory network[158].

In this thesis, all networks were developed in Python, using the open-source Keras high level API[159] and tensorflow in back-end.

5.3 Deep DNA segmentation

To achieve high throughput species identification through optical DNA mapping, it is necessary to automatize as many part as possible of the whole pipeline. The task we are interested in consists in taking an input microscopy image of labelled and stretched DNA molecules and output the coordinates of the DNA molecules present in the image. While this task is, except for rare edge cases, trivial for a human, it is very challenging due to the nature of the signal, the presence of varying gap, the increased background signal near the DNA molecules, the free
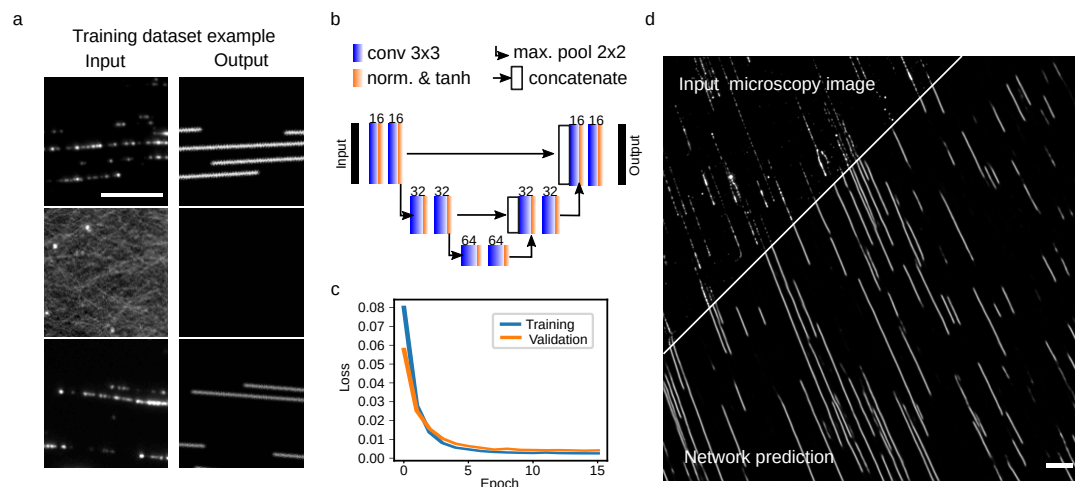
Figure 5.2 – Convolutional neural network assisted DNA segmentation. (a) Examples of input and output training dataset. (b) U-net architecture used. The number above the convolution layers indicates the number of filters used. (c) Results of the training. (d) Output of the network on an unseen image. Scale bar 5μm.

dyes and the entanglement of DNA molecules. There actually exists many methods that can be combined to solve this task, such as background removal, morphological operations, Hough transform, peak finding, etc... However, all the methods we evaluated were heavily relying on external parameters that have to be fine tuned in order to get high quality segmentation. Here we show how a convolutional neural network can be used to denoise, remove the background and make continuous lines by connecting the signal of adjacent fluorophores. The neural network filtered image can then be fed in a standard line finding algorithm to segment individual molecules.

Fig. 5.2a shows few examples of images used for the training of the network. The images were obtained by visually inspecting and manually drawing lines on top of as many DNA molecules as possible. The start and end point of each line was saved as ImageJ ROIs. Only single molecules were selected and obviously entangled DNA molecules were ignored. The output training dataset was obtained by redrawing the selected lines on a black background. The obtained image was then convolved with a Gaussian with a FWHM of 2 pixels. In total, 60'000 training images of 128x128 pixels were generated from about 150 images of 1000x1000 pixels, including data augmentation by mirroring. To improve the convergence of the network, all the images are preprocessed to orient the molecules along the horizontal axis. This preprocessing step can be reliably achieved using a Hough transform[160] to find the DNA molecules main orientation.

Fig. 5.2b shows the U-net architecture[161] used. The U-net architecture is made of several convolution layer combined with maximum pooling operations (2x downsampling where the maximum of each pixel group is used instead of the mean) to progressively compress the spatial features. In addition, the output of the layers before each max. pooling are copied and directly concatenated to their corresponding convolution block skipping the feature

compression. This architecture helps the network in outputting high-frequency images. Fig. 5.2c shows the loss resulting of the training as a function of the epoch. The network was trained using Adam optimizer[159] (learning rate of 10^{-4}) and mean squared error loss function with a batch size of 50 for 16 epochs. We observe a fast convergence of the network were each epoch takes about 1 minute to complete. Fig. 5.2d shows the prediction of the network on an unseen image. The discontinuous DNA molecules are replaced by solid lines, single isolated dyes are completely discarded and the brightness variations along the DNA molecules are also suppressed.

The final segmentation of DNA molecules is then achieved by thresholding the image at a value of 0.25, clustering all the pixels that are 4-connected and computing the main axis and end points of each clusters. Using the end points of each cluster, the intensity along the path of the molecule is then extracted from the microscopy image. The only remaining parameter concerns the additional connection of two aligned molecules if the spacing was too large for the network to connect them. This step is necessary as the DNA map can have a large gap due to a lower labelling density.

5.4 Deep DNA mapping

As discussed before, a typical task of machine learning and neural networks is to classify data. In this section, we investigate how a convolutional neural network followed by a dense network can be used to classify DNA maps against a given database of species.

5.4.1 Viral DNA mapping

Optical mapping of viral DNA is an interesting case study as some are commercialized and as they are relatively short (about 20 to 30 microns once stretched on the glass substrate). For a pixel size of 80 nm, this means that the intensity trace of a viral DNA map does not exceed 400 pixels.
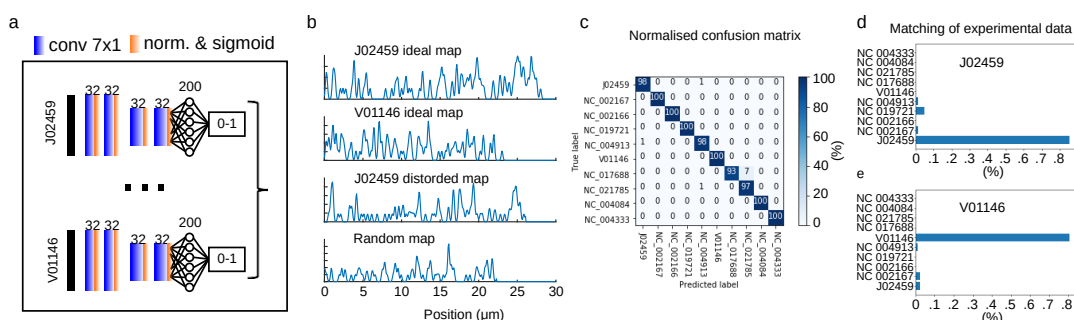

Figure 5.3 – Mapping of viral DNA. (a) Network architecture with one network per species. (b) Example simulated intensity for lambda DNA (J02459), T7 DNA (V01146), distorted lambda DNA and random map with similar labelling density. (c) Mapping confusion matrix of the unseen simulated test dataset. (d,e) Results of the network on experimental data.

The chosen strategy to classify DNA traces is shown in Fig. 5.3a. For each species from the database, a corresponding network is trained. The network consists of a 400x1 input followed by two convolutional layer, a max. pooling layer and two additional convolutional layer, which act as feature extraction layers. The classification is handled by a fully connected layer of 200 perceptrons using a sigmoid activation function and a final single perceptron which outputs a value between 0 and 1. The training is based on simulated data. The simulated data is obtained by downloading the theoretical position of each label from a public database. We then distort the map to simulate the experimental variations that will affect the label distribution. We start by removing a fraction of labels from the original map (labelling efficiency 0.6-0.7). A number of false positive labels are then added in proportion to the map length (false positive labelling rate of 0.3-0.5 labels per kilobase-pair). A probability of double labelling at a correct sequence site is also included (double labelling probability of 0.05-0.1). Finally, the trace is randomly shortened the unavoidable random DNA breaking when being pipetted. Non-linear stretching can also be included but did not led to any significant improvement in the matching and can be assumed to be negligible for short DNA fragment. The map is then linearly stretched by a random factor comprised in the range 1.65-1.75 and convolved with a Gaussian point-spread function to simulate the limited imaging resolution. Fig. 5.3b shows examples of idealized, distorted and randomized intensity traces.

The training database of each network is made of 10000 distorted traces, with 5000 belonging to the specie that the network should recognize and the 5000 rest being randomly drawn from other species traces.

All networks were trained using the Adam optimizer (learning rate of 10^{-4}) and a mean squared error loss function with batch size of 50 for 50 epochs. Fig. 5.3c shows the confusion matrix of the classification using the collection of neural network on unseen simulated data using similar distortion parameters. As expected, the neural networks are able to handle the many distortion that a labelled DNA molecule can undergo and still be able to correctly classify them with an accuracy ranging from 97 to 100 %.

Fig. 5.3d and e shows the performance of the collection of network on experimental data of lambda (J02459) and T7 (V01146) DNA. Despite the fact that the networks were trained on simulated data, they are completely able to classify real data. Compared to a p-value analysis[148], neural network classification shows a better sensitivity (about 85% and 77% for p-value) but also a lower specificity.

5.4.2 Bacterial DNA mapping

The major difference between viral and bacterial DNA is the length of the map. Compared to a viral DNA molecule which takes less than 400 pixels, bacterial DNA can take more than 30'000 pixels. Since current sample preparation methods limits the size of the DNA molecules to 400-600 pixels, the approach proposed to map viral DNA cannot be transferred to bacterial DNA mapping. In this section, we aim at training a single network which would act as a correlator between an ideal intensity trace and a distorted experimental trace.

Fig. 5.4a shows the architecture of the network used. The network is composed of two distinct inputs of size 400x1, one for the reference ideal trace and one for the experimental distorted trace. Both traces go through several convolution, hyperbolic tangent activation and max. pooling layer before being concatenated. After another set of convolution layer, two fully connected layer followed by a single perceptron with a sigmoid activation function are used to make the decision if the two traces are similar.
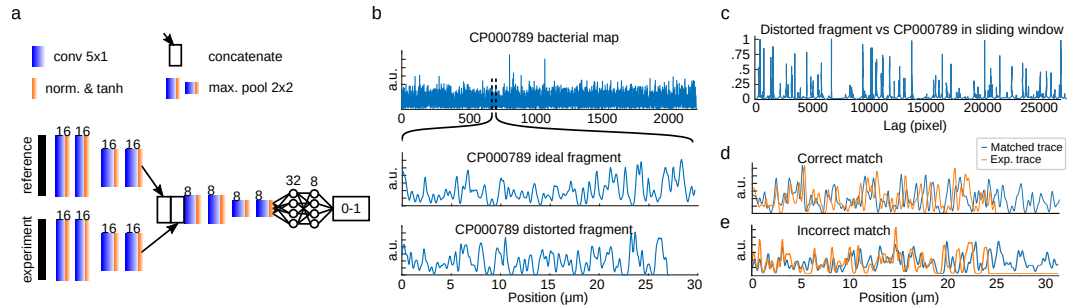

Figure 5.4 – Mapping of bacterial DNA. (a) Correlator network architecture. (b) Ideal CP000789 bacterial map, an ideal fragment and its distorted version. (c) Results of the correlator applied in a sliding windows. (d) Overlay of the distorted map (orange) with the correct corresponding bacteria map (blue). (e) Overlay of the distorted map (orange) with incorrect location on the bacterial map (blue) predicted by the network based on the position of the highest score.

The network training database was obtained by simulating a total of 40000 random map with labelling site density similar to the bacteria Vibrio campbellii chromosome I (CP000789) and II (CP000790). The map were randomly distorted in a similar way as the viral DNA map to produce pair of traces that should be predicted as similar. Pair of map from different traces were obtained by reshuffling the matching pair and randomly generating more traces. Fig. 5.4b shows the full simulated CP000789 map, a selected fragment of 30 μm and the same fragment after distorting the map in a similar way as the viral DNA map.

The network was trained for 80 epochs with the Adam optimizer (learning rate of 10^{-4}) and mean squared error loss function in batches of 50 (test accuracy of 95%). Fig. 5.4c shows the output of the network when comparing the distorted map against the CP000789 ideal map (for one orientation). We see that the network identify certain region of the bacterial map as very similar to the distorted map. While one of these peaks corresponds to the correct location, other regions of the genome are also predicted to be highly similar by the network. The non-linear nature of the network makes it prone to a low specificity as relatively small correlations between two signals might be over-amplified and produce an over-estimated similarity score. As an example we show in Fig. 5.4d and 5.4e a correct and a wrong prediction of the network. While being from two different region of the genome, the two sequences show some similarities which are amplified by the network.

In its current form, the network could be used a fast way to identify candidate regions of the genomes where normalized cross-correlation and p-value analysis could be used to provide the specificity. A solution to increase the specificity of the network would be to change its

output prediction to not only compute a similarity score but also to predict the mapping hyper-parameter such as labelling density or double labelling rate, imposing stronger constrain on the network during the training.

6 Conclusion and Outlook

In summary, my thesis aimed at developing new microscopy methods. I built a framework for the 3D image formation of partially coherent bright field microscope. I introduced a new method for quantitative phase retrieval and associated it with super-resolution microscopy using a unique multi-plane prism. To improve the live cell compatibility of the multi-plane setup, I combined the prism detection with a structured illumination and achieved volumetric high-speed high-resolution imaging of mitochondria network in live COS7 cells. Triggered by the limited illumination power, I designed, built and programmed a high-speed high-power multi-color 2D or 3D SIM illumination using a galvanometer system, a mirror mounter on a piezo and a retro-reflector inside a Michelson interferometer to generate a sinusoidal pattern. Motivated by the lack of tools for resolution estimation, I proposed a new method for resolution estimation, based on the computation of many cross-correlations of filtered version of the input image with itself. Finally, I showed how we can use deep learning to assist the specific field of optical DNA mapping.

This chapter is highly subjective and reflects my point of view on the results presented in this thesis and further work that might be carried on.

6.1   3D quantitative phase microscopy

In chapter 2, a framework for the 3D quantitative phase retrieval from a stack of bright field image was presented. This work is greatly inspired from the derivation presented in Born and Wolf[6] to derive an expression for the scattered field as a function of the scattering potential and incident field. We then expanded the derivation to include the partial spatial and temporal coherence of the illumination. Making use of the Wiener-Khintchine theorem [71], which is in essence the approximation that a scattering event is only coherent with itself, we arrived to an expression for the 3D partially coherent image formation. By understanding the 3D shape of the transfer function and rewriting the expression in term of the average intensity and the complex cross-spectral density, it became clear that the complex cross-spectral density could be retrieved via a simple filtering in Fourier space, which turned out to be a simple axial Hilbert filter. Furthermore we showed how the quantitative phase could be expressed as a

function of the real and imaginary part of the cross-spectral density and demonstrated the quantitativeness of the method.

A detailed analysis of the overlap between the cross-spectral density and its complex conjugate revealed that the phase information contained in this band could be recovered through a deconvolution operation. This allowed us to link our theory with an established state-of-the-art method for phase retrieval from defocused bright field measurement, called the Transport of Intensity Equation. Unlike the TIE, our derivation is not restricted to 2D phase object and paraxial field. While we showed slightly improved results for the recovery of high frequencies, the main scientific contribution of this section remains, in my opinion, in the improved theoretical understanding of the partially coherent image formation. Compared to other approaches for phase imaging, our method has the advantage of simplicity as it only requires a bright field illumination and no modifications of the detection path.

Combined with the multi-plane prism, designed by Dr. Marcel Leuteneger, Dr. Stephan Geissbuehler and Prof. Theo Lasser, we demonstrated for the first time 3D quantitative phase imaging at 200Hz. Since the phase imaging does not require any additional optical component in the detection path, it can be readily combined with fluorescence and super-resolution microscopy, providing the sensitivity and structural information of phase microscopy with the specificity and sub-diffraction imaging of super-resolution microscopy.

While we mainly focused on a technical demonstration of how the multi-plane setup performs, I believe that there is a lot more that can be done. One highly interesting application would be to combine the 3D phase microscopy with machine learning to perform what is called digital labelling[162–164]. While looking extremely promising, all theses results have to be taken with a grain of salt as no one understand (and might never) what the network is learning and how it interprets the data. It is clear that many cell structure scatters light and that the signal, although imperceptible, is present in the input image. However, we clearly see that all the results published so far are unable to accurately predict high-resolution structures and are only accurate in predicting the shapes. While image segmentation is the task of choice for a neural network, we have to ask the question if we can really trust a black box which has been trained and therefore unavoidably biassed with already known data. This issue appears in the work of Ouyang et. all.[165], where they trained a network to predict super-resolution images from a sparse localization subset. In their case, the network acts as an interpolation function. If trained on microtubule data, it will try to interpolate fibres. If trained on nuclear pore complex data, it will try to interpolate circles, independently of the origin of the input data, missing in the process the opportunity to learn something.

6.2 SIM microscopy

While SOFI is able to achieve 3D super-resolution with a relatively low acquisition time, it remains limited to low cumulant order in practice. Relatively high illumination power densities are also required to image the fluctuations of single molecules with sufficient SNR.

To circumvent these limitations, we combined the multi-plane imaging setup with structured illumination microscopy. We decided to implement the SIM illumination using a digital micromirror device (DMD) due to its high-speed potential, its flexibility and its simplicity. We were aiming to realize for the first time high-speed 3D SIM in live cells however the extremely high-loss of the DMD due to spurious diffraction orders and the 8 fold splitting of the fluorescence signal by the prism severely limited the achievable signal to noise ratio and prevented us from reaching the theoretical limit of SIM. We therefore restricted ourselves to a higher contrast coarser pattern and recorded volumetric 2D SIM images of live mitochondria in COS-7 cells. This work was also the occasion to write my own SIM reconstruction method in Matlab.

The original challenging goal remains to achieve true 3D SIM on live cell using a multi-plane prism however a different illumination design is required to minimize the losses in the illumination path while keeping the high speed and flexibility of the DMD design. The solution I designed is presented in chapter 3.2. The setup I built, aligned and programmed is able to project sinusoidal patterns at 1 kHz and is ultimately limited by the fluorescence rate. We demonstrated multi-color 2D SIM and, for the first time, the experimental combination of SOFI and SIM on a fixed sample.

Further work would focus on demonstrating live cell multi-color imaging, improving the setup signal to noise ratio of the SOFI-SIM experiment by implementing a polarization control scheme or doing TIRF-SOFI-SIM. Another aspect would be to combine this SIM design with a multi-plane prism and achieve super-resolution high speed 3D SIM imaging.

6.3 Image resolution estimation

When we are talking about super-resolution microscopy, the question of the achieved resolution is obviously of great interest. However when I started my PhD, there was no universal method for this task. A solution presented already in 1980 proposed the use of Fourier Ring Correlation (FRC) of two images supposed strictly identical except for their noise content. As stated in the name, it consists in computing the correlation between the two images in rings of increasing radii in Fourier space. As the spatial frequency increases, the signal to noise of the two images decreases which is translated in a decrease of the correlation. The so-called FRC curve need then to be thresholded to estimate a cut-off frequency. The first problem of this method is the need for a threshold which directly affects the resolution estimate. The second is that the assumption that the two images are identical is most of the time partially fulfilled. The violation of this assumption strongly biases the final estimate and there exists no solution to correct for this.

Another method to estimate the image resolution is based on drawing line profiles and cherry-picking the smallest resolvable structure. This approach is obviously highly subjective but highlights the important fact that the information we are looking for is present in the image. In this thesis, I developed a new method to extract this information from a single image using partial phase correlations between the input image and many filtered version of the same

input image. The strength of the algorithm is that it requires no additional parameters and predicts an objective resolution estimate.

Further development concerns the expansion of the algorithm in the third dimension. While being trivial in principle, a careful study is required to understand the behaviour of the method when the sampling is limited and when the signal is sparse. The speed of the method could also be greatly improved by designing a parallel version of the algorithm and optimizing the convergence of the method in order to minimize the number of cross-correlations to be computed.

Finally, it would be very interesting to implement the algorithm as a module in a autonomous microscope, guaranteeing optimal imaging conditions of the sample. It could also be used as a criterion to stop the acquisition of localization microscopy data based on the evolution and saturation of the resolution estimate.

6.4   Deep DNA mapping

During my thesis, I also had the opportunity to study the field of deep learning and learn how to use dedicated open source tools such as jupyter notebook, tensorflow and keras. I decided to use neural networks to work on the problem of optical DNA mapping, an excellent example of applying a microscopy technique as a quantitative tool. Using neural networks, I was able to significantly simplify the problem of automatic segmentation by training the network to recognize DNA molecules. I also trained a collection of networks to classify the extracted signal to estimate the population of viral species. Finally I proposed a network architecture to map a fragment against a much larger bacterial DNA map. The results were promising but suffered from relatively low specificity, probably due to the highly non-linear response of the network to small correlations. A possible solutions to increase the specificity would be to train the network to not only predict a similarity score but also predict hyper-parameters such as the stretching factor or the labelling efficiency.

A PRISM multi-plane platform for 3D phase and SOFI imaging

The telecentric multi-plane platform (MP) allows the simultaneous acquisition of 8 fluorescence or bright field images originating from 8 object planes with a constant inter-plane distance (Fig. A.2). The fluorescence excitation is realized by wide-field epi-illumination, whereas phase imaging uses the Koehler bright field arm from a commercial Zeiss microscope. The detection system is common to both imaging modalities, i.e., the setup is a classical microscope with an integrated telescope containing an image splitting prism in the detection path (optical design (Section A.2) and specification LOB-EPFL, Lausanne; manufacturing Schott SA, Yverdon, Switzerland). An adjustable field stop in the intermediate image plane prevents the overlap of the images on the cameras. All lenses and optomechanics are standard commercial components, except for the custom-made holder for the prism and cameras (see Fig. A.1 and Table A.1 for the list of optical components). This versatile MP microscope allows diffraction limited imaging for all 8 conjugated object-image planes.
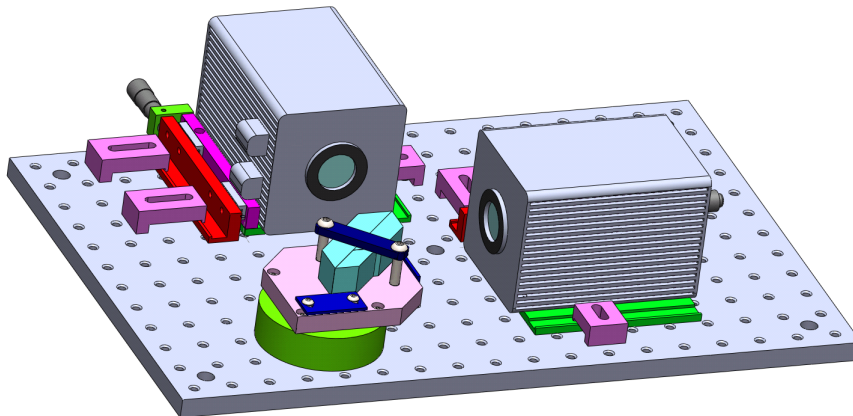

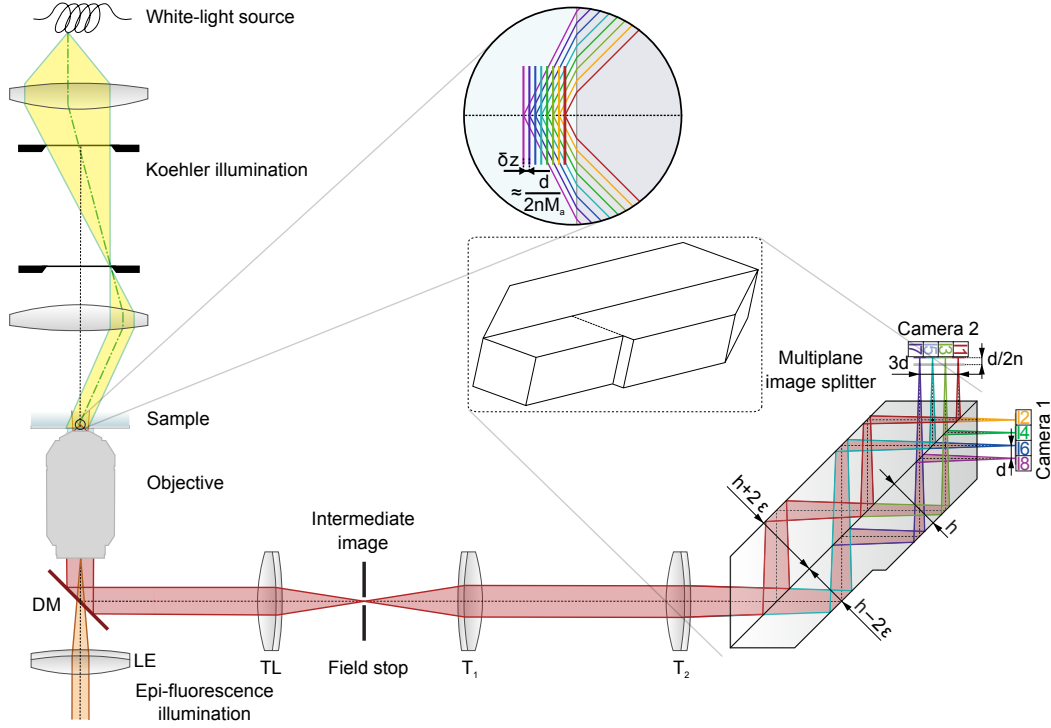Figure A.1 – Custom-made holder for the prism and cameras.

Figure A.2 – Microscope setup. Wide-field epi-illumination for fluorescence imaging combined with a Koehler trans-illumination for phase imaging. The multi-plane image splitting prism directs the light coming from 8 axially distinct planes in the sample towards 4 adjacent fields of view on each of the two cameras. The lenses in the detection path are arranged as a sequence of four 2f configurations. DM dichroic mirror, LE lens, TL tube lens, T1 and T2 lenses.

A.1 Image splitter prism design

As shown in Fig. A.2 and A.3, the image splitter consists of 3 individual prisms glued along the common interfaces. The different images have individual paths and accumulate path length differences such that a conjugated object-image condition is ensured. The light paths undergo multiple total reflection at the outer prism interfaces, whereas the common inner interface has a customized 50:50 coating for equal image intensities.

Essential for a constant inter-plane distance and a constant lateral displacement d are the different prism heights h and $h \pm 2\varepsilon$ ($\varepsilon = \frac{d}{\sqrt{2}}$). As indicated in Fig. A.2, the images are channelled in an interlaced fashion, i.e. the odd images (1, 3, 5, 7) are acquired by camera 1, the even images (2, 4, 6, 8) are acquired by camera 2. The neighbouring images on both cameras are laterally displaced by a distance d, which corresponds to a path length difference of $\Delta z = \frac{d}{n}$ (prism refractive index n = 1.458), i.e. for example the path length difference of image 7 to image 5 equals Δz. The first camera is additionally shifted by $\Delta z_{IP} = \frac{d}{2n}$, which results in a constant inter-plane (IP) distance of the consecutive axial planes Δz_{IP}. We chose the displacement of neighboring images $d = 3.32mm$ such that the row of four images matches

Component	Specifications
White light Koehler illumination	Axiovert 100 M, 12 V 100 W Halogen lamp (Carl Zeiss)
Fluorescence widefield epi-illumination	120 mW, 405 nm laser (iBeam smart, Toptica)
	800 mW, 635 nm laser (MLL-III-635, Roithner)
	800 mW, 532 nm laser (MLL-FN-532, Roithner)
Objective	UPLSAPO 60XW 1.2 NA (Olympus)
Microscope stage	piezoLEGS® stage (3-PT-60-F2,5/5)
	Motion-Commander-Piezo (Nanos Instruments)
Filters	Dichroic zt405/488/532/640rpc, (Chroma)
Tube lens	$f_{TL} = 140mm$
	(achr. doublet (AC 140/22.4, ANR 574070), Qioptiq)
Telescope lenses	$f_{T_1} = 160mm$ and $f_{T_2} = 200mm$
	(achr. doublets (AC 160/22.4, ANR 576447)
	(AC 200/22.4, ANR 556031), Qioptiq)
Prism	Corning C-7980, n= 1.458 (at 587.56 nm),
	Abbe number V = 67.8
Camera	Orca Flash 4.0 (Hamamatsu), pixel pitch = $6.5\mu m$

Table A.1 – Components of the MP detection. All optomechanics are standard commercial components, except for the custom-made holder for the prisms and cameras.

the width of the sCMOS sensor (Orca Flash 4.0, Hamamatsu). The geometric path lengths of the rays in the prism range from 96.52 mm for the images 7 and 8 to 106.48 mm for the images 1 and 2. We performed an analysis of image aberrations using Zemax. Results are summarized in Section A.2 below.

The inter-plane distance of consecutive axial planes in object space is then given by $\delta z_{IP} = \frac{\Delta z_{IP}}{M_a}$ where $M_a = M_l^2$ is the axial magnification. Experimentally, the inter-plane distance was estimated as $347 \pm 11nm$ (mean ± standard deviation of 8 individual measurements of surface immobilized fluorescent beads scanned along the optical axis in 200 nm steps).

A.2 Analysis of the MP design performance

The overall system has been fully designed based on ray tracing with Zemax (Radiant Zemax LLC). The layout of the optical design of the detection path is shown in Fig. A.2. As we are lacking the objective's design data, we modelled the objective as a paraxial lens with 3 mm focal length and 7.2 mm aperture diameter. The field stop is adjusted to suppress crosstalk between the different images, resulting in an image side numerical aperture of $NA_i = 0.031$. All lenses (TL, T1, T2) are in this paraxial path and are standard lenses (Qioptiq) as indicated in Table A.1. All optical distances are chosen at the effective focal length per element (see Fig. A.4). The objective is placed in a telecentric configuration and the tube lens TL to the image plane is almost image-side telecentric (exit pupil position > 33 m from the image plane).

Our analysis of the optical aberrations based on the Seidel diagram (Fig. A.5) shows that the spherical aberration due to the prism is insignificant. Moreover, the axial colour (chromatic
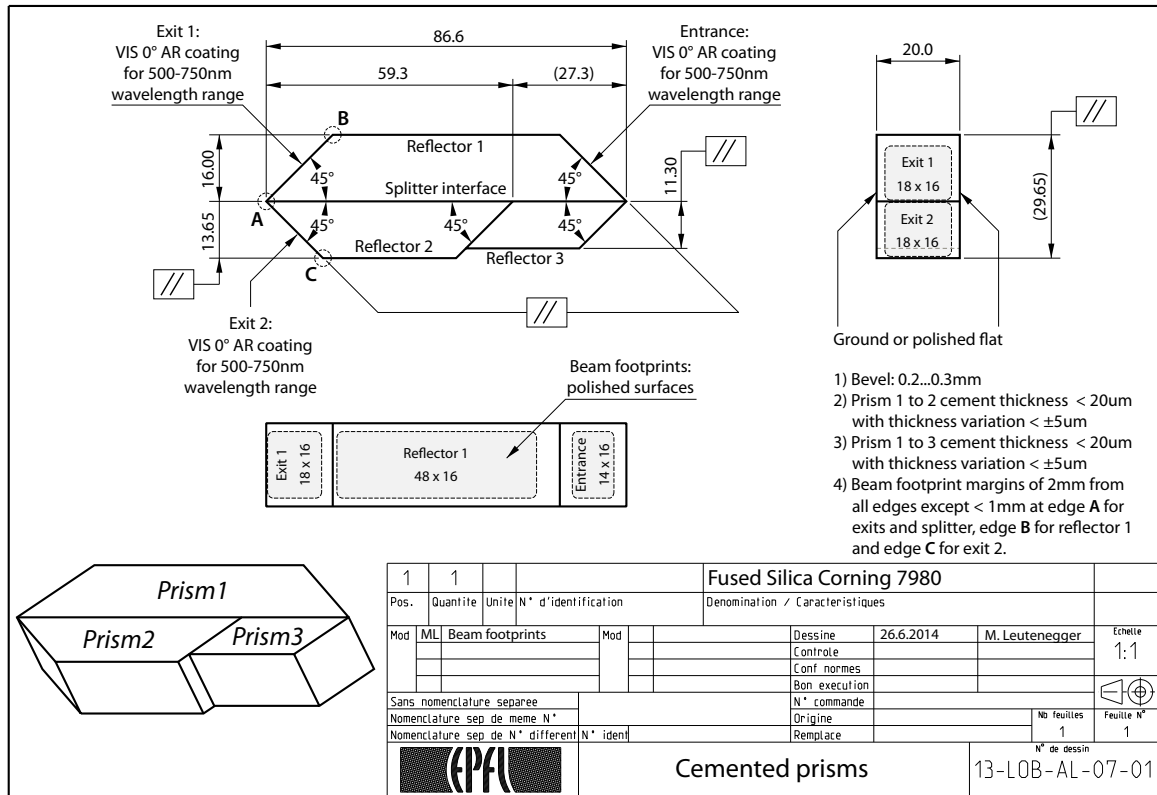
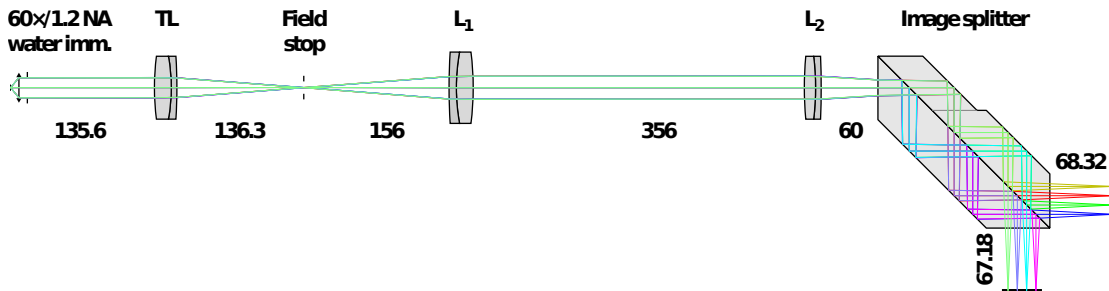Figure A.3 – Technical drawing of the image splitter prism assembly.

Figure A.4 – Layout of the detection system containing a 60×/1.20 NA water immersion objective, the tube lens ($f_{TL} = 140\,mm$), the field stop, the telescope lenses T1 ($f_1 = 160\,mm$) and T2 ($f_2 = 200\,mm$) and the image splitter with two cameras. The free-space distances are indicated in millimetres and are 3x downscaled in the Figure.

length aberration, CLA) of the prism compensates the axial colour of all lenses. Therefore, the remaining system aberrations are due to the "unknown" aberrations of the objective and the residual aberrations of the lenses. The Seidel diagram shows that the axial colour is the dominant aberration with CLA $< \lambda/2$ the wavelength range 500–650 nm. These residual aberrations are even lower for the used wavelength range. The optical path length differences (OPD) are below $\lambda/2$ for the wavelength range and field sizes up to 100 μm in diameter (Fig. A.6).
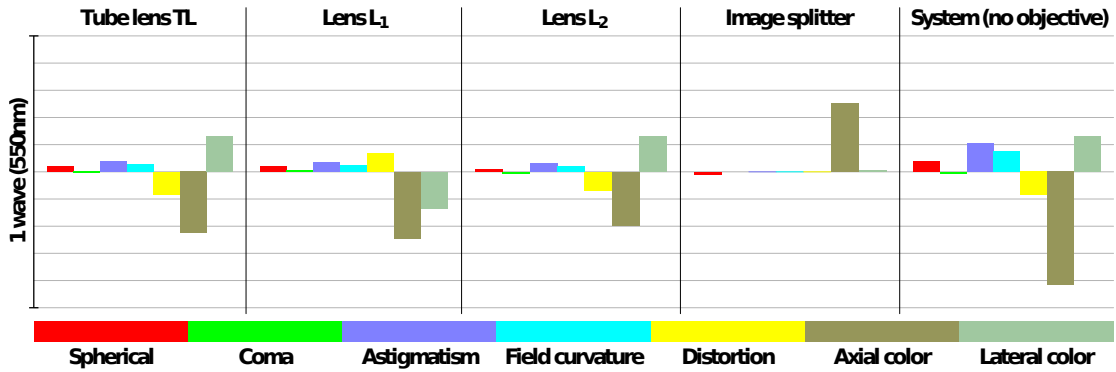
Figure A.5 – Seidel diagram (third-order aberrations) of the detection path. The major aberrations of the system are axial colour with about 0.4 waves, and lateral colour and astigmatism with about 0.1 waves each.
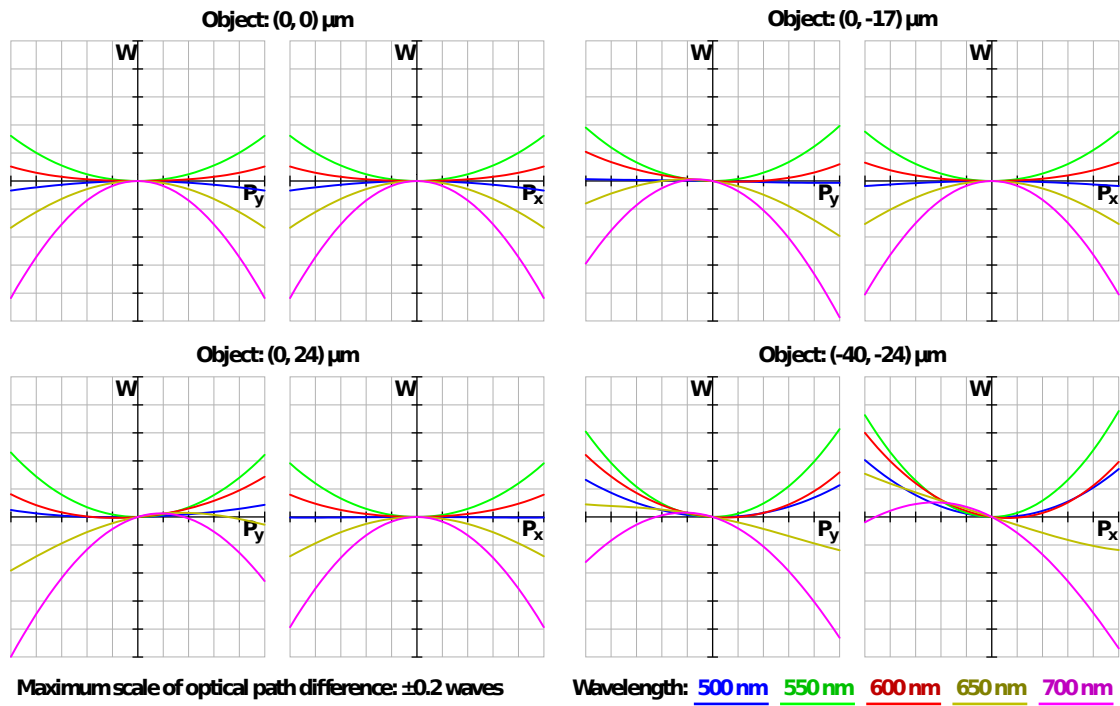
Figure A.6 – Optical path length difference (OPD) versus normalized pupil position. The OPD shows diffraction-limited performance ($|W| < 0.2$ waves) over an extended wavelength range and field.

For all fields and wavelengths, the geometrical PSF is below the Airy radius indicating clearly a diffraction-limited performance (Fig. A.7). As shown in the spot diagrams, the chief ray positions shift slightly due to lateral chromatic aberration well below the Airy radius, indicating that these residual lateral chromatic aberrations are insignificant. The diffraction-limited performance of the detection system is also evidenced by the polychromatic modulation transfer and point spread functions (Fig. A.8), showing a Strehl ratio > 0.95.

In summary we have a diffraction limited performance of our MP system.
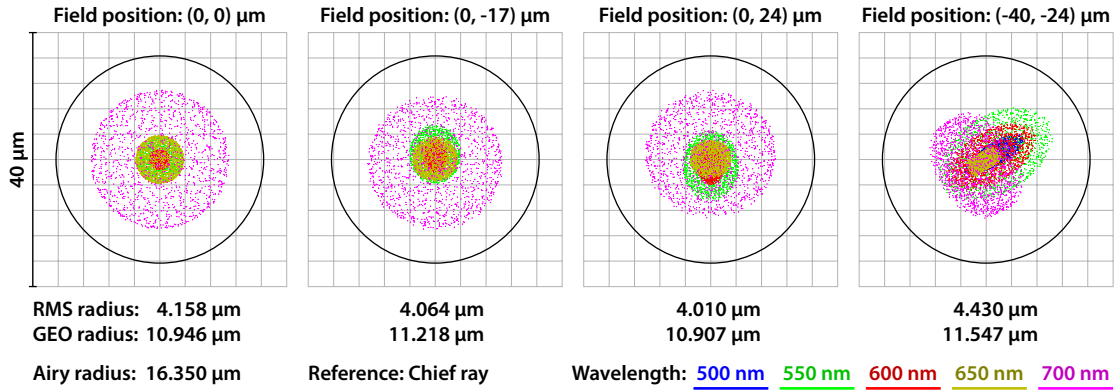
Figure A.7 – Spot diagrams of the ray intersections in all image planes. The root-mean-square (RMS) radii of the spots are much smaller than the Airy radius, which confirms the diffraction-limited performance across all image fields.
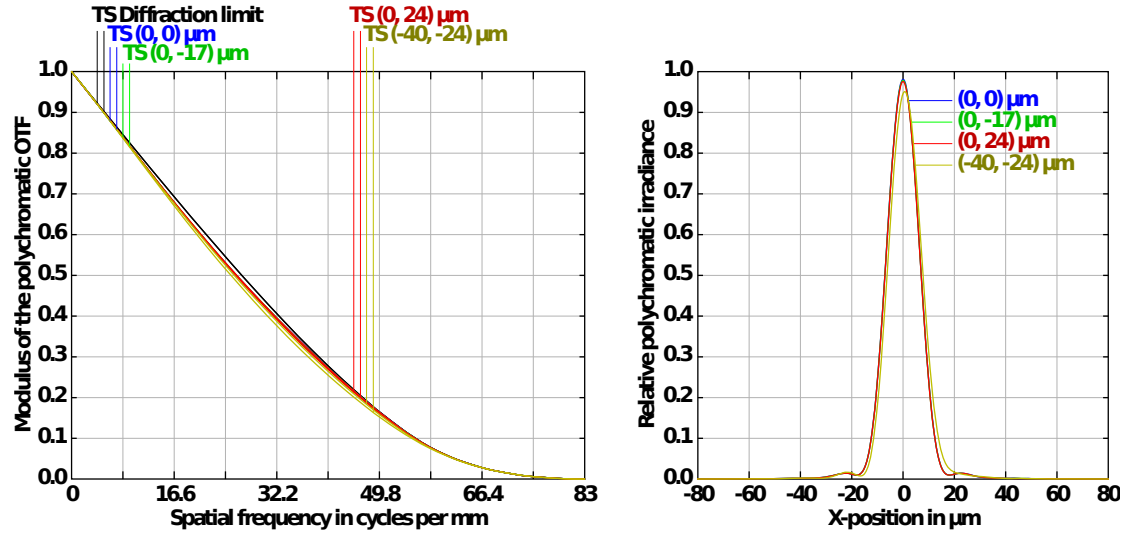
Figure A.8 – Polychromatic modulation transfer function (MTF) and point spread function (PSF). The MTF closely approaches the diffraction limit for all field positions and the PSF peak value and the Strehl ratio – are well above 0.8.

A.3 MP prism calibration

3D multi-plane imaging demands accurate calibration of the image planes. Co-alignment for both imaging modalities is based on an affine transformation and bilinear image interpolation (see Fig. A.9). The transformation parameters are extracted from a calibration measurement of fluorescent beads scanned along the optical axis in 200 nm steps over the whole sampling volume.

The beads calibration measurements are also used to correct the transmission variation among the 8 image channels (slight deviation from 50:50 channel splitting) for SOFI processing. For phase imaging, the channels transmission correction is based on bright field images.

Figure A.9 – Co-registration of image planes. An affine transformation and bilinear interpolation based on a calibration measurement with fluorescent beads is applied to (pairs of) image channels at different steps in the analysis routine.

B ImageJ plugin

In order to simplify the access to our method, we translated the algorithm in Java and developed an ImageJ plugin[77] (publicly available on https://github.com/Ades91/ImDecorr.git; tested for ImageJ 1.48 to 1.52 and Micromanager 1.4). Fig. B.1 shows the current plugin graphical user interface (GUI of Version 1.1.5).
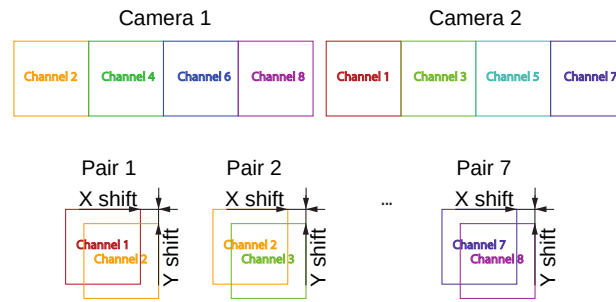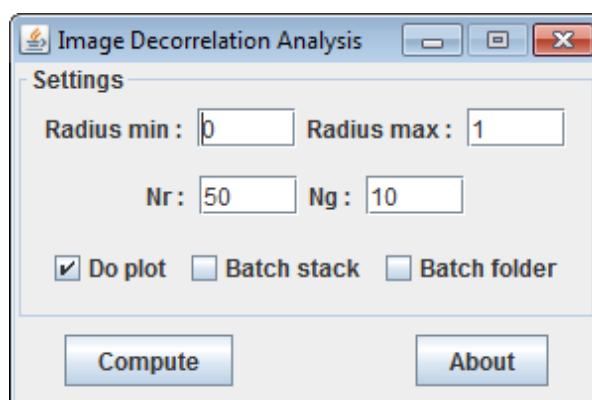

Figure B.1 – ImageJ plugin V1.1.5 with default settings

The operation mode of the plugin is straightforward. Open the image of interest in ImageJ and make sure it is the active window. Before running the analysis, it is important to set the image pixel size and units (Image -> Properties... -> Unit of length, Pixel width and pixel height). If empty or not defined, the plugin will return the resolution in pixel units. Click on compute and once the analysis is done, results are added to the main results table.

The plugin supports multidimensional stacks of any bit depth. If a RGB image is supplied, it will be automatically converted to grayscale. The plugin also supports rectangular ROI, which allows to repeat the analysis on sub-regions and check the consistency of the estimate over the whole image.

The settings panel is composed of 4 optional parameters of the computation, specifying the range of normalized frequencies where the correlations have to be computed (from Radius min to Radius max), as well as the number of points in between (N_r, typically 50 points).

Finally, N_g (typically 10) specify the number of intermediate high-pass filtering used to find the resolution. These parameters essentially determine the speed of the computation. Since all the points of the decorrelation function are independent of each other, the computation time is proportional to the total number of points which is equal to $N_r * (2 * N_g + 1)$. The proposed default value of $N_r = 50$ and $N_g = 10$ were experimentally determined as good compromise for fast but accurate results.

We also provide additional processing options in the form of 3 check-boxes:

Do plot:

If checked, plot all the computed decorrelation functions and local maxima (example of plot shown in Fig. B.2).

Batch stack:

If checked, process all the frames, slices and channel of the current image. If do plot is also checked, all the decorrelation functions for all the images will be plotted.

Batch folder:

If checked, the user will be asked to select a folder containing images. All images are then opened, processed and the result table is automatically saved in the selected folder as a .csv file. Again, if "do plot" is checked, all the decorrelation analysis will be plotted.
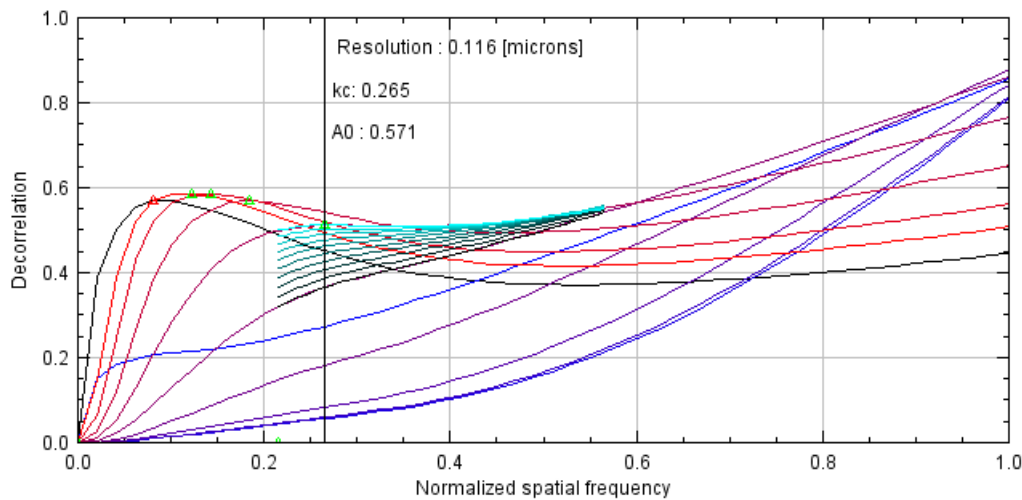
Figure B.2 – ImageJ plot of the analysis showing the non-filtered decorrelation function(black), its local maximum (red triangle), all the high-pass versions (color gradient from red (weak filtering) to blue (strong filtering)), all the local maxima (green triangle) and the estimated resolution, cutoff frequency kc and SNR A0. The second set of lines (here from ~ 0.15 to 0.52) corresponds to the refinement operation where the computation is repeated on a smaller range of N_r and N_g for increased robustness.

C Resolution estimation compatible SIM reconstruction

Due to the sensibility of the method to manipulations of the Fourier space, publicly available SIM reconstructions algorithms are not compatible with resolution estimation without resulting in biased resolution due to Fourier filtering and deconvolution.

Consequently, we wrote our own SIM reconstruction algorithm (in Matlab) and discuss required features for decorrelation compatible SIM reconstruction.

Pre-processing

We first compute and subtract the mean of all images. We then apodize the edges of the all the raw image with a cosine function and add the previously computed mean. High frequency artefacts arising for edges discontinuities are consequently minimized.

Peak finding

After specification of the frequency band where the peak should be found, the absolute value of the Fourier transform of all the raw images are multiplied with a circular symmetric inverted OTF, defined as

$$OTF_{inv}(k) = \left(\frac{|k|}{k_c}\right)(|k| < k_c) \tag{C.1}$$

where $k = \sqrt{k_x^2 + k_y^2}$ is the radial frequency and k_c is a user defined cutoff frequency. This operation attempts to flatten the Fourier space by balancing the effect of the OTF on the peaks intensity. Consequently, the 5 largest Fourier pixel within the frequency band are localized and clustered. This allows to reliably exclude randomly bright Fourier pixels. The position and phase of the peak are then stored.

Unmixing

Using the peaks phase values, an adequate transformation matrix is build and the corresponding Fourier components are unmixed pixels per pixels for each angle.

Reconstruction

For each angle, all the zero order components are averaged to reconstruct the pseudo wide field image. This image is then zero-padded in Fourier space and all the other components are translated according to their peak position and added together. The resulting Fourier spectrum is then reweighted to balance the partial overlap of the Fourier components (otherwise, the Fourier space of the SIM image will be plagued with weak edges that might produce significant peaks in the decorrelation analysis, preventing any resolution estimate).

Finally, instead of masking the Fourier space with an apodization filter, that might bias the resolution estimate, we crop the Fourier space. This partially removes the high-frequency noise but without creating any artificial edges. This also have the side effect of changing the projected pixel size of the resulting SIM image.

Bibliography

[1] E. Hecht, "Optics 4th edition. optics," *Addison Wesley Longman Inc*, vol. 1, p. 1998, 1998.

[2] "Adgut : Alzheimer's disease - gut connection," 2016-2020. EPFL (Coordinator); Ulm University; Leuven University; Flemish institute for Biotechnology; Lund University and Bern University.

[3] A. Köhler, "Ein neues beleuchtungsverfahren für mikrophotographische zwecke," *Zeitschrift für wissenschaftliche Mikroskopie und für Mikroskopische Technik*, vol. 10, no. 4, pp. 433–440, 1893.

[4] J. W. Goodman, *Introduction to Fourier optics.* Roberts and Company Publishers, 2005.

[5] W. Singer, M. Totzeck, and H. Gross, *Handbook of optical systems, volume 2: Physical image formation.* John Wiley & Sons, 2006.

[6] M. Born and E. Wolf, "Principles of optics, 7th (expanded) edition," *United Kingdom: Press Syndicate of the University of Cambridge*, vol. 461, 1999.

[7] F. Zernike, "Phase contrast, a new method for the microscopic observation of transparent objects," *Physica*, vol. 9, no. 7, pp. 686–698, 1942.

[8] R. Allen and G. David, "The zeiss-nomarski differential interference equipment for transmitted-light microscopy," *Zeitschrift für wissenschaftliche Mikroskopie und mikroskopische Technik*, vol. 69, no. 4, pp. 193–221, 1969.

[9] D. Gabor, "A new microscopic principle," 1948.

[10] E. Cuche, F. Bevilacqua, and C. Depeursinge, "Digital holography for quantitative phase-contrast imaging," *Optics letters*, vol. 24, no. 5, pp. 291–293, 1999.

[11] E. Cuche, P. Marquet, and C. Depeursinge, "Spatial filtering for zero-order and twin-image elimination in digital off-axis holography," *Applied optics*, vol. 39, no. 23, pp. 4070–4075, 2000.

[12] M. R. Teague, "Deterministic phase retrieval: a green's function solution," *JOSA*, vol. 73, no. 11, pp. 1434–1441, 1983.

[13] A. H. Coons, "The demonstration of pneumococcal antigen in tissues by the use of fluorescent antibody," *J Immunol*, vol. 45, p. 159, 1942.

Bibliography

[14] M. Chalfie, Y. Tu, G. Euskirchen, W. W. Ward, and D. C. Prasher, "Green fluorescent protein as a marker for gene expression," *Science*, vol. 263, no. 5148, pp. 802–805, 1994.

[15] J. R. Lakowicz, *Principles of fluorescence spectroscopy.* Springer Science & Business Media, 2013.

[16] G. G. Stokes, "On the change of refrangibility of light," *Philosophical transactions of the Royal Society of London*, no. 142, pp. 463–562, 1852.

[17] S. Doose, H. Neuweiler, and M. Sauer, "Fluorescence quenching by photoinduced electron transfer: a reporter for conformational dynamics of macromolecules," *ChemPhysChem*, vol. 10, no. 9-10, pp. 1389–1398, 2009.

[18] S. van de Linde, I. Krstić, T. Prisner, S. Doose, M. Heilemann, and M. Sauer, "Photoinduced formation of reversible dye radicals and their impact on super-resolution imaging," *Photochemical & Photobiological Sciences*, vol. 10, no. 4, pp. 499–506, 2011.

[19] F. Zernike, "Beugungstheorie des schneidenver-fahrens und seiner verbesserten form, der phasenkontrastmethode," *physica*, vol. 1, pp. 689–704, 1934.

[20] "A java software package to generate realistic 3d microscope point-spread function (psf)." http://bigwww.epfl.ch/algorithms/psfgenerator/. Accessed: 2020-01-29.

[21] P. Ewald, "Zur theorie der interferenzen der röntgenstrahlen in kristallen," *Phys. Z*, vol. 14, pp. 465–472, 1913.

[22] E. Ash and G. Nicholls, "Super-resolution aperture scanning microscope," *Nature*, vol. 237, no. 5357, pp. 510–512, 1972.

[23] S. W. Hell and J. Wichmann, "Breaking the diffraction resolution limit by stimulated emission: stimulated-emission-depletion fluorescence microscopy," *Optics letters*, vol. 19, no. 11, pp. 780–782, 1994.

[24] S. W. Hell, K. I. Willig, M. Dyba, S. Jakobs, L. Kastrup, and V. Westphal, "Nanoscale resolution with focused light: Sted and other resolft microscopy concepts," *Handbook of biological confocal microscopy*, pp. 571–579, 2006.

[25] R. Schmidt, C. A. Wurm, S. Jakobs, J. Engelhardt, A. Egner, and S. W. Hell, "Spherical nanosized focal spot unravels the interior of cells," *Nature methods*, vol. 5, no. 6, pp. 539–544, 2008.

[26] D. Wildanger, B. R. Patton, H. Schill, L. Marseglia, J. Hadden, S. Knauer, A. Schönle, J. G. Rarity, J. L. O'Brien, S. W. Hell, *et al.*, "Solid immersion facilitates fluorescence microscopy with nanometer resolution and sub-ångström emitter localization," *Advanced Materials*, vol. 24, no. 44, pp. OP309–OP313, 2012.

[27] C. Osseforth, J. R. Moffitt, L. Schermelleh, and J. Michaelis, "Simultaneous dual-color 3d sted microscopy," *Optics express*, vol. 22, no. 6, pp. 7028–7039, 2014.

[28] D. Wildanger, R. Medda, L. Kastrup, and S. W. Hell, "A compact sted microscope providing 3d nanoscale resolution," *Journal of microscopy*, vol. 236, no. 1, pp. 35–43, 2009.

[29] R. Heintzmann and C. G. Cremer, "Laterally modulated excitation microscopy: improvement of resolution by using a diffraction grating," in *Optical Biopsies and Microscopic Techniques III*, vol. 3568, pp. 185–196, International Society for Optics and Photonics, 1999.

[30] J. T. Frohn, *Super-resolution fluorescence microscopy by structured ligth illumination.* PhD thesis, ETH Zurich, 2000.

[31] M. G. Gustafsson, "Surpassing the lateral resolution limit by a factor of two using structured illumination microscopy," *Journal of microscopy*, vol. 198, no. 2, pp. 82–87, 2000.

[32] K. Wicker and R. Heintzmann, "Resolving a misconception about structured illumination," *Nature Photonics*, vol. 8, no. 5, pp. 342–344, 2014.

[33] C. J. Sheppard, "Super-resolution in confocal imaging," *Optik (Stuttgart)*, vol. 80, no. 2, pp. 53–54, 1988.

[34] C. B. Müller and J. Enderlein, "Image scanning microscopy," *Physical review letters*, vol. 104, no. 19, p. 198101, 2010.

[35] A. G. York, P. Chandris, D. Dalle Nogare, J. Head, P. Wawrzusin, R. S. Fischer, A. Chitnis, and H. Shroff, "Instant super-resolution imaging in live cells and embryos via analog image processing," *Nature methods*, vol. 10, no. 11, p. 1122, 2013.

[36] M. G. Gustafsson, "Nonlinear structured-illumination microscopy: wide-field fluorescence imaging with theoretically unlimited resolution," *Proceedings of the National Academy of Sciences of the United States of America*, vol. 102, no. 37, pp. 13081–13086, 2005.

[37] P. Kner, B. B. Chhun, E. R. Griffis, L. Winoto, and M. G. Gustafsson, "Super-resolution video microscopy of live cells by structured illumination," *Nature methods*, vol. 6, no. 5, pp. 339–342, 2009.

[38] P. Křížek, I. Raška, and G. M. Hagen, "Flexible structured illumination microscope with a programmable illumination array," *Optics express*, vol. 20, no. 22, pp. 24585–24599, 2012.

[39] K. Wicker, O. Mandula, G. Best, R. Fiolka, and R. Heintzmann, "Phase optimisation for structured illumination microscopy," *Optics express*, vol. 21, no. 2, pp. 2032–2049, 2013.

[40] Q. Yang, L. Cao, H. Zhang, H. Zhang, and G. Jin, "Method of lateral image reconstruction in structured illumination microscopy with super resolution," *Journal of Innovative Optical Health Sciences*, p. 1630002, 2015.

[41] S. A. Shroff, J. R. Fienup, and D. R. Williams, "Phase-shift estimation in sinusoidally illuminated images for lateral superresolution," *JOSA A*, vol. 26, no. 2, pp. 413–424, 2009.

[42] J. Demmerle, C. Innocent, A. J. North, G. Ball, M. Müller, E. Miron, A. Matsuda, I. M. Dobbie, Y. Markaki, and L. Schermelleh, "Strategic and practical guidelines for successful structured illumination microscopy," *Nature protocols*, vol. 12, no. 5, p. 988, 2017.

[43] M. G. Gustafsson, L. Shao, P. M. Carlton, C. R. Wang, I. N. Golubovskaya, W. Z. Cande, D. A. Agard, and J. W. Sedat, "Three-dimensional resolution doubling in wide-field fluorescence microscopy by structured illumination," *Biophysical journal*, vol. 94, no. 12, pp. 4957–4970, 2008.

[44] Z. Liu, L. D. Lavis, and E. Betzig, "Imaging live-cell dynamics and structure at the single-molecule level," *Molecular cell*, vol. 58, no. 4, pp. 644–659, 2015.

[45] M. J. Rust, M. Bates, and X. Zhuang, "Sub-diffraction-limit imaging by stochastic optical reconstruction microscopy (storm)," *Nature methods*, vol. 3, no. 10, pp. 793–796, 2006.

[46] S. Wolter, M. Schüttpelz, M. Tscherepanow, S. Van de Linde, M. Heilemann, and M. Sauer, "Real-time computation of subdiffraction-resolution fluorescence images," *Journal of microscopy*, vol. 237, no. 1, pp. 12–22, 2010.

[47] M. Heilemann, S. van de Linde, A. Mukherjee, and M. Sauer, "Super-resolution imaging with small organic fluorophores," *Angewandte Chemie International Edition*, vol. 48, no. 37, pp. 6903–6908, 2009.

[48] E. Betzig, G. H. Patterson, R. Sougrat, O. W. Lindwasser, S. Olenych, J. S. Bonifacino, M. W. Davidson, J. Lippincott-Schwartz, and H. F. Hess, "Imaging intracellular fluorescent proteins at nanometer resolution," *Science*, vol. 313, no. 5793, pp. 1642–1645, 2006.

[49] S. T. Hess, T. P. Girirajan, and M. D. Mason, "Ultra-high resolution imaging by fluorescence photoactivation localization microscopy," *Biophysical journal*, vol. 91, no. 11, pp. 4258–4272, 2006.

[50] A. Sharonov and R. M. Hochstrasser, "Wide-field subdiffraction imaging by accumulated binding of diffusing probes," *Proceedings of the National Academy of Sciences*, vol. 103, no. 50, pp. 18911–18916, 2006.

[51] J. Schnitzbauer, M. T. Strauss, T. Schlichthaerle, F. Schueder, and R. Jungmann, "Super-resolution microscopy with dna-paint," *Nature protocols*, vol. 12, no. 6, p. 1198, 2017.

[52] B. Huang, W. Wang, M. Bates, and X. Zhuang, "Three-dimensional super-resolution imaging by stochastic optical reconstruction microscopy," *Science*, vol. 319, no. 5864, pp. 810–813, 2008.

[53] I. Izeddin, M. El Beheiry, J. Andilla, D. Ciepielewski, X. Darzacq, and M. Dahan, "Psf shaping using adaptive optics for three-dimensional single-molecule super-resolution imaging and tracking," *Optics express*, vol. 20, no. 5, pp. 4957–4967, 2012.

[54] M. Speidel, A. Jonáš, and E.-L. Florin, "Three-dimensional tracking of fluorescent nanoparticles with subnanometer precision by use of off-focus imaging," *Optics letters*, vol. 28, no. 2, pp. 69–71, 2003.

[55] S. Ram, P. Prabhat, J. Chao, E. S. Ward, and R. J. Ober, "High accuracy 3d quantum dot tracking with multifocal plane microscopy for the study of fast intracellular dynamics in live cells," *Biophysical journal*, vol. 95, no. 12, pp. 6025–6043, 2008.

[56] S. R. P. Pavani, M. A. Thompson, J. S. Biteen, S. J. Lord, N. Liu, R. J. Twieg, R. Piestun, and W. Moerner, "Three-dimensional, single-molecule fluorescence imaging beyond the diffraction limit by using a double-helix point spread function," *Proceedings of the National Academy of Sciences*, vol. 106, no. 9, pp. 2995–2999, 2009.

[57] S. Jia, J. C. Vaughan, and X. Zhuang, "Isotropic three-dimensional super-resolution imaging with a self-bending point spread function," *Nature photonics*, vol. 8, no. 4, p. 302, 2014.

[58] P. Bon, J. Linares-Loyez, M. Feyeux, K. Alessandri, B. Lounis, P. Nassoy, and L. Cognet, "Self-interference 3d super-resolution microscopy for deep tissue investigations," *Nature methods*, vol. 15, no. 6, pp. 449–454, 2018.

[59] P. Jouchet, C. Cabriel, N. Bourg, M. Bardou, C. Pous, F. Emmanuel, and S. Lévêque-Fort, "Nanometric axial localization of single fluorescent molecules with modulated excitation," *BioRxiv*, p. 865865, 2019.

[60] F. Balzarotti, Y. Eilers, K. C. Gwosch, A. H. Gynnå, V. Westphal, F. D. Stefani, J. Elf, and S. W. Hell, "Nanometer resolution imaging and tracking of fluorescent molecules with minimal photon fluxes," *Science*, vol. 355, no. 6325, pp. 606–612, 2017.

[61] Y. Eilers, H. Ta, K. C. Gwosch, F. Balzarotti, and S. W. Hell, "Minflux monitors rapid molecular jumps with superior spatiotemporal resolution," *Proceedings of the National Academy of Sciences*, vol. 115, no. 24, pp. 6117–6122, 2018.

[62] K. I. Mortensen, L. S. Churchman, J. A. Spudich, and H. Flyvbjerg, "Optimized localization analysis for single-molecule tracking and super-resolution microscopy," *Nature methods*, vol. 7, no. 5, p. 377, 2010.

[63] F. Huang, T. M. Hartwich, F. E. Rivera-Molina, Y. Lin, W. C. Duim, J. J. Long, P. D. Uchil, J. R. Myers, M. A. Baird, W. Mothes, *et al.*, "Video-rate nanoscopy using scmos camera–specific single-molecule localization algorithms," *Nature methods*, vol. 10, no. 7, pp. 653–658, 2013.

[64] D. Baddeley, M. B. Cannell, and C. Soeller, "Visualization of localization microscopy data," *Microscopy and microanalysis*, vol. 16, no. 1, pp. 64–72, 2010.

[65] T. Dertinger, R. Colyer, G. Iyer, S. Weiss, and J. Enderlein, "Fast, background-free, 3d super-resolution optical fluctuation imaging (sofi)," *Proceedings of the National Academy of Sciences*, vol. 106, no. 52, pp. 22287–22292, 2009.

[66] T. Dertinger, R. Colyer, R. Vogel, J. Enderlein, and S. Weiss, "Achieving increased resolution and more pixels with superresolution optical fluctuation imaging (sofi)," *Optics express*, vol. 18, no. 18, pp. 18875–18885, 2010.

[67] T. Dertinger, J. Xu, O. F. Naini, R. Vogel, and S. Weiss, "Sofi-based 3d superresolution sectioning with a widefield microscope," *Optical nanoscopy*, vol. 1, no. 1, pp. 1–5, 2012.

[68] S. Geissbuehler, N. L. Bocchio, C. Dellagiacoma, C. Berclaz, M. Leutenegger, and T. Lasser, "Mapping molecular statistics with balanced super-resolution optical fluctuation imaging (bsofi)," *Optical Nanoscopy*, vol. 1, no. 1, p. 4, 2012.

[69] S. Geissbuehler, A. Sharipov, A. Godinat, N. L. Bocchio, P. A. Sandoz, A. Huss, N. A. Jensen, S. Jakobs, J. Enderlein, F. G. Van Der Goot, *et al.*, "Live-cell multiplane three-dimensional super-resolution optical fluctuation imaging," *Nature communications*, vol. 5, p. 5830, 2014.

[70] W. Singer and K.-H. Brenner, "Transition of the scalar field at a refracting surface in the generalized kirchhoff diffraction theory," *JOSA A*, vol. 12, no. 9, pp. 1913–1919, 1995.

[71] L. Mandel and E. Wolf, *Optical coherence and quantum optics.* Cambridge university press, 1995.

[72] N. Streibl, "Three-dimensional imaging by a microscope," *JOSA A*, vol. 2, no. 2, pp. 121–127, 1985.

[73] C. McCutchen, "Generalized aperture and the three-dimensional diffraction image," *JOSA*, vol. 54, no. 2, pp. 240–244, 1964.

[74] E. C. Titchmarsh, *Introduction to the theory of Fourier integrals.* Clarendon Press, 1948.

[75] T. H. Nguyen, C. Edwards, L. L. Goddard, and G. Popescu, "Quantitative phase imaging with partially coherent illumination," *Optics letters*, vol. 39, no. 19, pp. 5511–5514, 2014.

[76] T. Kim, C. Edwards, L. L. Goddard, and G. Popescu, "Quantitative phase imaging with programmable illumination," in *Quantitative Phase Imaging*, vol. 9336, p. 93361F, International Society for Optics and Photonics, 2015.

[77] M. D. Abràmoff, P. J. Magalhães, and S. J. Ram, "Image processing with imagej," *Biophotonics international*, vol. 11, no. 7, pp. 36–42, 2004.

[78] N. Streibl, "Phase imaging by the transport equation of intensity," *Optics communications*, vol. 49, no. 1, pp. 6–10, 1984.

[79] A. Descloux, K. Grußmayer, E. Bostan, T. Lukes, A. Bouwens, A. Sharipov, S. Geissbuehler, A.-L. Mahul-Mellier, H. Lashuel, M. Leutenegger, *et al.*, "Combined multi-plane phase retrieval and super-resolution optical fluctuation imaging for 4d cell microscopy," *Nature Photonics*, vol. 12, no. 3, pp. 165–172, 2018.

[80] S. Geissbuehler, C. Dellagiacoma, and T. Lasser, "Comparison between sofi and storm," *Biomedical optics express*, vol. 2, no. 3, pp. 408–420, 2011.

[81] H. Deschout, T. Lukes, A. Sharipov, D. Szlag, L. Feletti, W. Vandenberg, P. Dedecker, J. Hofkens, M. Leutenegger, T. Lasser, *et al.*, "Complementarity of palm and sofi for super-resolution live-cell imaging of focal adhesions," *Nature communications*, vol. 7, no. 1, pp. 1–11, 2016.

[82] B. Borm, R. P. Requardt, V. Herzog, and G. Kirfel, "Membrane ruffles in cell migration: indicators of inefficient lamellipodia adhesion and compartments of actin filament reorganization," *Experimental cell research*, vol. 302, no. 1, pp. 83–95, 2005.

[83] H. A. Lashuel, C. R. Overk, A. Oueslati, and E. Masliah, "The many faces of α-synuclein: from structure and toxicity to therapeutic target," *Nature Reviews Neuroscience*, vol. 14, no. 1, pp. 38–48, 2013.

[84] J. Riedl, A. H. Crevenna, K. Kessenbrock, J. H. Yu, D. Neukirchen, M. Bista, F. Bradke, D. Jenne, T. A. Holak, Z. Werb, *et al.*, "Lifeact: a versatile marker to visualize f-actin," *Nature methods*, vol. 5, no. 7, pp. 605–607, 2008.

[85] M. G. Gustafsson, "Surpassing the lateral resolution limit by a factor of two using structured illumination microscopy," *Journal of microscopy*, vol. 198, no. 2, pp. 82–87, 2000.

[86] R. Heintzmann and T. Huser, "Super-resolution structured illumination microscopy," *Chemical Reviews*, vol. 177, no. 23, pp. 13890–13908, 2017.

[87] K. O'Holleran and M. Shaw, "Optimized approaches for optical sectioning and resolution enhancement in 2d structured illumination microscopy," *Biomedical optics express*, vol. 5, no. 8, pp. 2580–2590, 2014.

[88] M. Shaw, L. Zajiczek, and K. O'Holleran, "High speed structured illumination microscopy in optically thick samples," *Methods*, vol. 88, pp. 11–19, 2015.

[89] F. Ströhl and C. F. Kaminski, "Speed limits of structured illumination microscopy," *Optics letters*, vol. 42, no. 13, pp. 2511–2514, 2017.

[90] H.-W. Lu-Walther, M. Kielhorn, R. Förster, A. Jost, K. Wicker, and R. Heintzmann, "fast-sim: a practical implementation of fast structured illumination microscopy," *Methods and Applications in Fluorescence*, vol. 3, no. 1, p. 014001, 2015.

[91] L. Song, H.-W. Lu-Walther, R. Förster, A. Jost, M. Kielhorn, J. Zhou, and R. Heintzmann, "Fast structured illumination microscopy using rolling shutter cameras," *Measurement Science and Technology*, vol. 27, no. 5, p. 055401, 2016.

[92] S. Abrahamsson, S. Usawa, and M. Gustafsson, "A new approach to extended focus for high-speed high-resolution biological microscopy," in *Three-Dimensional and Multi-dimensional Microscopy: Image Acquisition and Processing XIII*, vol. 6090, p. 60900N, International Society for Optics and Photonics, 2006.

[93] S. Abrahamsson, J. Chen, B. Hajj, S. Stallinga, A. Y. Katsov, J. Wisniewski, G. Mizuguchi, P. Soule, F. Mueller, C. D. Darzacq, X. Darzacq, C. Wu, C. I. Bargmann, D. A. Agard,

M. Dahan, and M. G. L. Gustafsson, "Fast multicolor 3d imaging using aberration-corrected multifocus microscopy," *Nature methods*, vol. 10, no. 1, p. 60, 2013.

[94] S. Abrahamsson, R. Ilic, J. Wisniewski, B. Mehl, L. Yu, L. Chen, M. Davanco, L. Oudjedi, J.-B. Fiche, B. Hajj, X. Jin, C. Pulupa, Joan Cho, M. Mir, M. E. Beheiry, X. Darzacq, M. Nollmann, M. Dahan, C. Wu, T. Lionnet, J. A. Liddle, and C. I. Bargmann, "Multifocus microscopy with precise color multi-phase diffractive optics applied in functional neuronal imaging," *Biomedical optics express*, vol. 7, no. 3, pp. 855–869, 2016.

[95] S. Abrahamsson, H. Blom, A. Agostinho, D. C. Jans, A. Jost, M. Müller, L. Nilsson, K. Bernhem, T. J. Lambert, R. Heintzmann, and H. Brismar, "Multifocus structured illumination microscopy for fast volumetric super-resolution imaging," *Biomedical optics express*, vol. 8, no. 9, pp. 4135–4140, 2017.

[96] M. F. Juette, T. J. Gould, M. D. Lessard, M. J. Mlodzianoski, B. S. Nagpure, B. T. Bennett, S. T. Hess, and J. Bewersdorf, "Three-dimensional sub–100 nm resolution fluorescence microscopy of thick samples," *Nature methods*, vol. 5, no. 6, p. 527, 2008.

[97] K. O'Holleran and M. Shaw, "Polarization effects on contrast in structured illumination microscopy," *Optics letters*, vol. 37, no. 22, pp. 4603–4605, 2012.

[98] M. Sison, S. Chakrabortty, J. Extermann, A. Nahas, P. J. Marchand, A. Lopez, T. Weil, and T. Lasser, "3d time-lapse imaging and quantification of mitochondrial dynamics," *Scientific Reports*, vol. 7, p. 43275, 2017.

[99] L. Große, C. A. Wurm, C. Brüser, D. Neumann, D. C. Jans, and S. Jakobs, "Bax assembles into large ring-like structures remodeling the mitochondrial outer membrane in apoptosis," *The EMBO journal*, vol. 35, no. 4, pp. 402–413, 2016.

[100] A. Descloux, K. S. Grußmayer, and A. Radenovic, "Parameter-free image resolution estimation based on decorrelation analysis," *Nature methods*, vol. 16, no. 9, pp. 918–924, 2019.

[101] M. Müller, V. Mönkemöller, S. Hennig, W. Hübner, and T. Huser, "Open-source image reconstruction of super-resolution structured illumination microscopy data in imagej," *Nature Communications*, vol. 7, 2016.

[102] X. Huang, J. Fan, L. Li, H. Liu, R. Wu, Y. Wu, L. Wei, H. Mao, A. Lal, P. Xi, L. Tang, Y. Zhang, Y. Liu, S. Tan, and L. Chen, "Fast, long-term, super-resolution imaging with hessian structured illumination microscopy," *Nature Biotechnology*, 4 2018.

[103] W. Liu, Q. Liu, Z. Zhang, Y. Han, C. Kuang, L. Xu, H. Yang, and X. Liu, "Three-dimensional super-resolution imaging of live whole cells using galvanometer-based structured illumination microscopy," *Optics express*, vol. 27, no. 5, pp. 7237–7248, 2019.

[104] A. Classen, J. von Zanthier, and G. S. Agarwal, "Enhancing superresolution optical fluctuation imaging (sofi) by use of structured illumination," *arXiv*, 2018.

[105] G. Zhao, C. Zheng, C. Kuang, and X. Liu, "Resolution-enhanced sofi via structured illumination," *Optics letters*, vol. 42, no. 19, pp. 3956–3959, 2017.

[106] K. Chu, P. J. McMillan, Z. J. Smith, J. Yin, J. Atkins, P. Goodwin, S. Wachsmann-Hogiu, and S. Lane, "Image reconstruction for structured-illumination microscopy with low signal level," *Optics express*, vol. 22, no. 7, pp. 8687–8702, 2014.

[107] S. J. Sahl, S. W. Hell, and S. Jakobs, "Fluorescence nanoscopy in cell biology," *Nature reviews Molecular cell biology*, vol. 18, no. 11, p. 685, 2017.

[108] Y. M. Sigal, R. Zhou, and X. Zhuang, "Visualizing and discovering cellular structures with super-resolution microscopy," *Science*, vol. 361, no. 6405, pp. 880–887, 2018.

[109] E. Abbe, "Beiträge zur theorie des mikroskops und der mikroskopischen wahrnehmung," *Archiv für mikroskopische Anatomie*, vol. 9, no. 1, pp. 413–418, 1873.

[110] C. J. Sheppard, "Resolution and super-resolution," *Microscopy research and technique*, vol. 80, no. 6, pp. 590–598, 2017.

[111] R. M. Power and J. Huisken, "Adaptable, illumination patterning light sheet microscopy," *Scientific reports*, vol. 8, no. 1, pp. 1–11, 2018.

[112] M. Štefko, B. Ottino, K. M. Douglass, and S. Manley, "Autonomous illumination control for localization microscopy," *Optics express*, vol. 26, no. 23, pp. 30882–30900, 2018.

[113] M. Van Heel, "Similarity measures between images," *Ultramicroscopy*, vol. 21, no. 1, pp. 95–100, 1987.

[114] W. Saxton and W. Baumeister, "The correlation averaging of a regularly arranged bacterial cell envelope protein," *Journal of microscopy*, vol. 127, no. 2, pp. 127–138, 1982.

[115] G. Harauz and M. van Heel, "Exact filters for general geometry three dimensional reconstruction," *Optik (Stuttgart)*, vol. 73, no. 4, pp. 146–156, 1986.

[116] P. B. Rosenthal and R. Henderson, "Optimal determination of particle orientation, absolute hand, and contrast loss in single-particle electron cryomicroscopy," *Journal of molecular biology*, vol. 333, no. 4, pp. 721–745, 2003.

[117] E. V. Orlova, P. Dube, J. R. Harris, E. Beckman, F. Zemlin, J. Markl, and M. van Heel, "Structure of keyhole limpet hemocyanin type 1 (klh1) at 15 å resolution by electron cryomicroscopy and angular reconstitution," *Journal of molecular biology*, vol. 271, no. 3, pp. 417–437, 1997.

[118] M. Unser, B. L. Trus, and A. C. Steven, "A new resolution criterion based on spectral signal-to-noise ratios," *Ultramicroscopy*, vol. 23, no. 1, pp. 39–51, 1987.

[119] N. Banterle, K. H. Bui, E. A. Lemke, and M. Beck, "Fourier ring correlation as a resolution criterion for super-resolution microscopy," *Journal of structural biology*, vol. 183, no. 3, pp. 363–367, 2013.

Bibliography

[120] R. P. Nieuwenhuizen, K. A. Lidke, M. Bates, D. L. Puig, D. Grünwald, S. Stallinga, and B. Rieger, "Measuring image resolution in optical nanoscopy," *Nature methods*, vol. 10, no. 6, p. 557, 2013.

[121] G. Tortarolo, M. Castello, A. Diaspro, S. Koho, and G. Vicidomini, "Evaluating image resolution in stimulated emission depletion microscopy," *Optica*, vol. 5, no. 1, pp. 32–35, 2018.

[122] J. J. Schmied, A. Gietl, P. Holzmeister, C. Forthmann, C. Steinhauer, T. Dammeyer, and P. Tinnefeld, "Fluorescence and super-resolution standards based on dna origami," *Nature methods*, vol. 9, no. 12, pp. 1133–1134, 2012.

[123] M. Raab, I. Jusuk, J. Molle, E. Buhr, B. Bodermann, D. Bergmann, H. Bosse, and P. Tinnefeld, "Using dna origami nanorulers as traceable distance measurement standards and nanoscopic benchmark structures," *Scientific reports*, vol. 8, no. 1, pp. 1–11, 2018.

[124] A. Szymborska, A. De Marco, N. Daigle, V. C. Cordes, J. A. Briggs, and J. Ellenberg, "Nuclear pore scaffold structure analyzed by super-resolution microscopy and particle averaging," *Science*, vol. 341, no. 6146, pp. 655–658, 2013.

[125] M. Bates, "Single-particle analysis for fluorescence nanoscopy," *Nature methods*, vol. 15, no. 10, pp. 771–772, 2018.

[126] M. Minsky, "Memoir on inventing the confocal scanning microscope," *Scanning*, vol. 10, no. 4, pp. 128–138, 1988.

[127] G. Vicidomini, P. Bianchini, and A. Diaspro, "Sted super-resolved microscopy," *Nature methods*, vol. 15, no. 3, p. 173, 2018.

[128] G. Tortarolo, Y. Sun, K. W. Teng, Y. Ishitsuka, L. Lanzanó, P. R. Selvin, B. Barbieri, A. Diaspro, and G. Vicidomini, "Photon-separation to enhance the spatial resolution of pulsed sted microscopy," *Nanoscale*, vol. 11, no. 4, pp. 1754–1761, 2019.

[129] V. Westphal and S. W. Hell, "Nanoscale resolution in the focal plane of an optical microscope," *Physical review letters*, vol. 94, no. 14, p. 143903, 2005.

[130] S. Galiani, B. Harke, G. Vicidomini, G. Lignani, F. Benfenati, A. Diaspro, and P. Bianchini, "Strategies to maximize the performance of a sted microscope," *Optics express*, vol. 20, no. 7, pp. 7362–7374, 2012.

[131] R. Heintzmann and T. Huser, "Super-resolution structured illumination microscopy," *Chemical reviews*, vol. 117, no. 23, pp. 13890–13908, 2017.

[132] Y. Peeters, W. Vandenberg, S. Duwé, A. Bouwens, T. Lukeš, C. Ruckebusch, T. Lasser, and P. Dedecker, "Correcting for photodestruction in super-resolution optical fluctuation imaging," *Scientific reports*, vol. 7, no. 1, p. 10470, 2017.

[133] M. Sauer and M. Heilemann, "Single-molecule localization microscopy in eukaryotes," *Chemical reviews*, vol. 117, no. 11, pp. 7478–7509, 2017.

[134] R. J. Marsh, K. Pfisterer, P. Bennett, L. M. Hirvonen, M. Gautel, G. E. Jones, and S. Cox, "Artifact-free high-density localization microscopy analysis," *Nature methods*, vol. 15, no. 9, pp. 689–692, 2018.

[135] W. R. Legant, L. Shao, J. B. Grimm, T. A. Brown, D. E. Milkie, B. B. Avants, L. D. Lavis, and E. Betzig, "High-density three-dimensional localization microscopy across large volumes," *Nature methods*, vol. 13, no. 4, pp. 359–365, 2016.

[136] J. Fölling, V. Belov, R. Kunetsky, R. Medda, A. Schönle, A. Egner, C. Eggeling, M. Bossi, and S. Hell, "Photochromic rhodamines provide nanoscopy with optical sectioning," *Angewandte Chemie International Edition*, vol. 46, no. 33, pp. 6266–6270, 2007.

[137] M. Bossi, J. Fölling, V. N. Belov, V. P. Boyarskiy, R. Medda, A. Egner, C. Eggeling, A. Schönle, and S. W. Hell, "Multicolor far-field fluorescence nanoscopy through isolated detection of distinct molecular species," *Nano letters*, vol. 8, no. 8, pp. 2463–2468, 2008.

[138] T. J. Lambert and J. C. Waters, "Navigating challenges in the application of superresolution microscopy," *Journal of Cell Biology*, vol. 216, no. 1, pp. 53–63, 2017.

[139] M. Mikhaylova, B. M. Cloin, K. Finan, R. Van Den Berg, J. Teeuw, M. M. Kijanka, M. Sokolowski, E. A. Katrukha, M. Maidorn, F. Opazo, *et al.*, "Resolving bundled microtubules using anti-tubulin nanobodies," *Nature communications*, vol. 6, no. 1, pp. 1–7, 2015.

[140] T. Pleiner, M. Bates, and D. Görlich, "A toolbox of anti–mouse and anti–rabbit igg secondary nanobodies," *Journal of Cell Biology*, vol. 217, no. 3, pp. 1143–1154, 2018.

[141] M. Ovesnỳ, P. Křížek, J. Borkovec, Z. Švindrych, and G. M. Hagen, "Thunderstorm: a comprehensive imagej plug-in for palm and storm data analysis and super-resolution imaging," *Bioinformatics*, vol. 30, no. 16, pp. 2389–2390, 2014.

[142] P. Annibale, S. Vanni, M. Scarselli, U. Rothlisberger, and A. Radenovic, "Quantitative photo activated localization microscopy: unraveling the effects of photoblinking," *PloS one*, vol. 6, no. 7, 2011.

[143] J. Deen, "High resolution dna mapping for species identification," *KU Leuven PhD thesis*, 2016.

[144] C. Vranken, J. Deen, L. Dirix, T. Stakenborg, W. Dehaen, V. Leen, J. Hofkens, and R. K. Neely, "Super-resolution optical dna mapping via dna methyltransferase-directed click chemistry," *Nucleic acids research*, vol. 42, no. 7, pp. e50–e50, 2014.

[145] L. K. Nyberg, F. Persson, J. Berg, J. Bergström, E. Fransson, L. Olsson, M. Persson, A. Stålnacke, J. Wigenius, J. O. Tegenfeldt, *et al.*, "A single-step competitive binding assay for mapping of single dna molecules," *Biochemical and biophysical research communications*, vol. 417, no. 1, pp. 404–408, 2012.

[146] V. Müller and F. Westerlund, "Optical dna mapping in nanofluidic devices: principles and applications," *Lab on a Chip*, vol. 17, no. 4, pp. 579–590, 2017.

Bibliography

[147] A. N. Nilsson, G. Emilsson, L. K. Nyberg, C. Noble, L. S. Stadler, J. Fritzsche, E. R. Moore, J. O. Tegenfeldt, T. Ambjörnsson, and F. Westerlund, "Competitive binding-based optical dna mapping for fast identification of bacteria-multi-ligand transfer matrix theory and experimental applications on escherichia coli," *Nucleic acids research*, vol. 42, no. 15, pp. e118–e118, 2014.

[148] A. Bouwens, J. Deen, R. Vitale, L. D'Huys, V. Goyvaerts, A. Descloux, D. Borrenberghs, K. Grussmayer, T. Lukes, R. Camacho, *et al.*, "Identifying microbial species by single-molecule dna optical mapping and resampling statistics," *NAR Genomics and Bioinformatics*, vol. 2, no. 1, p. lqz007, 2020.

[149] D. Bogas, L. Nyberg, R. Pacheco, N. F. Azevedo, J. P. Beech, M. Gomila, J. Lalucat, C. M. Manaia, O. C. Nunes, J. O. Tegenfeldt, *et al.*, "Applications of optical dna mapping in microbiology," *BioTechniques*, vol. 62, no. 6, pp. 255–267, 2017.

[150] J. S. Biteen, P. C. Blainey, Z. G. Cardon, M. Chun, G. M. Church, P. C. Dorrestein, S. E. Fraser, J. A. Gilbert, J. K. Jansson, R. Knight, *et al.*, "Tools for the microbiome: nano and beyond," 2016.

[151] N. M. Vogt, R. L. Kerby, K. A. Dill-McFarland, S. J. Harding, A. P. Merluzzi, S. C. Johnson, C. M. Carlsson, S. Asthana, H. Zetterberg, K. Blennow, *et al.*, "Gut microbiome alterations in alzheimer's disease," *Scientific reports*, vol. 7, no. 1, pp. 1–11, 2017.

[152] T. Harach, N. Marungruang, N. Duthilleul, V. Cheatham, K. Mc Coy, G. Frisoni, J. Neher, F. Fåk, M. Jucker, T. Lasser, *et al.*, "Reduction of abeta amyloid pathology in appps1 transgenic mice in the absence of gut microbiota," *Scientific reports*, vol. 7, p. 41802, 2017.

[153] A. L. Samuel, "Some studies in machine learning using the game of checkers," *IBM Journal of research and development*, vol. 3, no. 3, pp. 210–229, 1959.

[154] W. S. McCulloch and W. Pitts, "A logical calculus of the ideas immanent in nervous activity," *The bulletin of mathematical biophysics*, vol. 5, no. 4, pp. 115–133, 1943.

[155] F. Rosenblatt, "The perceptron: a probabilistic model for information storage and organization in the brain.," *Psychological review*, vol. 65, no. 6, p. 386, 1958.

[156] Y. LeCun, Y. Bengio, and G. Hinton, "Deep learning," *nature*, vol. 521, no. 7553, pp. 436–444, 2015.

[157] I. Goodfellow, J. Pouget-Abadie, M. Mirza, B. Xu, D. Warde-Farley, S. Ozair, A. Courville, and Y. Bengio, "Generative adversarial nets," in *Advances in neural information processing systems*, pp. 2672–2680, 2014.

[158] S. Hochreiter and J. Schmidhuber, "Long short-term memory," *Neural computation*, vol. 9, no. 8, pp. 1735–1780, 1997.

[159] "Keras api." https://keras.io/. Accessed: 2020-02-19.

[160] P. E. Hart, "How the hough transform was invented [dsp history]," *IEEE Signal Processing Magazine*, vol. 26, no. 6, pp. 18–22, 2009.

[161] O. Ronneberger, P. Fischer, and T. Brox, "U-net: Convolutional networks for biomedical image segmentation," in *International Conference on Medical image computing and computer-assisted intervention*, pp. 234–241, Springer, 2015.

[162] Y. Rivenson, T. Liu, Z. Wei, Y. Zhang, K. de Haan, and A. Ozcan, "Phasestain: the digital staining of label-free quantitative phase microscopy images using deep learning," *Light: Science & Applications*, vol. 8, no. 1, pp. 1–11, 2019.

[163] Y. Rivenson, H. Wang, Z. Wei, K. de Haan, Y. Zhang, Y. Wu, H. Günaydın, J. E. Zuckerman, T. Chong, A. E. Sisk, *et al.*, "Virtual histological staining of unlabelled tissue-autofluorescence images via deep learning," *Nature biomedical engineering*, vol. 3, no. 6, p. 466, 2019.

[164] C. Ounkomol, S. Seshamani, M. M. Maleckar, F. Collman, and G. R. Johnson, "Label-free prediction of three-dimensional fluorescence images from transmitted-light microscopy," *Nature methods*, vol. 15, no. 11, pp. 917–920, 2018.

[165] W. Ouyang, A. Aristov, M. Lelek, X. Hao, and C. Zimmer, "Deep learning massively accelerates super-resolution localization microscopy," *Nature biotechnology*, vol. 36, no. 5, pp. 460–468, 2018.

Adrien Descloux
PhD student in Photonics

adrien.descloux91@gmail.com ✉

+41 79 291 07 08 📱

Chemin du Chêne 17, 1115, Vullierens, Switzerland 📍

github.com/Ades91 ⌂

orcid.org/0000-0002-3101-6641 ⓘ

Fascinated by science and music.
Always interested in learning.

EDUCATION

PhD student in Photonics
EPFL

04/2016 – Present   *Lausanne, Switzerland*

Attended courses
- Quantum Optics and Quantum information
- Deep learning for optical imaging

Master degree in Applied Optics
Carl Zeiss & Twente University

09/2013 – 08/2015   *Jena, Germany & Enschede, The Netherlands*

Thesis
- Optical phase conjugation in multimode fibers

Bachelor in Micro-engineering
EPFL

09/2009 – 07/2013   *Lausanne, Switzerland*

WORK EXPERIENCE

Research assistant
Complex Photonics System, Twente University

Achievements/Tasks
- Continuation of the work pursued during my master Thesis, investigating the limits of high-resolution wavefront shaping
- Results were published in Optics Express

Contact : p.w.h.pinkse@utwente.nl

Internship
Carl Zeiss

02/2015 – 08/2015   *Jena, Germany*

World leader company in microscopy, semi-conductors, metrology and biomedical instrumentation.

Achievements/Tasks
- Master thesis in close collaboration with Twente University

Contact : joerg.petschulat@zeiss.com

Internship
Second Sight

07/2014 – 09/2014   *EPFL, Switzerland*

Second Sight develops groundbreaking prosthetic systems to provide functional vision to the visually impaired.

Achievements/Tasks
- Design and optimization of a new calibration procedure for an eye tracker.

SKILLS

Super-resolution microscopy · Coherent microscopy · Single molecule microscopy · Image processing · Photonics · Optical design · CAD · Deep learning · Java, Python, Matlab, C, C++, arduino, git, P5.js, FPGA

SCIENTIFIC CONTRIBUTIONS

- **Descloux, A.**, Lasser, T., & Radenovic, A. (2019). Tomographic Phase Retrieval: a reformulation of TIE to non-paraxial fields. Manuscript in preparation.

- **Descloux, A.**, Müller, ... & Huser, T. (2019). High speed multi-plane superresolution structured illumination microscopy of living cells using an image-splitting prism. Manuscript in review in *Nanophotonics*.

- **Descloux, A.,** Grußmayer, K. S., & Radenovic, A. (2019). Parameter-free image resolution estimation based on decorrelation analysis. *Nature methods*, 1-7.

- **Descloux, A.,** Grussmayer, K. S., Bostan, E., Lukes, T., Bouwens, A., Sharipov, A., ... & Lasser,T. (2018). Combined multi-plane phase retrieval and super-resolution optical fluctuation imaging for 4D cell microscopy. *Nature Photonics*, 12(3), 165.

- **Descloux, A.,** Amitonova, L. V., & Pinkse, P. W. (2016). Aberrations of the point spread function of a multimode fiber due to partial mode excitation. Optics express, 24(16), 18501-18512.

CONFERENCES

- Parameter free resolution estimation based on decorrelation analysis. **Talk**, SSOM 2019, Engelberg, Switzerland

- Parameter free resolution estimation based on decorrelation analysis. **Talk**, SMLMS19, Delft, The Netherlands

- Combined multi-plane super-resolution and phase microscopy using an image splitting prism. **Poster**, ICON18, Bielefeld, Germany

- Combined multi-plane super-resolution and phase microscopy using an image splitting prism. **Poster**, FOM18, Bruges, Belgium

LANGUAGES

French
Native

English
Expert

German
Professional Working Proficiency

INTERESTS

Guitar · Cello · Jazz Manouche · Philosophy · Science popularization · Theoretical Physics · Number theory · Computer science · Hiking

SCIENTIFIC CONTRIBUTIONS (full list)

- **Descloux, A.**, Lasser, T., & Radenovic, A. (2019). Tomographic Phase Retrieval: a reformulation of TIE to non-paraxial fields. Manuscript in preparation.

- **Descloux, A.**, Müller, ... & Huser, T. (2019). High speed multi-plane superresolution structured illumination microscopy of living cells using an image-splitting prism. Manuscript in review in *Nanophotonics*.

- Grussmayer, K. S., Geissbuehler, S., **Descloux, A.**, ... & Lasser, T. (2019). Spectral Cross-Cumulants for Multicolor Super-resolved SOFI Imaging. Manuscript in review in *Nature Communications*

- Bouwens, A., Deen, J., Vitale, R., DHuys, L., Goyvaerts, V., **Descloux, A.**, ... & Janssen, K. (2019). Identifying microbial species by single-molecule DNA optical mapping and resampling statistics. Accepted in *NAR Genomics & Bioinformatics.*

- **Descloux, A.,** Grußmayer, K. S., & Radenovic, A. (2019). Parameter-free image resolution estimation based on decorrelation analysis. *Nature methods*, 1-7.

- **Descloux, A.,** Grussmayer, K. S., Bostan, E., Lukes, T., Bouwens, A., Sharipov, A., ... & Lasser,T. (2018). Combined multi-plane phase retrieval and super-resolution optical fluctuation imaging for 4D cell microscopy. *Nature Photonics,* 12(3), 165.

- Marchand, P. J., Bouwens, A., Szlag, D., Nguyen, D., **Descloux, A.,** Sison, M., ... & Lasser, T. (2017). Visible spectrum extended-focus optical coherence microscopy for label-free sub-cellular tomography. *Biomedical optics express*, 8(7), 3343-3359.

- **Descloux, A.,** Amitonova, L. V., & Pinkse, P. W. (2016). Aberrations of the point spread function of a multimode fiber due to partial mode excitation. Optics express, 24(16), 18501-18512.

- Amitonova, L. V., **Descloux, A.,** Petschulat, J., ... & Pinkse, P. W. (2016). High-resolution wavefront shaping with a photonic crystal fiber for multimode fiber imaging. *Optics letters,* 41(3), 497-500.